



POLITECNICO
MILANO 1863

SCUOLA DI INGEGNERIA INDUSTRIALE
E DELL'INFORMAZIONE

Characterization of exotic crystal structures of titanium thin films through Brillouin spectroscopy

TESI DI LAUREA MAGISTRALE IN
ENGINEERING PHYSICS - INGEGNERIA FISICA

Author: **Silvia Guadagnini**

Student ID: 965759

Advisor: Prof. Marco Beghi

Co-advisors: David Dellasega

Academic Year: 2021-22

Abstract

Titanium is a transition metal widely exploited in the industrial engineering and medical instrumentation fields because of its strength-to-density ratio and corrosion resistance in harsh conditions. While pure titanium (and the majority of its alloys) exhibits a hexagonal-closed-packed (hcp) crystal structure at room temperature under atmospheric pressure, a body-centered cubic crystal phase can be observed upon varying the temperature. The exceptional properties of titanium and its alloys are linked to their crystal structures. For instance, the hcp structure exhibits limited plastic deformability as compared to the bcc one.

A face-centered cubic (fcc) crystal structure has recently been observed in titanium and its alloys. This new exotic titanium phase has strongly stimulated research interest as such a phase is not predicted by the usual pressure-temperature phase diagram of Ti. The marked interest in the study of titanium exotic phases is intertwined with its widespread applications and usage. Indeed, the physical and mechanical properties of titanium crystal structures are key to understand and design possible technological application.

Thin films of exotic titanium structures have been produced at the Micro and Nano Structured Materials Laboratory (NanoLab) of the Politecnico di Milano. Upon analyzing the samples through X-Ray Diffraction, one finds that the lattice parameter of the structure investigated is compatible with that of a face-centered-cubic Ti structure. The aim of this thesis work is to characterize the thermomechanical properties of these thin films of exotic titanium structures, assessing the values of the elastic constants through Surface Brillouin Spectroscopy (SBS). The analysis yields elastic constant estimates which differ from those expected in the case of an hcp crystal structure. This suggests that the newly discovered titanium exotic phase is harder than pure titanium typically found in nature.

Keywords: titanium, crystal structure, fcc phase, Brillouin spectroscopy

Abstract in lingua italiana

Il titanio (Ti) è un metallo di transizione largamente utilizzato nei campi dell'ingegneria industriale e delle strumentazioni mediche, grazie alla sua resistenza alla corrosione quando esposto a condizioni estreme e al suo rapporto di forza-densità. Il titanio puro (e la maggior parte delle sue leghe) si trova a temperatura ambiente e sotto pressione atmosferica in una struttura cristallina esagonale compatta, mentre assume una struttura cristallina cubica a corpo centrato variando la temperature. Le proprietà eccezionali del titanio e delle sue leghe sono legate alle sue strutture cristalline. Per esempio, la struttura esagonale compatta risulta meno soggetta a deformazioni plastiche rispetto alla struttura cubica a corpo centrato.

Una struttura cristallina cubica a facce centrate è stata osservata di recente nel titanio e nelle sue leghe. Questa nuova fase esotica del titanio ha fortemente stimolato interesse di ricerca in quanto tale fase non è predetta dall'usuale diagramma di fase pressione-temperatura del Ti. Il marcato interesse nello studio delle fasi esotiche del titanio è intrecciato alle sue vaste applicazioni. Infatti, le proprietà fisiche e meccaniche delle strutture cristalline del titanio sono fondamentali per capirne possibili applicazioni tecnologiche.

Al Laboratorio di Materiali Micro- e Nanostrutturati del Politecnico di Milano sono stati recentemente prodotti film sottili di strutture esotiche di titanio. Una prima analisi attraverso diffrazione a raggi X suggerisce che il parametro di cella della struttura investigata è compatibile con quello di una struttura cubica a facce centrate del Ti. Lo scopo di questa tesi è quello di caratterizzare le proprietà termomeccaniche di questi film sottili che mostrano strutture esotiche del titanio, valutandone le costanti elastiche grazie all'ausilio della spettroscopia Brillouin di superficie. Le costanti elastiche trovate differiscono da quelle aspettate nel caso di una struttura cristallina esagonale compatta e suggeriscono che questa nuova fase esotica del titanio sia più resistente del titanio che si trova in natura.

Parole chiave: titanio, struttura cristallina, fase fcc, spettroscopia Brillouin

Contents

Abstract	i
Abstract in lingua italiana	iii
Contents	v
Introduction	1
1 Elastic Waves in Solids and Brillouin Spectroscopy Principles	7
1.1 Elastic Waves in Solids	7
1.1.1 Continuum Mechanics and Theory of Elasticity	7
1.1.2 Elastic Waves Propagation	14
1.2 Brillouin Light Scattering (BLS)	19
1.2.1 Introduction	19
1.2.2 Scattering Geometry	20
2 Experimental Set-Up and Samples Preparation	25
2.1 Experimental Set-Up	25
2.1.1 Laser Radiation and Optical Path	26
2.1.2 Fabry-Perot Interferometer	27
2.2 Samples Preparation	40
2.2.1 Pulsed Laser Deposition	40
2.2.2 Energy-Dispersive X-ray Spectroscopy Analysis	41
2.2.3 X-Ray Diffraction Analysis	41
3 Data Analysis	43
3.1 EDXS and XRD Analysis	43
3.1.1 EDXS Analysis	43
3.1.2 XRD Analysis	44
3.2 Brillouin Spectroscopy Analysis	47

3.2.1	Methodology	48
3.2.2	Results and Discussion	53
	Conclusions	81
	Bibliography	85
	List of Figures	89
	List of Tables	97
	List of Main Symbols	99

Introduction

Titanium (Ti) is a transition metal very well known for its corrosion resistance and strength-to-density ratio [1]. Its high mechanical strength, excellent thermal stability, good corrosion resistance in harsh conditions and intrinsic bio compatibility make it suitable for applications in aerospace, industrial engineering and medical instrumentation [1, 2].

While titanium and many other metals (e.g. Ca, Fe, Co, Zr, Sn, Ce, and Hf) can crystallize in various crystal structures, each modification is only stable within particular temperature ranges [1]. Pure titanium (and the majority of its alloys) exhibits at room temperature under atmospheric pressure an hexagonal-closed-packed (hcp) crystal structure (usually referred to as its α -phase). Titanium body-centered cubic crystal phase (β -phase) can be observed upon raising the temperature above 880° , while maintaining a constant pressure. The atomic unit cells of the hcp α -titanium and the bcc β -titanium are schematically shown in Figure 1.

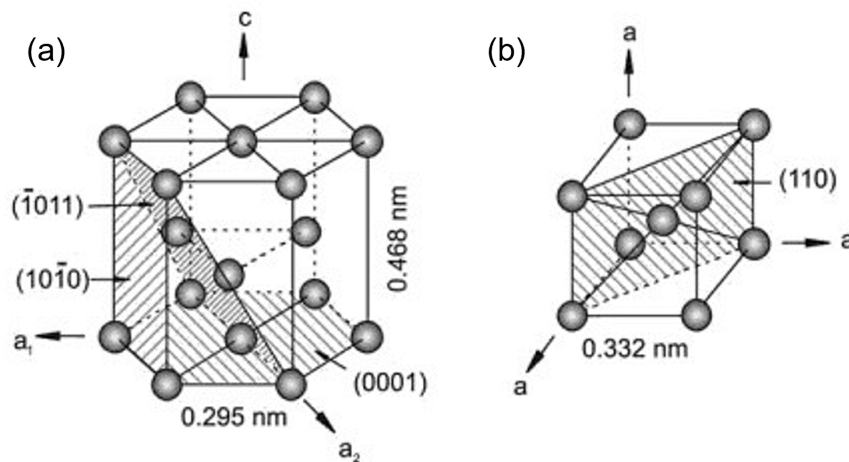


Figure 1: Titanium's (a) hcp α phase and (b) bcc β phase. Their most densely packed planes and directions are highlighted ([1]).

The exceptional properties of titanium are linked to the existence of both α and β crystal structures. For instance, plastic deformation is closely related to the material crystal

structure. The ease of plastic deformation increases from the hexagonal-close-packed (hcp) lattice to the body-centered cubic (bcc) one, thus explaining the limited plastic deformability of the hcp titanium compared to the bcc titanium [1].

A face-centered cubic (fcc) crystal structure has recently been observed in titanium alloys obtained through various processing. This discovery has stimulated research interest as such an exotic phase does not appear on the usual pressure-temperature phase diagram of Ti. The fcc titanium phase has first been observed upon depositing a thin Ti film onto a single NaCl crystal [3]. Subsequently, the epitaxial growth of such a crystal structure has been observed on various other substrates [3–7]. All these works show that Ti deposits with a fcc structure and subsequently transforms to the equilibrium α phase at a critical thickness of around 1-20 nm. Fcc-Ti has been documented to exist in Ti/Ni and Ti/Al multi-layers as well [8, 9]. In this context, the hcp to fcc transformation of Ti has been observed in ion milled cross-sections exploited for TEM studies. The fcc phase structure has been recently observed also in titanium alloys undergoing severe plastic deformation like milling, and rolling tensile deformation [10, 11]. Finally, the face-centered cubic phase of titanium has been theoretically assessed via first principle calculations [12]. The latter study shows that Ti allows for a locally stable fcc structure with a lattice parameter of about 4.11 Å. Moreover, it is predicted that the electronic structure for such an exotic phase significantly differs from that of its hcp phase.

The stress-induced phase transformation from hexagonal-closed packed to face-centered-cubic in titanium and titanium alloys has become a hot topic in materials science. Indeed, the stabilization of a metastable fcc-Ti phase has been at the center of scientific and technical debates [13]. Moreover, there is a marked interest in understanding the physical and mechanical properties of titanium various crystal structures because of the widespread applications associated with such a metal. Many studies have been carried out on the deformation mechanisms of commercially pure titanium to improve its mechanical properties [14]. The fcc phase of titanium has also been documented upon water quenching (WQ) of thin cold pressed Ti discs [14], compression testing [15] and tensile testing of thin films [16]. The existence of possible effects of interstitial elements is being debated [17]. Indeed, pure Ti is difficult to be processed because of its affinity to interstitial elements such as oxygen (O), nitrogen (N), carbon (C), and hydrogen (H) [18]. The stability of metastable fcc Ti phase (produced via ball milling) by hydrogen presence has been thoroughly investigated via TEM analysis [17, 19]. In this context, while a lattice parameter of around 4.22 Å has been observed in TiH_{0.67}, a pure Ti fcc phase with lattice parameter of about 4.10 Å has been produced due to the unstable crystallites under a TEM electron beam. This behavior suggests that the lattice parameter of the fcc phase of titanium is

highly dependent on the composition or the interstitial impurities (e.g., O, H, N) [13]. The lattice parameter of the fcc titanium phase generally varies between 4.00 Å and 4.50 Å, depending on the method of production. Ball milling has been widely exploited to produce fcc titanium as it introduces stresses in Ti powder particles while promoting particle refinement [13]. While this process promotes the formation of the fcc phase of Ti, it has been observed that such an exotic phase vanishes upon post heat treatment of the milled Ti powder [20]. This fact strengthens the idea that the fcc-Ti phase is unstable. However, ball milling of Ti powder mixed with stearic acid has yielded an fcc phase after annealing [18]. Furthermore, cold rolling of Ti has provided thin sheet comprised of a fcc phase with lattice parameter of about 4.09 Å [11], which is close to theoretical evaluations [12]. These findings are at the center of a debate on the stability of this fcc titanium phase [13]. Nonetheless, a stable TiN structure with lattice parameter of about 4.24 Å has been observed [21]. The lattice parameter of TiO_x vary and are predicted to be in between 4.08 and 4.89 Å [13].

It can be noted that the lattice parameter of the fcc Ti phase is found to be comparable with other fcc Ti compounds. Values of the lattice parameter of the fcc titanium phase documented in literature are listed in Table 1.

Recently, thin films (with thickness in between 200-500 nm) of titanium have been produced via pulsed laser deposition (PLD) at the Micro and Nano Structured Materials Laboratory (NanoLab) of the Energy Department of the Politecnico di Milano. Such films are found to be in a fcc structure and show a non negligible amount of oxygen contamination (up to 40%). Samples of various thicknesses have been obtained upon varying background pressure and fluence rate.

The aim of this thesis work is to characterize the thermomechanical properties of these thin films of exotic titanium structures, assessing the values of the elastic constants. This analysis is possible upon relying on Surface Brillouin Spectroscopy (SBS). The latter is a non destructive technique which exploits a laser source to investigate the acoustic properties of materials. Such an experimental technique is based on the study of the inelastic scattering of light when it encounters acoustic phonons in the sample (Brillouin scattering). This enables one to determine the velocities of surface acoustic waves through the analysis of the dispersion relations of acoustic modes obtained upon changing the laser incident angle on the sample. Computational algorithms allow retrieving the values of the elastic constants of the films from the observed experimental velocities measured.

The samples have first been analyzed through Energy-Dispersive X-ray Spectroscopy (EDXS) and X-Ray Diffraction (XRD) to retrieve information about their crystallographic

Lattice parameter (Å)	Process	Material	Reference
4.33	BM	Ti	[10]
4.24	BM	Ti	[20]
4.20	BM	Ti	[22]
4.29-4.10	BM + annealing	Ti + stearic acid	[18]
4.10	BM (TEM observation)	Ti	[19]
4.16	BM	Ti	[23]
4.40	Thin layer deposition	Ti/Ni	[8]
4.42	Thin layer deposition	Ti/Al	[9]
4.30	Thin foil/uniaxial tensile	Ti	[24]
4.31-4.33	Thin foil	Ti	[16]
4.30	Hot rolled/compression	Ti	[15]
4.15	Compression	Ti	[25]
4.11	First principle calculations	Ti	[12]
4.10	First principle calculations	Ti	[26]
4.16	Molecular dynamics	Ti	[27]
4.10	Sintered + WQ	Ti	[14]
4.09	Rolling	Ti	[11]
4.16	Thin film	Ti	[28]
4.20	Thin film/calculated	Ti	[29]
4.29	Thin film	Ti	[30]
4.12	Thin film	Ti	[31]
4.10	High-pressure torsion	Ti-6Al-4V	[32]
4.14	Repeated impact	Ti	[13]

Table 1: Values of the lattice parameter of fcc titanium (adapted from [13]). The values depend on both the process of formation of titanium and the material exploited.

conformation. This analysis also yields information about the lattice parameter of such thin films.

Chapter 1 of this thesis is devoted to a theoretical description of the propagation of acoustic waves in solids, to set the framework around which the Brillouin analysis is built. An introduction on the basics of continuum mechanics and theory of elasticity is first proposed. The focus is then put on elastic waves propagation in solids, and then on surface acoustic modes. Furthermore, the theory behind Brillouin spectroscopy is illustrated, alongside the main scattering geometry exploited in the experiments.

Chapter 2 provides a detailed description of the experimental set-up. The focus is placed

on the key elements of the instrumentation (i.e., the laser source and the Fabry-Perot interferometer). Finally, an overview on how samples are prepared and first characterized is proposed. Pulsed Laser Deposition's key elements are described to provide information about the production of the samples. Finally, the principles of EDXS and XRD are highlighted, alongside the key results of such studies.

Details of the methodology to characterize the samples are described in Chapter 3. The experimental results and analysis are also presented, alongside a comparison with results present in literature (see Table 1).

1 | Elastic Waves in Solids and Brillouin Spectroscopy Principles

The aim of this thesis is to assess the elastic properties of fcc titanium thin films. The elastic properties of materials are key to understand the ability of materials to deform in a reversible way. It is important to recall the basic elements of the theory of elasticity and continuum mechanics to gain enhanced understanding of elastic wave propagation in materials. Indeed, the elastic continuum model is appropriate to model materials at scales ranging from the supramolecular one (i.e., of the order of a few nanometers) up to the fully macroscopic one [33]. Key concepts such as strain and rotation tensor are introduced, alongside traction and the relationship between stress and strain. Finally, the elastic moduli (or constants) are introduced, focusing mainly on the hcp and fcc crystal structures (which are at the core of this thesis work). The main elements underpinning elastic waves propagation in solids are described, placing the focus on surface acoustic waves. The latter are key in Brillouin analysis. Finally, the main principles of Brillouin Spectroscopy are presented to provide the framework in which the experiments are conducted.

1.1. Elastic Waves in Solids

1.1.1. Continuum Mechanics and Theory of Elasticity

Figure 1.1 depicts the reference state R and deformed state D of a body in the (x_1, x_2, x_3) Cartesian coordinate system. Deformation of a body may occur due to applied forces or change in temperature. After reaching equilibrium in a given deformed state, such a state may evolve into a newly deformed state upon persisting external perturbations. The reference state of a body can conveniently be considered to be the initial stress-free configuration of the body, prior to any external disturbance [34].

In Figure 1.1 a generic point of the reference body (R) is denoted by vector $\mathbf{X} \equiv (x_1, x_2,$

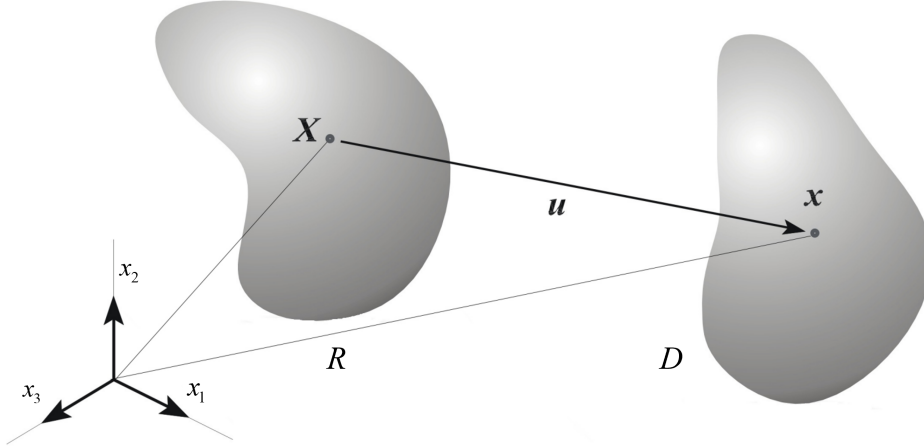


Figure 1.1: Transformation of a reference body (R) into its deformed state (D) in a (x_1, x_2, x_3) Cartesian coordinate system. Figure adapted from [35].

x_3). Upon applying an external perturbation, the body undergoes a deformation (D) and the given point is now identified by the position vector $\mathbf{x}(\mathbf{X})$, thus yielding a displacement

$$\mathbf{u} = \mathbf{x}(\mathbf{X}) - \mathbf{X} \quad (1.1)$$

where bold letters stand for vectorial quantities.

Under an elastic continuum hypothesis, a body can be sub-divided into infinitesimal elements with properties matching those of the bulk material. In this framework, if we consider small deformations, it is possible to describe displacements from R to D through regular and continuous functions. Thus, transformation of the reference body into its deformed state results from the movement of deformations of all the points of the body and the deformation of the initial point considered (in this case \mathbf{X}) [35]. The description by the continuous vector field of displacement is appropriate to model the behavior of materials ranging from a few nanometers upwards [33]. Going from the reference condition to the deformed state, the displacement gradient

$$U_{i,j} = \frac{\partial u_j}{\partial x_i}, (i, j) = 1, 2, 3 \quad (1.2)$$

can be written as

$$U_{i,j} = \epsilon_{i,j} + \omega_{i,j}, (i, j) = 1, 2, 3 \quad (1.3)$$

In Equation 1.3, $\epsilon_{i,j}$ is the strain tensor and represents the rate of change of the deformation of a body in the neighborhood of a certain point. $\omega_{i,j}$ is called the rotation tensor and describes the rigid rotation undergone by a body during the deformation [34]. While $\epsilon_{i,j}$ describes the symmetric part of $U_{i,j}$, $\omega_{i,j}$ is key to understand the anti symmetric components of the displacement gradient. Thus, it is possible to write

$$\epsilon_{i,j} = \frac{1}{2}(U_{i,j} + U_{j,i}), (i, j) = 1, 2, 3 \quad (1.4)$$

$$\omega_{i,j} = \frac{1}{2}(U_{i,j} - U_{j,i}), (i, j) = 1, 2, 3 \quad (1.5)$$

Deformation of a body takes place through an external perturbation (e.g., a force applied at a given point of the material). The force per unit area applied onto a surface of the body is called traction. To define traction at a given point P one needs to state on which surface, which includes that point, traction is defined (see Figure 1.2) [34].

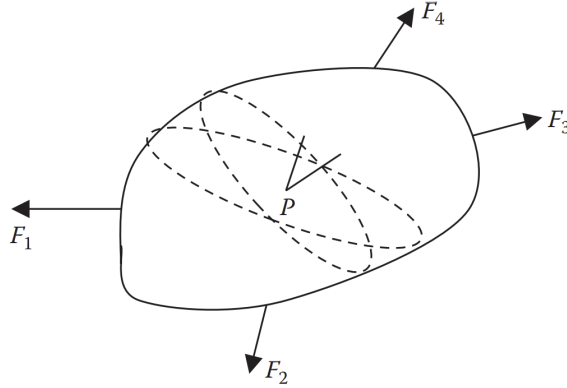


Figure 1.2: External forces F_i ($i = 1, 2, 3, 4$) applied to a body in equilibrium. Two exemplary planes passing through the point P and cutting the body into two halves are highlighted (from [34]).

The force per unit area in the neighborhood of point P is defined as the traction at point P and its value depends on the orientation of the surface on which the traction is defined [34]. Hence, to define traction at a point, one shall identify its three components alongside the plane on which it is defined. Traction can be denoted as $\mathbf{T}^{(\mathbf{n})}$, where \mathbf{n} is the unit vector normal to the plane on which the traction is defined. In a (x_1, x_2, x_3) Cartesian coordinate system, the three components of $\mathbf{T}^{(\mathbf{n})}$ correspond to the force per unit area along x_1 -, x_2 -, and x_3 -direction, respectively. Stress is similar to traction, both of them being defined as force per unit area. However, while the stress components are always defined normal or parallel to a surface, traction components are not necessarily normal or

parallel to the surface [34]. Stress components are described by two subscripts: the first subscript indicates the plane (or the direction normal to the plane) on which the stress component is defined and the second one corresponds to the direction of the force per unit area or stress value (an example is shown in Figure 1.3).

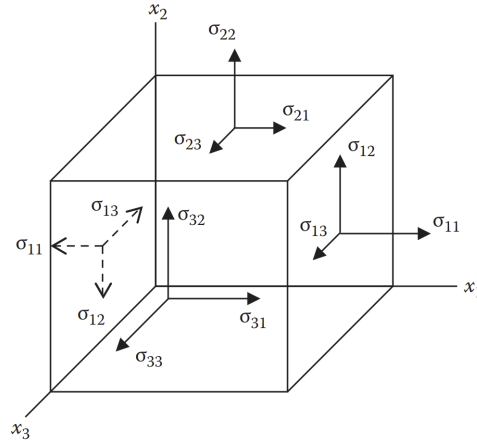


Figure 1.3: Stress components $\sigma_{i,j}$ ($i,j=1,2,3$) in a (x_1, x_2, x_3) coordinate system (from [34]).

Materials can be described as elastic or inelastic depending on their characteristic stress-strain relation (see Figure 1.4).

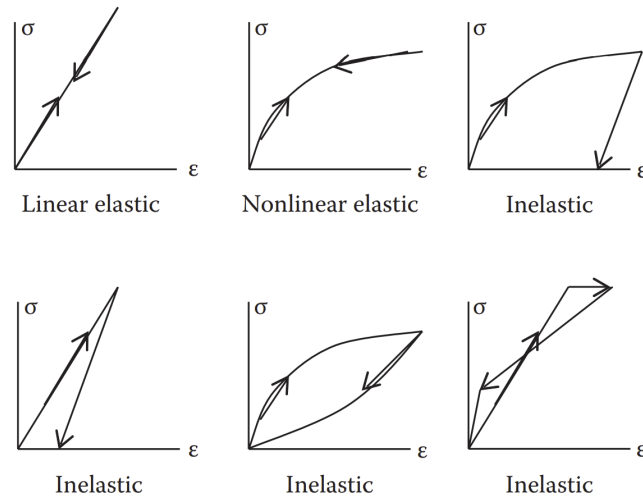


Figure 1.4: Stress-strain relations for elastic and inelastic materials (from [34]).

From Figure 1.4 it is possible to see that the material is called linear elastic if the stress-strain relation is linear. It is otherwise defined as nonlinear elastic material. However, it is important to highlight that if the stress-strain path is different during loading and unloading, then the material is no longer elastic even if the path is linear during

loading and unloading [34].

The following linear stress-strain relation (or constitutive relation) can be found for linear elastic materials

$$\sigma_{i,j} = C_{i,j,k,l} \epsilon_{k,l}, \quad (i, j, k, l) = 1, 2, 3 \quad (1.6)$$

where the coefficients $C_{i,j,k,l}$ depend on the material type and are called material constants or elastic constants. Equation 1.6 represents a general relationship between two second rank tensors, thus yielding a fourth order tensor characterized by 81 entries. However, since stress and strain tensors are symmetric, one has

$$C_{i,j,k,l} = C_{j,i,k,l} = C_{j,i,l,k} \quad (1.7)$$

thus reducing the number of index (i.e., i, j, k, l) combinations down to 36 [34]. In this framework, only 36 of the 81 elements of the fourth order tensor are distinguishable and can be represented through a 6×6 matrix.

The elastic constants matrix C is symmetric, thus leading to the following matrix relationship

$$\begin{bmatrix} \sigma_1 \\ \sigma_2 \\ \sigma_3 \\ \sigma_4 \\ \sigma_5 \\ \sigma_6 \end{bmatrix} = \begin{bmatrix} C_{11} & C_{12} & C_{13} & C_{14} & C_{15} & C_{16} \\ C_{21} & C_{22} & C_{23} & C_{24} & C_{25} & C_{26} \\ C_{31} & C_{32} & C_{33} & C_{34} & C_{35} & C_{36} \\ C_{41} & C_{42} & C_{43} & C_{44} & C_{45} & C_{46} \\ C_{51} & C_{52} & C_{53} & C_{54} & C_{55} & C_{56} \\ C_{61} & C_{62} & C_{63} & C_{64} & C_{65} & C_{66} \end{bmatrix} \times \begin{bmatrix} \epsilon_1 \\ \epsilon_2 \\ \epsilon_3 \\ 2\epsilon_4 \\ 2\epsilon_5 \\ 2\epsilon_6 \end{bmatrix} \quad (1.8)$$

Equation 1.8 generally describes the stress-strain relation for an anisotropic material (or triclinic material). Such a material has 21 independent elastic constants in the absence of any plane of symmetry. If the material response is symmetric about a plane or an axis, then the number of independent material constants is reduced [34].

This thesis focuses on the study of thin films of titanium. Titanium is found in nature in a hexagonal-closed-packed (hcp) crystal structure. An hexagonal material is characterized by one axis of rotational symmetry of order 6, in addition to three planes of symmetry. Such a material is also called transversely isotropic. Indeed, the rotational symmetry of order 6 is sufficient to guarantee isotropy for the elastic tensor in the plane orthogonal to

the axis. If in a (x_1, x_2, x_3) reference frame x_3 is the axis of symmetry, then the material response in x_1 - and x_2 -directions must be identical [34]. This assumption results in the possibility to reduce the number of elastic constants down to 6. In this case, Equation 1.8 becomes

$$\begin{bmatrix} \sigma_1 \\ \sigma_2 \\ \sigma_3 \\ \sigma_4 \\ \sigma_5 \\ \sigma_6 \end{bmatrix} = \begin{bmatrix} C_{11} & C_{12} & C_{13} & 0 & 0 & 0 \\ C_{12} & C_{11} & C_{13} & 0 & 0 & 0 \\ C_{13} & C_{13} & C_{33} & 0 & 0 & 0 \\ 0 & 0 & 0 & C_{44} & 0 & 0 \\ 0 & 0 & 0 & 0 & C_{44} & 0 \\ 0 & 0 & 0 & 0 & 0 & C_{66} \end{bmatrix} \times \begin{bmatrix} \epsilon_1 \\ \epsilon_2 \\ \epsilon_3 \\ 2\epsilon_4 \\ 2\epsilon_5 \\ 2\epsilon_6 \end{bmatrix} \quad (1.9)$$

Although Equation 1.9 includes 6 elastic constants, only 5 of them are actually independent, C_{66} being expressed as

$$C_{66} = \frac{C_{11} - C_{12}}{2} \quad (1.10)$$

because of rotational symmetry.

If the material is characterized by three planes and three axis of symmetry, Equation 1.8 becomes

$$\begin{bmatrix} \sigma_1 \\ \sigma_2 \\ \sigma_3 \\ \sigma_4 \\ \sigma_5 \\ \sigma_6 \end{bmatrix} = \begin{bmatrix} C_{11} & C_{12} & C_{12} & 0 & 0 & 0 \\ C_{12} & C_{11} & C_{12} & 0 & 0 & 0 \\ C_{12} & C_{12} & C_{11} & 0 & 0 & 0 \\ 0 & 0 & 0 & C_{44} & 0 & 0 \\ 0 & 0 & 0 & 0 & C_{44} & 0 \\ 0 & 0 & 0 & 0 & 0 & C_{44} \end{bmatrix} \times \begin{bmatrix} \epsilon_1 \\ \epsilon_2 \\ \epsilon_3 \\ 2\epsilon_4 \\ 2\epsilon_5 \\ 2\epsilon_6 \end{bmatrix} \quad (1.11)$$

Equation 1.11 is characterized by 3 independent parameters and is used to represent a cubic structure. The latter can be modeled as an isotropic structure upon considering the following isotropy condition

$$C_{11} - C_{12} - 2C_{44} = 0 \quad (1.12)$$

In this framework, the number of independent elastic constants drops to 2.

Equation 1.11 describes the stress-strain relation of a cubic crystal. Face-centered cubic

(fcc) films of titanium are the main focus of this thesis work. Their elastic properties are fully defined by the two elastic constants C_{11} and C_{44} , C_{12} being derived with the isotropy condition (Equation 1.12).

Deposited films are usually polycrystalline (with only a few exceptions). Regardless of the specific (point scale) anisotropy of the grains of the film, if grain orientations are purely random, then every small volume encircling a certain number of grains is statistically isotropic. Thus, the material behaves as an isotropic structure at such scale. This hypothesis applies to the study of the thin films of titanium in this thesis. Indeed, the analysis here presented is performed in the approximation of isotropic materials.

From the elastic constants, one can derive quantities which allow to thoroughly characterize materials. Such quantities are (i) Young's modulus (E), (ii) Poisson's ratio (ν), (iii) shear modulus (G), and (iv) bulk modulus (B). Young's modulus is a mechanical property that measures the tensile stress of a solid material when a force is applied lengthwise. For an isotropic material, (i) can be expressed as

$$E = C_{44} \frac{3C_{11} - 4C_{44}}{C_{11} - C_{44}} \quad (1.13)$$

The shear modulus G (also known as modulus of rigidity) links the shear stress to the shear strain and for an isotropic material is simply given by

$$G = C_{44} \quad (1.14)$$

The Poisson's ratio yields a measurement of the deformation (expansion or contraction) of a material along directions perpendicular to the direction of loading considered. For an isotropic material, ν is given by

$$\nu = \frac{C_{11} - 2C_{44}}{2(C_{11} - C_{44})} \quad (1.15)$$

Most materials are characterized by positive Poisson's ratio values, such that

$$0 < \nu < \frac{1}{2} \quad (1.16)$$

Another important quantity to characterize materials is the bulk modulus, B . The latter assesses the resistance of a material to compression. It links the applied hydrostatic stress

to the relative change of the volume of the material and for isotropic materials it is defined as

$$B = C_{11} - \frac{4}{3}C_{44} \quad (1.17)$$

The bulk modulus is a thermodynamic quantity which ought to be positive. From Equation 1.17, one retrieves the following condition for thermodynamic stability:

$$C_{11} > \frac{4}{3}C_{44} \quad (1.18)$$

1.1.2. Elastic Waves Propagation

Elastic waves are generated whenever a transient stress imbalance is produced within or on the surface of an elastic medium and can be seen as small deformations propagating through the material at a given speed (c) and frequency (ω) [35, 36]. The elastic continuum model allows describing displacements and strains for homogeneous media as

$$\rho \frac{\partial^2 u_j}{\partial t^2} = \sum_{i,k,l} C_{ijkl} \frac{\partial^2 u_k}{\partial x_i \partial x_l}, j = 1, 2, 3 \quad (1.19)$$

Equation 1.19 is called the elastodynamic equation and holds in the hypothesis of absence of body forces [33].

The key hypothesis of the elastic continuum model is the presence of an infinite medium [33]. An infinite homogeneous medium is symmetric to any translation in position and in time. The fundamental excitations described by Equation 1.19 are thus waves that are periodic in time and in space. Periodicity in space is best described by the wavelength λ or by a wavevector \mathbf{k} associated with the propagating wave, where $|\mathbf{k}| = 2\pi/\lambda$. The fundamental solutions of Equation 1.19 are thoroughly described by dispersion relations $\omega(\mathbf{k})$, which are determined by the properties of the medium [33]. An infinite medium does not have intrinsic length scale from the geometrical point of view since it is not characterized by an upper limit of size. In this context, the wavelengths (λ) of the propagating elastic wave range continuously up to infinity and the corresponding angular frequencies range from null frequencies (i.e., $\lambda \rightarrow \infty$) up to a not sharply defined upper limit (i.e., up to the shortest meaningful wavelengths) [33]. In the absence of intrinsic length scales, the dispersion relations are linear (i.e., $\omega = c|\mathbf{k}|$). In an infinite elastic solid, velocities do not depend on the direction of the wavevector and elastic waves can propagate

in two different modes: P-wave and S-wave mode (which are known as body or bulk waves) [34]. For such waves, it is possible to link the values of wave speed and frequency to the elastic constants of the materials in the following way. An elastic wave propagating as the P-wave (or longitudinal wave) causes only normal stresses (compressional or dilatational) to be generated in the solid, and the wave propagation speed is

$$c_P = \sqrt{\frac{C_{11}}{\rho}} \quad (1.20)$$

where ρ is the mass density of the material.

S-waves (or transverse waves) propagation causes only shear stress to be generated as the applied stress field is parallel to the free surface. Such a perturbation will propagate with a velocity

$$c_S = \sqrt{\frac{C_{44}}{\rho}} \quad (1.21)$$

While P-waves modify the volume of the material traversed, S-waves only act on the shape of the object [35].

The properties of bulk waves can be retrieved exploiting Equation 1.19. In an infinite medium, the simplest solution to Equation 1.19 is given by a plane wave of the form

$$u_j = U_j e^{ik(l_i x_i - c_{ph} t)} \quad (1.22)$$

where \mathbf{U} is the polarization vector, with components U_j . The phase velocity of the bulk wave (c_{ph}) is measured along the propagation direction defined by \mathbf{k} (i.e., the wavevector associated with the bulk wave) and its direction cosines l_i . It is noted that \mathbf{k} , c_{ph} , and \mathbf{U} are related by the set of three linear equations, known as the Christoffel equations

$$(C_{ijkl} l_j l_l - \rho c_{ph}^2 \delta_{ik}) U_k = 0 \quad (1.23)$$

where δ_{ik} is the Kronecher delta and the summation over repeated indices is implied [34].

Non trivial solutions for Equation 1.23 can be found via the secular equation [35]

$$\det(\Gamma_{ij} - \rho c_{ph}^2 \delta_{ij}) = 0 \quad (1.24)$$

where

$$\Gamma_{jk} = \sum_{i,l=1}^3 \frac{1}{2} (C_{ijkl} + C_{ijlk}) l_i l_l \quad (1.25)$$

is the Christoffel tensor and is linked to the elastic constants [35].

Surface Acoustic Waves

When P- and S-waves meet a free surface or an interface, they undergo reflection and transmission [34]. However, some wave motions are confined near a free surface or propagating along the interface between different media as some kind of confinement has been introduced in the material (i.e., the interface). In this framework, surface acoustic waves (SAWs) are propagation modes of elastic energy along the free interface of a semi-infinite elastic medium [35]. A semi-infinite medium introduces a sort of confinement, thus causing a rupture of the infinite translational symmetry, whereas translation invariance in time is not altered. Consequently, the acoustic modes remain periodic in time and are associated with a frequency ω . Even the invariance of the medium to any translation in the plane of the surface is left untouched. As a consequence, the acoustic modes remain periodic in this plane, with a periodicity given by a wave vector $\mathbf{k}_{//}$ parallel to the surface. One could associated to such a wavevector a wavelength

$$\lambda_{//} = \frac{2\pi}{|\mathbf{k}_{//}|} \quad (1.26)$$

which is to be understood as “*the period along the direction of $\mathbf{k}_{//}$ of an acoustic excitation whose wave vector component is $\mathbf{k}_{//}$* ” [33]. Such a wavevector characterizes the propagation of SAWs. The displacement amplitude of SAWs exponentially decays into the material so that these waves are confined within approximately one wavelength from the surface [35].

In a (x_1, x_2, x_3) reference frame, where x_1 and x_2 are parallel to the free surface and x_3 is normal to such a surface and pointing outwards, surface waves decay for values of $x_3 < 0$. Solutions of Equation 1.19 can be retrieved recalling that wavefronts are orthogonal to wavevectors and can be represented by the following linear combination

$$u_i = \sum_{n=1}^3 C_n \alpha_i^{(n)} e^{ik\mu^{(n)}x_3} e^{ik(l_1x_1+l_2x_2-c_pht)} \quad (1.27)$$

where α_i and k are the amplitude of the wave and of the wavevector, respectively. l_1 and

l_2 are direction cosines and $c_{ph} = \omega/k$ is the phase velocity of a vibrational mode. μ is a parameter which must be taken in a way that for $x_3 \rightarrow -\infty$ the solution yields zero. The weights C_n are such that set of solutions in Equation 1.27 satisfies Equation 1.19 if

$$(\sigma_{3j})|_{x_3=0} = \left(\frac{\partial u_m}{x_n} \right) |_{x_3=0} = 0, j = 1, 2, 3 \quad (1.28)$$

Similar to the problem for bulk waves, upon inserting Equation 1.27 into Equation 1.19, one finds the following secular equation

$$\det(\Gamma_{ij} - \delta_{ij}\rho c_{ph}^2) = 0 \quad (1.29)$$

Thus, one finds a sixth-order equation in μ with c_{ph} acting as a parameter [35].

SAWs traveling along the surface of a semi-infinite medium are best represented by Rayleigh waves. These kind of acoustic waves are characterized by a velocity c_R such that

$$c_R < c_S < c_P \quad (1.30)$$

The Rayleigh wave displacement field decays exponentially with depth, with a decay length very close to $\lambda_{//}$. In a semi-infinite medium, it can approximately be said that the properties of the medium influence c_R up to a depth of $2\lambda_{//}$, thus setting a length scale [33]. In this framework, the Rayleigh wave is a probe which senses the properties of the medium up to that depth [33].

In media which are finite in at least one dimension with size d , it is the size of the object which supports the excitations to set a reference length scale [33]. Confinement of the acoustic wave to the surface is mainly determined by the ratio of the wavelength λ to the size d . The films considered in this work are titanium thin film supported by a silicon substrate of a few hundreds of μm thickness. These can be modeled as stratified media, where the layer thickness sets the characteristic size d . In this framework, bulk waves with $\lambda/d \ll 1$ and the Rayleigh wave with $\lambda_{//} \ll d$, are indistinguishable from those in a semi-infinite medium of the same material [33]. The semi-infinite model can be applied to model the substrate on which samples are produced (i.e., silicon). Indeed, a supported film with thickness above one micrometer already behaves as a semi-infinite medium [34]. In this framework, the acoustic waves velocity depends on the film thickness, the wavevector parallel with respect to the considered surface, and the properties of both

film and substrate [35].

The geometry exploited to study a supported film (as in the case of the samples analyzed in this thesis work) is sketched in Figure 1.5.

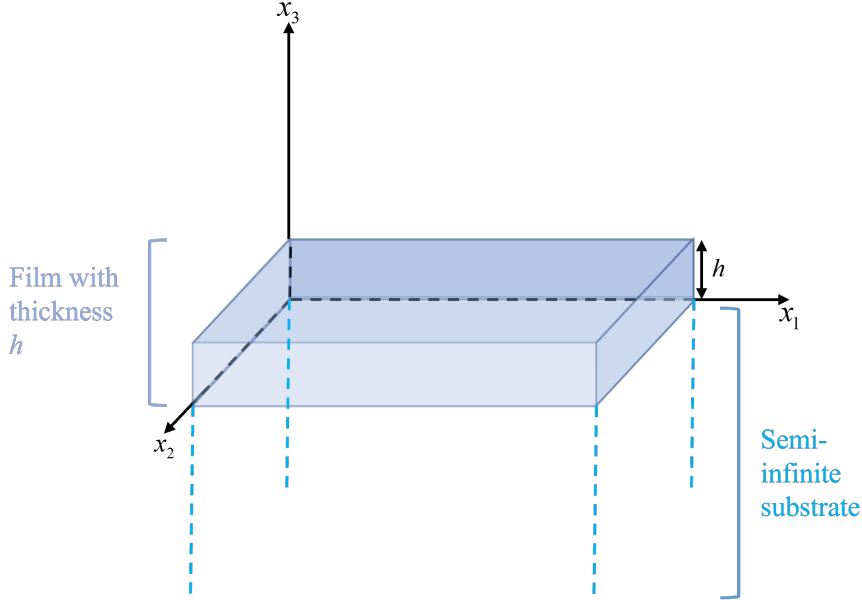


Figure 1.5: Sketch of the geometry of a film of thickness h supported by a semi-infinite substrate.

In the case of a film with thickness h supported by a semi-infinite substrate (Figure 1.5), the propagation of acoustic waves can still be modeled by Equation 1.19. However, boundary conditions have to be added to those previously described in the case of a semi-infinite medium (Equation 1.28). The complete set of equations used to describe wave propagation in a supported film is given by

$$\begin{aligned}
 \rho \frac{\partial^2 u_j}{\partial t^2} &= C_{ijkl} \frac{\partial^2 u_k}{\partial x_i \partial x_l} \\
 \sigma_{3j}^f \Big|_{x_3=0} &= \sigma_{3j}^s \Big|_{x_3=0} \\
 \mathbf{u}^f \Big|_{x_3=0} &= \mathbf{u}^s \Big|_{x_3=0} \\
 \sigma_{3j}^f \Big|_{x_3=h} &= 0
 \end{aligned} \tag{1.31}$$

where the superscripts s and f are used to identify the substrate and the film, respectively.

Upon solving the above set of equation as before, under the hypothesis of an elastic and isotropic medium, one finds the propagation modes in the sample (and thus the characteristic dispersion relations of the sample). The modes that can propagate in a

supported film are mainly distinguished into Rayleigh and Sezawa modes. While Rayleigh modes are linked with the first branch of the dispersion relations of the sample, SAWs travelling in a film made of a layer over a substrate give rise to Sezawa modes, which are linked to higher branches [34]. Sezawa modes result from the coupling of guided SAWs with the substrate's wave modes [35].

The properties of SAWs can be experimentally probed via Brillouin light scattering (BLS).

1.2. Brillouin Light Scattering (BLS)

1.2.1. Introduction

Brillouin light scattering (BLS) is a non-contact measurement technique that relies on light scattering to probe the properties of surface acoustic waves (SAWs) propagating at the surface of homogeneous solids or of thin layers (either supported or freestanding) [34]. Brillouin scattering technique is based on the spontaneous thermal fluctuations in the acoustic modes of the sample. Detection of acoustic modes is provided through local inelastic scattering of light.

Acoustic modes are vibrational excitations linked with the atomic motions. Vibrational excitations can be distinguished into acoustic and optical modes based on the phase difference between the motions of different atoms. While in an acoustic mode adjacent atoms vibrate in phase, an optic mode is characterized by adjacent atoms vibrating out of phase. In the case of acoustic modes of vibrations, the average displacement evaluated over a group of neighboring atoms fully represents the displacement of single atoms [33].

Thermal fluctuations in the acoustic modes are governed by the equipartition principle of thermodynamics. Such a principle states that at a given temperature T , each vibrational degree of freedom of a mechanical system is endowed with an average amount of energy $k_B T$, where $k_B = 1.38 \times 10^{-23}$ J/K is Boltzmann's constant. In an elastic continuum, the vibrational degrees of freedom are associated with acoustic modes of any wavevector [34]. Brillouin scattering geometry allows selecting a specific wavevector and probing the thermal noise (which is given by an incoherent superposition of all the acoustic modes) at that wavevector. The key component of the technique is a laser beam which illuminates the solid. Spectra of the scattered light are then analyzed to retrieve the dispersion relation of SAWs. The elastic properties of the sample are then retrieved from the dispersion relation. The laser is carefully selected not to cause excessive heating to the solid. Its power is fairly modest (usually less than a watt) and its wavelength λ_{laser} is taken such that $\lambda_{laser} \gg a$, where a is the sample's atomic distance. If such a condition is satisfied

(as in the case of visible light), the sample can be modeled as an elastic continuum. It is important to highlight that the laser does not cause any excitation in the sample, and is rather used as a simple probe.

The key consequences of the light scattering nature of BLS are the following. For starters, the technique is contactless. Thus, mechanical contact with the sample is not needed. Therefore, only optical access is required and this makes the technique particularly viable for environmental chambers for which only an optical window is required. Moreover, scattering occurs locally (in a volume of the order of tens of micrometers). This allows to fully exploit samples of this size making the technique most suitable for very thin samples. Finally, the acoustic wavelength is determined by the experimental conditions. Exploiting visible light, it is possible to probe submicrometric acoustic wavelengths, thus analyzing frequencies ranging from a few GHz up to several tens of GHz. Such small wavelengths allow to achieve high sensitivity to thin and ultrathin layers [34]. The interest in the characterization of the elastic properties of thin films relies on the observation that film properties can differ from those of the corresponding bulk material and can depend significantly on the film production process [34].

1.2.2. Scattering Geometry

The main scattering geometries exploited to perform Brillouin spectroscopy are (i) forward scattering and (ii) backscattering. In the following, we focus on the backscattering configuration, which is the geometry exploited through the experimental activity. The principles of backscattering geometry are sketched in Figure 1.6.

In Figure 1.6 a laser beam with a wavevector \mathbf{q}_i hits a surface at an angle θ to the normal. Most of the incident light is specularly reflected, refracted at angle θ' , or absorbed. A small amount of light undergoes inelastic scattering by a SAW because of thermally excited dynamic fluctuations in the strain field within the solid and dynamic rippling of the surface [34]. The inelastically scattered light is characterized by a shift in frequency of the order of $c_{acoust}/c_{light} \sim 10^{-5}$, c_{acoust} and c_{light} being the acoustic wave speed and the speed of light, respectively.

In opaque materials (e.g., titanium films here analyzed) Brillouin scattering is constrained to the surface and is thus called Surface Brillouin Scattering (SBS). The latter is caused by dynamic surface corrugations which take place because of acoustic waves propagation. Such waves can be modeled as a superposition of harmonic modes traveling in different directions with c_{SAW} velocity. This peculiar mechanism is known as surface ripple scattering and is at the core of light scattering [35].

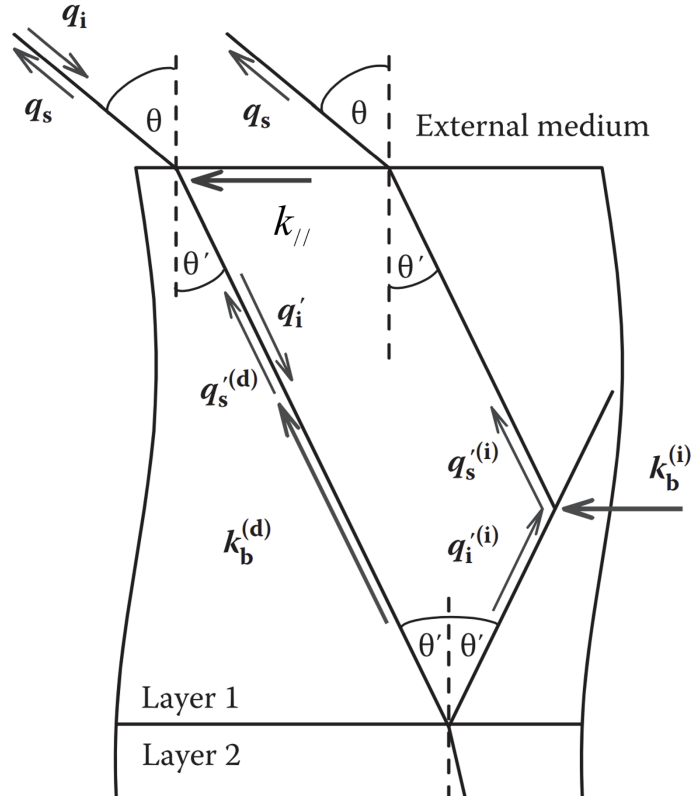


Figure 1.6: Backscattering by a SAW of wavevector $k_{//}$, direct backscattering by a bulk acoustic wave (i.e., acoustic waves occurring in the bulk of material) of wavevector $k_b^{(d)}$, and indirect backscattering by a bulk wave of wavevector $k_b^{(i)}$. q_i , and q_s are the incident and scattered wavevectors; $q_{i,s}$, $q'_{i,s}$ are the optical wavevectors in the external medium (vacuum) and in layer 1. Image adapted from [34].

Inelastically scattered light can be modeled as superposition of vibrational modes of any wavevector. Such components constructively interfere when the incident angle is such that

$$2\lambda_{SAW}\sin(\theta) = \lambda_{laser} \quad (1.32)$$

where λ_{SAW} is the wavelength associated with vibrational modes.

Alongside scattering, one finds that Doppler effect causes a variation in the scattered photons frequency f given by

$$\Delta f = \frac{c_{SAW}\sin(\theta)}{\lambda_{laser}} \quad (1.33)$$

The radiation scattered in a specific direction is then collected and analyzed yielding

the characteristic Brillouin spectrum. The latter is characterized by a relatively intense sharp central peak, unshifted in frequency, due to elastic scattering. Two mirror image sidebands straddling the central peak in the spectrum can also be observed. These are caused by the inelastic scattering of the incident light by thermal phonons. They are called Stokes and anti-Stokes bands and are associated with a frequency downshift and upshift, respectively. The part of the spectrum concerning Stokes and anti-Stokes bands depends on the optical and elastic properties of the sample, the scattering geometry, and the vibrational modes of the solid that the light is able to couple to [34]. An example of Brillouin spectrum can be seen in Figure 1.7.

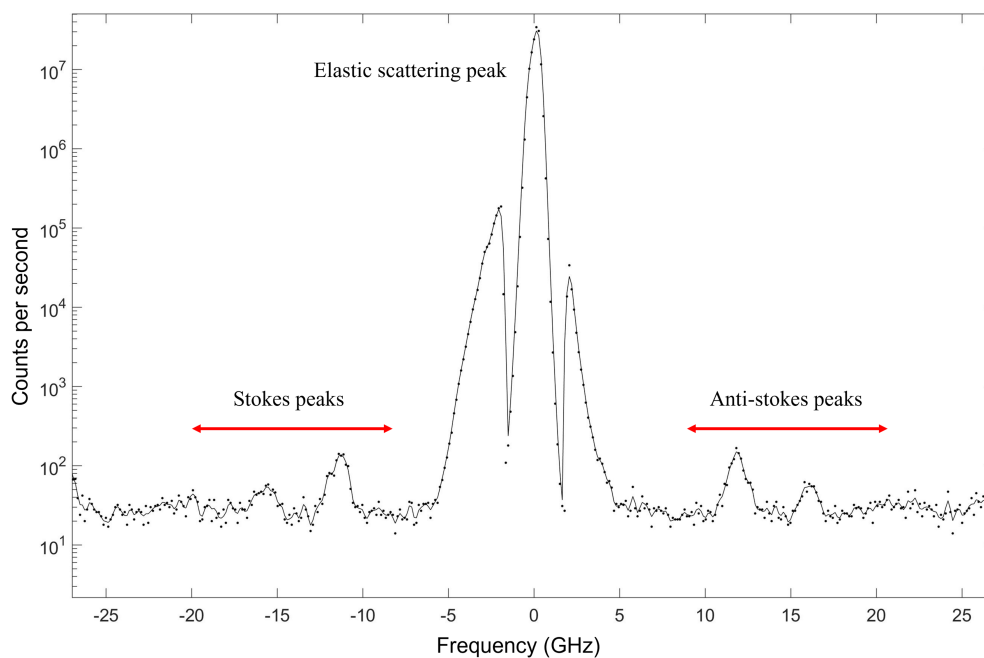


Figure 1.7: Example of Brillouin spectrum. The elastic peak and the Stokes/anti-Stokes events can be seen.

From Figure 1.7 two peak-like features can be seen in between -5 and 5 GHz, beside the elastic scattering central peak. The elastic peak intensity is much higher than that of the Stokes/anti-Stokes events. Thus, it has to be modulated to ensure the capability of the instrument to detect such small peaks. For this reason, a shutter is placed just before the interferometer. In this way, the elastically scattered light intensity is highly decreased. The two peak-like features in Figure 1.7 arise from the fact that the shutter operates a reduction of the elastic peak intensity. In the analysis performed in Chapter 3, the broad features near the elastic peak are not considered since they are related to the instrument set-up.

Brillouin scattering can be viewed either from a classical or a quantum mechanical point

of view. In a quantum mechanical picture, the scattering is interpreted as a phonon creation (Stokes) or annihilation (anti-Stokes) process, where energy is transferred in a phonon-photon interaction. In particular, the incident photon loses or gains the energy of the phonon giving rise to a Stokes and anti-Stokes event, respectively. In this framework, the Doppler effect (Equation 1.33) is present both in the energy absorption and emission happening during the phonon-phonon interaction, yielding a frequency shift of

$$\Delta f = \frac{2c_{SAW} \sin(\theta)}{\lambda_{laser}} \quad (1.34)$$

Equation 1.34 is exploited to link the acoustic waves' velocities to the measured frequency peaks in the Brillouin spectrum.

In quantum mechanics, each phonon carries a quantum energy of $\hbar\omega$ (where $\hbar = 1.05410^{-34}$ Js is Planck's constant and ω is the phonon frequency). For instance, the quantum of energy associated with an oscillator of 30 GHz frequency corresponds to an equivalent temperature $\hbar\omega/k_B T$ (where $k_B T$ is the thermal energy associated with each vibrational mode) of about 1.5K [34]. Thus, even at rather low temperatures, it is possible to adopt a classical approach to evaluate the Brillouin spectrum. In this framework, the classical and quantum mechanical approach become equivalent. It is only when $k_B T$ becomes comparable to $\hbar\omega$ (i.e., at extremely low temperatures) that quantum mechanical effects become highly relevant and a more sophisticated approach is required.

Backscattering Geometry

This thesis work relies on the use of backscattering by SAW. We can therefore focus only on such a mechanism (which can be seen in Figure 1.6). Figure 1.8 shows the backscattering configuration exploited to study opaque films.

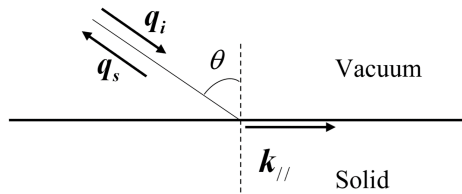


Figure 1.8: Brillouin backscattering geometry to study opaque films. Here, \mathbf{q}_i and θ are the incident wavevector and angle. \mathbf{q}_s , and $\mathbf{k}_{//}$ are the scattered and SAW's wavevector, respectively. Image adapted from [37]

In the configuration illustrated in Figure 1.8, the scattered light has frequency Ω_s and wavevector \mathbf{q}_s . Analysis of this radiation is performed considering a small cone of wavevec-

tors revolving around the incident wavevector \mathbf{q}_i [35]. Since the frequency shift is fairly small (see above), the frequency of the surface acoustic wave is given by

$$|\omega| = |\Omega_s - \Omega_i| \ll \Omega_i \quad (1.35)$$

Thus, the incident and scattered wavevectors can be approximated as

$$\mathbf{q}_s \approx \mathbf{q}_i \quad (1.36)$$

As mentioned above, Brillouin scattering in opaque materials is constrained to the surface (giving rise to Surface Brillouin Scattering). Therefore, the SAW wavevector probed by the incident laser is limited to its parallel component only, in such a way that

$$\mathbf{k}_{//} = (\mathbf{q}_s - \mathbf{q}_i)_{//} = 2q_i \sin(\theta) \quad (1.37)$$

where q_i is the modulus of the \mathbf{q}_i wavevector.

Surface acoustic waves are thus centered at frequencies

$$\omega = \pm 2q_i \sin(\theta) c_{SAW} \quad (1.38)$$

The anelastic phonon-photon interaction gives rise to a variation of the SAW wavevector modulus of an amount

$$\Delta k_{//} = 2k \sin(\theta) \quad (1.39)$$

The surface acoustic wave velocity can thus be evaluated as

$$c_{SAW} = \frac{\lambda_{laser} |\Delta\omega|}{4\pi \sin(\theta)} \quad (1.40)$$

where $\Delta\omega$ is the frequency shift associated with the acoustic modes' peaks (as defined in Equation 1.38). It is important to highlight that $\Delta\omega$ highly depends on the incident angle θ (see Equation 1.38). Thus, the frequency peaks collected in the Brillouin spectrum vary depending on the angle θ . Stokes and anti-Stokes bands in the Brillouin spectrum are found at frequencies $\Omega_s = \Omega_i \pm \omega$.

2 | Experimental Set-Up and Samples Preparation

The Brillouin Light Scattering (BLS) experimental set-up exploited to analyze fcc-titanium thin films is presented in the following chapter. The focus is placed on the fundamental elements of the instrumentation (i.e., the laser source and the Fabry-Perot interferometer). Finally, key information about the production and first characterization of the samples are illustrated.

2.1. Experimental Set-Up

BLS experiments rely on the possibility to illuminate the sample with a laser beam. The light scattered in a given direction is then collected and its spectrum is analyzed. Experiments are conducted in air at ambient temperature and pressure, the sample being in the open and placed on an appropriate sample holder. The latter is secured on the optical table on which the whole apparatus is set up. Brillouin scattering experiments are intrinsically contactless, thus the only strictly required condition is optical access to the sample. A simple experimental set-up for Brillouin scattering measurements in backscattering geometry and at ambient pressure is shown in Figure 2.1. Backscattering geometry is widely adopted to measure scattering by surface waves (SBS).

In Figure 2.1, the laser beam is directed onto the specimen by a small mirror M1 (incidence mirror), and focused onto the specimen surface by a lens L1 (termed front lens). The very same lens also collects the scattered light, transforming light coming from the focal spot into a parallel beam. Such a beam is then sent to the spectrometer. Spatial filtering is performed by a pinhole. In this framework, the scattered beam is focused onto the pinhole P by a lens L2, and can then be reconverted to a parallel beam. A couple of steering mirrors can be inserted along the optical path to the spectrometer to provide additional degrees of freedom (these components are useful for alignment purposes). The signal is collected via a phototube. The key advantages of backscattering geometry are (i) the use of a single lens to focus the incident beam and collect the scattered light, and (ii)

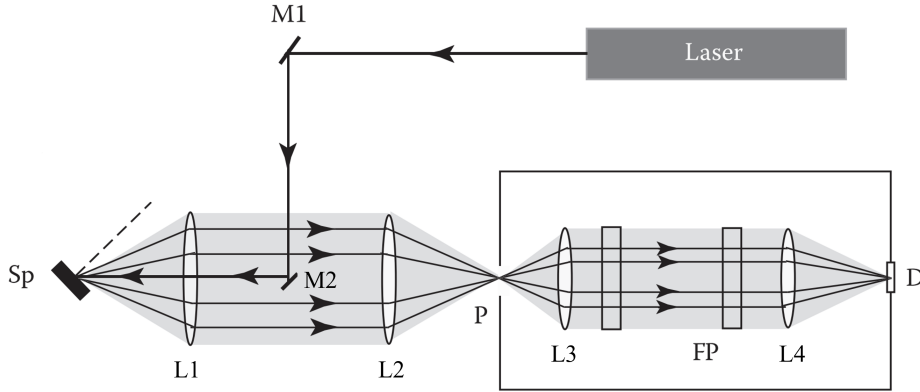


Figure 2.1: Typical experimental set-up for Brillouin spectroscopy in backscattering geometry. M1-M2 and L1-L4 are mirrors and lenses, respectively. Sp is the specimen. L2, P and L3 allow spatial filtering by the two lenses and a pinhole P. FP is the Fabry–Perot interferometer (for simplicity, a single interferometer is depicted, instead of the tandem multipass one). D is the light detector (typically a phototube). Light is focused and collected, in backscattering geometry, by lens L1. Image adapted from [37].

the minimization of elastically scattered light (at least for incidence not too close to the normal) as the collection direction is far from the specular reflection one [37].

A detailed description of the key components of the Brillouin apparatus at the NanoLab (Politecnico di Milano) is reported in the following. The focus is placed on the key components of the set-up, i.e., the laser radiation and the interferometer.

2.1.1. Laser Radiation and Optical Path

A frequency doubled Nd:YAG laser has been exploited for the experiments presented in this thesis work. It is produced by Laser Quantum and operates with green light ($\lambda = 532$ nm, $\nu \sim 6 \times 10^5$ GHz). The laser power exploited to study metallic films is of 200 mW to prevent damaging of samples. Vertically polarized laser light is selected via the presence of a quartz crystal [38].

The optical path followed by the laser beam is described in the following. Light hits on a beam splitter, which allows separation of primary and secondary radiation beams. While the former follows the optical path leading to the sample, the latter is an auxiliary bundle exploited for calibration and alignment of the interferometer (and is thus directly sent into the Fabry-Perot). It is important to highlight that the secondary beam is but a small fraction of the primary radiation. A half-wave plate is placed on the optical path of the primary beam to provide a sagittal polarization (i.e., a linear polarization with electric

field along the sample sagittal plane) of the incident radiation. The cross section between the incident radiation and the target acoustic modes is thus maximized. The radiation beam is then focused on the sample via a photographic lens. The sample is mounted on a rotating support that enables one to manually modify the incidence angle of the laser on the target. The focusing spot on the sample size is of the order of tens of micrometers so that the measurement is sensitive to the properties of the film in this area. Backscattered light is then collected by the camera lens and sent to a lens (i.e., focusing lens) that focuses light through a pinhole. The pinhole allows only light coming from the sample to enter the interferometer.

Figure 2.2 shows a picture of the optical path followed by the radiation.

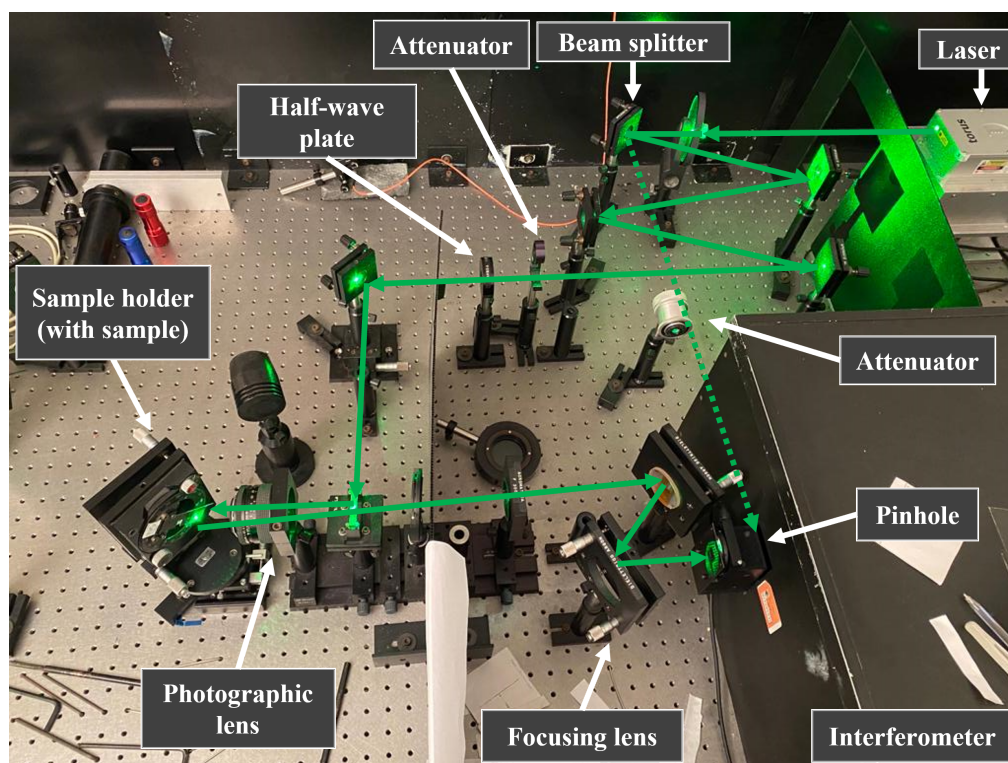


Figure 2.2: Optical path followed by the laser radiation. Attenuators are used to modify the intensity of light. The dashed and continuous lines represent the secondary and primary radiation beams, respectively.

2.1.2. Fabry-Perot Interferometer

The core of the experimental apparatus is the Fabry-Perot interferometer and is key for the analysis of Brillouin spectra (especially SBS ones). Indeed, the collected light contains an intense elastic peak at the incident frequency Ω_i and one (or more) weak doublet at frequencies $\Omega_i \pm \omega$ (see Chapter 1). The intensity of the low intensity doublets is several

orders of magnitude lower than that of the elastic peak, and the relative spectral shift ω/Ω_i for SBS goes down to 10^{-6} [37]. The spectral shift achieved with green light is typically of the order of 30 GHz or lower (which corresponds to exactly 1 cm^{-1}). The smallness of the frequency shift prevents analysis by dispersive means like diffraction gratings [37]. Scanning multipass Fabry–Perot interferometers achieve the required filtering performances and have become the standard choice to analyze Brillouin spectra.

The Fabry–Perot interferometer is an optical resonator which transmits only the light of its resonant wavelength, thus acting as a band-pass filter. Since its resonant frequency can be modified, it can be exploited to scan the spectrum to be measured [37]. Conventional Fabry–Perot interferometers are not able to achieve the contrast (i.e., the ratio between the maximum and minimum transmissivity) which is typically needed to resolve the weak doublets in Brillouin spectra. This is especially true for the SBS doublets [37]. A significant improvement in the interferometer configuration is achieved by multipassing the interferometer. In practice, two synchronized Fabry–Perot are coupled, thus avoiding the overlapping of different orders of interference. The most widespread multipass configuration adopted in Brillouin spectroscopy is a $3 + 3$ passes tandem interferometer (see below for a detailed description) [37].

The basics of operations of conventional Fabry–Perot and multipass interferometers are here summarized.

Single Fabry-Perot

Conventional Fabry–Perot interferometers are optical resonators (i.e., an optical cavities) made of two plane parallel partially reflecting mirrors, placed at a distance D from each other. Light entering the cavity is reflected back and forth and only the light of its resonant wavelength λ is transmitted. The Fabry-Perot interferometer thus acts as a band-pass filter. The interferometer resonant frequency can be adjusted by changing the distance between the mirrors. Therefore, such an optical resonator can be exploited to scan the spectrum to be measured [37].

For a given spacing D , the interferometer transmittance (T) is defined as the ratio of the transmitted to the incident intensity. A detailed analysis yields the following relationship

$$T = \frac{\tau_0}{1 + (4F^2/\pi^2)\sin^2(2\pi D/\lambda)} \quad (2.1)$$

where $\tau_0 < 1$ is the maximum possible transmission determined by losses in the system, and F (i.e., finesse), is a quality factor depending primarily on the mirror reflectivity and

flatness [39].

From Equation 2.1, one can see that only those wavelengths satisfying

$$D = \frac{1}{2}p\lambda \quad (2.2)$$

for integer values of p , will be transmitted. This is illustrated in Figure 2.3 [39].

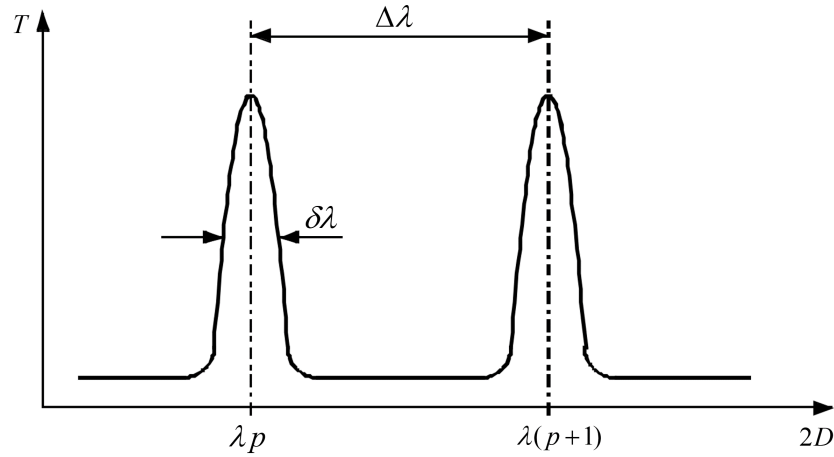


Figure 2.3: Fabry-Perot interferometer transmittance with respect to a given D mirror distance. Image adapted from [39].

The finesse F can be defined as

$$F = \frac{\Delta\lambda}{\delta\lambda} \quad (2.3)$$

where $\Delta\lambda$ and $\delta\lambda$ are the spacing between successive transmitted wavelengths (known as the free spectral range, FSR) and the width of a given transmission peak (i.e., its full width at half maximum, FWHM), respectively [39].

The free spectral range is defined as

$$\text{FSR} = \frac{c}{2D} = \frac{c}{\Delta\lambda} \quad (2.4)$$

where c is the speed of light in vacuum.

The finesse can further be expressed in terms of the mirror reflectivity R as [35]

$$F = \frac{4R}{(1 - R)^2} \quad (2.5)$$

A key quantity to describe the Fabry-Perot interferometer performance is the contrast C . The latter is defined as the ratio between the maximum and minimum value of the transmittance. From Equation 2.1, it turns out to be given by

$$C = \frac{1 + R^2}{1 - R^2} \quad (2.6)$$

An efficient Fabry-Perot interferometer allows for selective transmission of frequencies at FSR distance from each other. Moreover, a high value of the finesse is required.

During the experiments, the FSR is manually changed by acting on the mirror position. In this thesis work, a mirror distance of 5 mm is selected. This enables one to achieve a FSR of about 30 GHz. By selecting the mirror distance, one focuses on a specific transmission peak of the interferometer. Thus, the frequency range (\pm FSR) in which one operates is chosen to be higher than the largest frequency shift one aims at observing. The mirror distance can be modeled as

$$D = \bar{D} + \delta D \quad (2.7)$$

where \bar{D} is the mirror distance central value, which coincides with the maximum transmission (see Equation 2.1). Adjusting manually the mirror distance D to a central value \bar{D} allows the laser frequency $\Omega_i/2\pi$ to be transmitted [37]. The \bar{m} -th transmission peak coincides with the laser frequency

$$\bar{f}_m = \bar{m} \left(\frac{c}{2\bar{D}} \right) \quad (2.8)$$

which leads to

$$\bar{D} = \frac{\bar{m}\lambda}{2} \quad (2.9)$$

The free spectral range is thus set to

$$\text{FSR} = \frac{c}{2\bar{D}} \quad (2.10)$$

\bar{D} is then varied by a small quantity (usually by means of piezoelectric transducers), which corresponds to an order of interference. Thus, \bar{D} ranges in a $\pm\delta D$ interval such that

$$\delta D \leq \frac{\lambda}{2} = \frac{\bar{D}}{m} \quad (2.11)$$

The bounds of this interval are the $f_{\bar{m}-1}$ and $f_{\bar{m}+1}$ transmission peaks. At such frequencies the laser frequency is transmitted again. Therefore, by varying the macroscopic distance D , one produces also a shift in the peaks associated with a maximum transmission. In this way it is possible to scan all frequencies in the \pm FSR interval. The free spectral range slightly changes upon modifying the mirror distance. However, such a variation is of the order of tenths of micrometers with respect to a change in D of a few millimeters. Therefore, the FSR variation can be neglected. It is thus possible to analyze the spectral region centered around the elastic scattering frequency peak by slightly changing the mirror distance. The mirrors movement occurs via piezoelectric actuators. These allow changing the mirrors distance in a discrete way, thus scanning the whole free spectral range and keeping δD constant. The FSR is divided into many channels of the same amplitude, each associated to a different value of δD . During each acquisition, δD is kept constant for a given time, photons are counted and attributed to the corresponding channel, which remains open. The signals arriving to each open channel are then sent to the photomultiplier. This is typically operated in the single photon counting mode due to the low intensity of SBS doublets [37].

Counts are stored in a given channel, just to be transferred to the next one once the mirror distance is changed. The number of channels needed to perform a measurement is set by the value of the finesse F , which allows an insight on the instrumentation's resolution. It has been shown that the optimal number of channels n is given by $n > 2F$. In such a way, the maxima of the transmission function are better resolved and signal pile-up is less likely to occur [35].

The finesse is a parameter of each specific interferometer and does not depend on mirror distance. Thus, once the number of channels is fixed, the only parameter on which we can act for each measurement is the FSR (i.e., the mirror distance). The optimal choice of the FSR should not exceed twice the expected value of the frequency that should be measured [37].

Conventional Fabry–Perot interferometers do not achieve the contrast required to resolve the weak Brillouin doublets, especially the SBS doublets [37]. Indeed, the strongest signal is the one associated with the elastic light and is very close to the frequency peaks

associated with inelastic scattering. Thus, the tails of such a signal lead to a background signal which may obscure the weak doublets.

To effectively filter off the elastic peak contribution and improve the resolution of the weak doublets, multipassing techniques are adopted. Indeed, the contrast and the finesse are increased by passing the scattered light more times by the same interferometer. Moreover, a tandem configuration (i.e., a configuration in which two synchronized Fabry-Perot interferometers are exploited) is usually adopted to enhance the quality of the interpretation of the spectra. A detailed description of the tandem multipass Fabry-Perot interferometer is given below.

Tandem Multipass Fabry-Perot Interferometer

Sandercock was the first to show that the contrast can be improved by increasing the number of times the laser beam travels through the interferometer [34]. Such an operation is called multipassing.

Letting the radiation pass n times inside the interferometer, one achieves a contrast C_n given by

$$C_n = \left[\frac{(1 + R^2)}{(1 - R^2)} \right]^n \quad (2.12)$$

Thus, the contrast increases exponentially with the number of times the beam passes through the interferometer. However, one must take into account that the mirror's reflectivity is not ideal. Therefore, the signal gets slightly damped at each reflection. It has been shown that one should not go beyond values of $n = 5$ [35]. The instrumentation exploited for this thesis work exploits an interferometer which allows to multipass light 3 times.

Multipassing light n times allows also to increase the finesse as

$$F_n = \frac{F}{\sqrt{2^{\frac{1}{n}} - 1}} \quad (2.13)$$

The FSR can be increased while keeping the resolution fixed upon exploiting tandem interferometers [39]. In a single interferometer the $f_{\bar{m}}$, $f_{\bar{m}-1}$ and, $f_{\bar{m}+1}$ transmission peaks occur simultaneously, thus leading to an overlap of shifted replicas of the same spectrum and increasing the difficulties of the interpretation of the spectra [37]. Tandem configurations are thus used to separate transmission maxima. They exploit two synchronized

interferometers with slightly different FSRs. The $f_{\bar{m}}$ transmission peaks are made to coincide, thus increasing the overall transmissivity. Consequently, the $f_{\bar{m}-1}$ and $f_{\bar{m}+1}$ frequency peaks of the two interferometers do not coincide. Each of the interferometers cancels the transmission peaks of the other, avoiding spectra replicas [37] (see Figure 2.4).

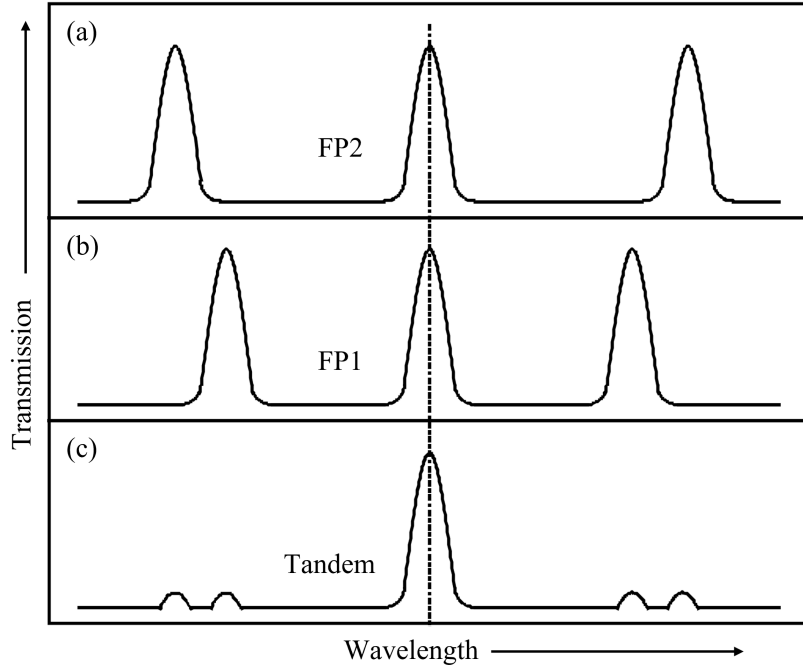


Figure 2.4: (a)-(b) Transmission in two Fabry-Perot interferometers FP1 and FP2 with different FSRs. (c) Transmission in tandem configuration (adapted from [39]).

The most useful arrangement is the so-called vernier system [39]. In such a system, the two interferometers FP1 and FP2 are characterized by a mirror spacing $L1$ and $L2$, respectively. $L2$ is chosen to be close to $L1$. The wavelengths transmitted by the interferometers combination must simultaneously satisfy

$$L1 = \frac{1}{2}p\lambda \quad (2.14)$$

$$L2 = \frac{1}{2}q\lambda \quad (2.15)$$

for integer values of p and q [39].

As shown in Figure 2.4, only the central peaks of FP1 and FP2 coincide, while the neighboring transmission peaks do not. Small "ghosts" of the intervening transmission peaks remain as the transmission of the interferometers never goes down to exactly zero (see Equation 2.1) [39]. Exemplary ghosts that are found in a common Brillouin spectrum are shown in Figure 2.5. Since ghosts result from the instrumentation configuration, they

will not be shown when analyzing data (see Chapter 3).

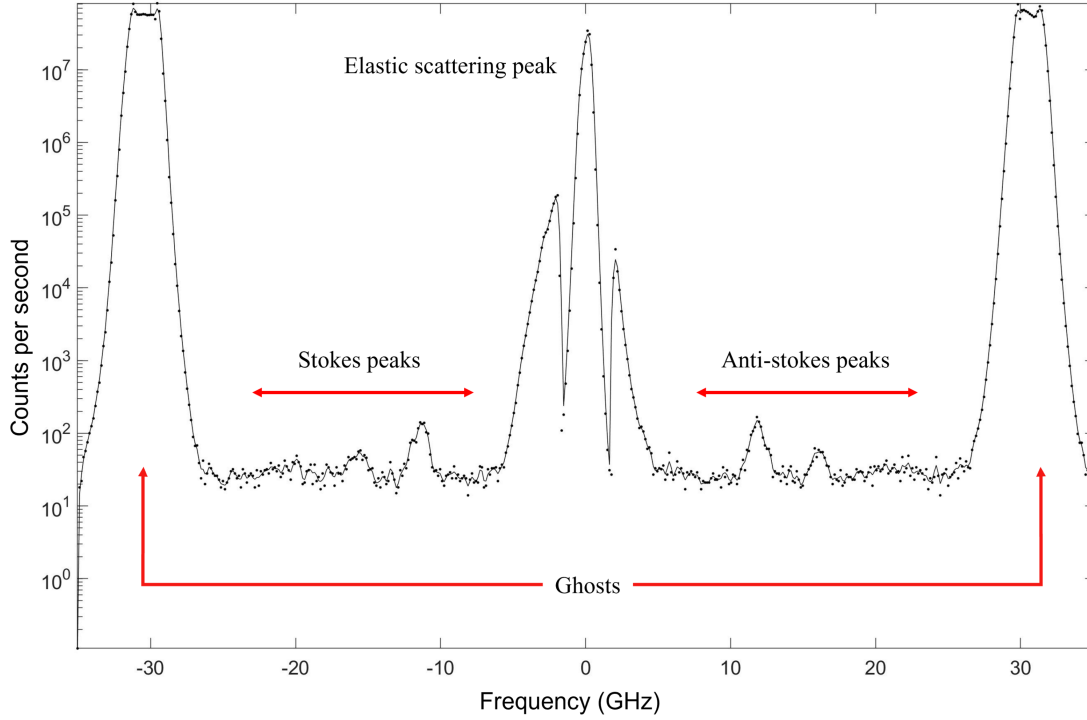


Figure 2.5: Exemplary ghosts due to instrumentation which can be seen in a typical Brillouin spectrum.

While the FSR of the tandem configuration increases, the resolution remains approximately constant. One should choose the values $L1$ and $L2$ in such a way that

$$F > \frac{L1}{L1 - L2} \quad (2.16)$$

to keep the ghost signal low. Commonly, one has $L2/L1 = 0.95$ [39].

The two interferometers must be synchronized to use the tandem configuration as a spectrometer. This can be achieved by simultaneously changing the spacings $L1$ and $L2$. To scan a given wavelength increment, the variations $\delta L1$ and $\delta L2$ must be such that

$$\frac{\delta L1}{\delta L2} = \frac{L1}{L2} \quad (2.17)$$

where $\delta L1$ and $\delta L2$ usually range from 1 to a few μm [39].

Practical implementation of tandem scanning interferometers must satisfy the static and dynamic synchronization criteria. The former implies that the spacings of the two inter-

ferometers are never allowed to depart from their correct relative values by more than 20 Å. The latter requires that correct relative spacings of FP1 and FP2 must be maintained over a scan of up to a few μm [39].

The aforementioned synchronization criteria are guaranteed upon using a single translation stage for both FP1 and FP2 (i.e., using a scanning tandem configuration). In this framework, the two mirrors are rigidly constrained to one another and are subject to the very same displacement (see Figure 2.6).

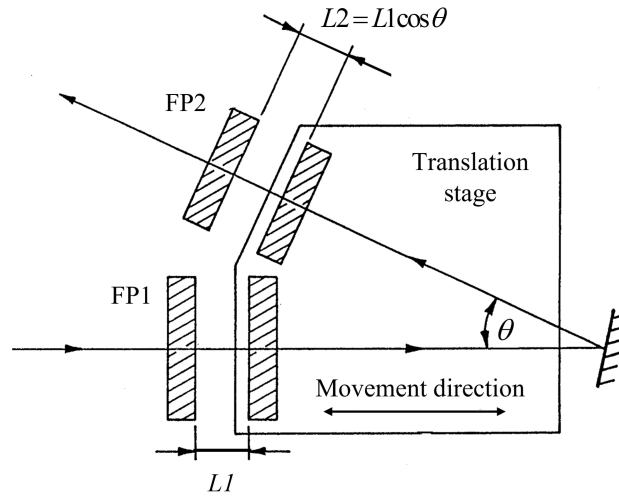


Figure 2.6: Exemplary scanning tandem configuration with two Fabry-Perot interferometers, FP1 and FP2, characterized by mirror distance $L1$ and $L2$, respectively. Image adapted from [39].

The first interferometer (FP1) is located along the direction of movement, with one of its mirrors placed on the translation stage. The latter consists of a parallelogram deformable via piezoelectric transducers, allowing movement of the mirror. The second interferometer (FP2) is set with its axis at an angle θ with respect to the scan direction. One of its mirrors is mounted on the translation stage and is kept in close proximity to the mirror of FP1. Moving the translation stage to the left draws both sets of mirrors near. The latter can come simultaneously in contact, although this situation is to be avoided not to damage the mirrors. In contrast, a movement of the translation stage to the right increases the spacings $L1$ and $L1 \cos \theta$. A scan $\delta L1$ of the translation stage causes a spacing variation of $\delta L1$ and $\delta L1 \cos \theta$ in FP1 and FP2, respectively. This arrangement allows satisfying Equation 2.17. In this framework, the two interferometers scan synchronously. The system design depicted in Figure 2.6 allows for (i) complete dynamic synchronization over a large scanning range and (ii) good static synchronization due to the fact that both interferometers share the same environment [39].

For the interferometer to work correctly, a vibration free environment is key. External perturbations could distort the mirror spacing, thus degrading the spectrum. To solve the issue of vibrations, there are usually two possibilities. It is possible to passively isolate the whole optical table by placing it on damping supports. However, a more effective solution relies on mounting the optical table rigidly on the floor, while isolating the interferometer from the optical table. The latter setting is termed active insulation. This can be achieved via dynamic isolation systems. These allow keeping the system isolated throughout the whole measurement window (see Figure 2.7).

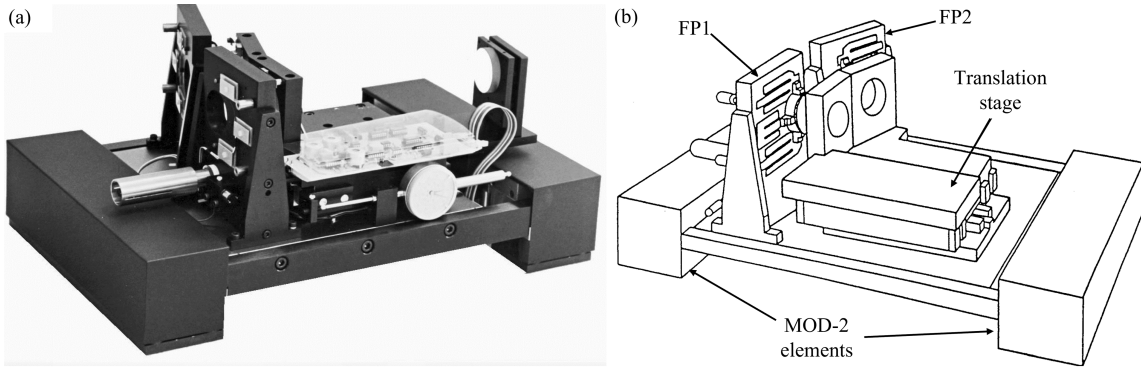


Figure 2.7: (a) Picture and (b) sketch of Fabry-Perot interferometers FP1 and FP2 supported by active isolation system MOD-2, characterized by two dynamical isolation mounts (MOD-2 elements). Image (b) adapted from [39].

The two Fabry-Perot and the optical components needed to multipass the interferometer are placed onto the isolation system. Pictures of the Fabry-Perot interferometers and of the optical components for multipassing are shown in Figure 2.8.

The interferometer is operated in a multipass tandem mode. Besides this measurement configuration, it is possible to switch the interferometer to an alignment modality. The tandem operation mode can be exploited provided that both interferometers have been pre-aligned in a parallel configuration and with the correct relative spacing [39]. These conditions can be fulfilled exploiting the optical components prior to the interferometers (see Figure 2.8 (a)). Light is first passed through a beam-splitter (Figure 2.9 (a)-(b)) and onto the first interferometer (FP1). The reflected light hits the second interferometer (FP2) thanks to a second beam-splitter. The beam, doubly reflected from FP2, goes to the photomultiplier. In this framework, light is assumed to be monochromatic. The key element on which pre-alignment relies is the fact that transmission through a Fabry-Perot is associated with a reflected intensity which tends to zero. The minimum value of the reflected beam is ideally obtained when interferometer is optimally aligned. The spectrum of the photomultiplier signal observed upon scanning the interferometer is characterized

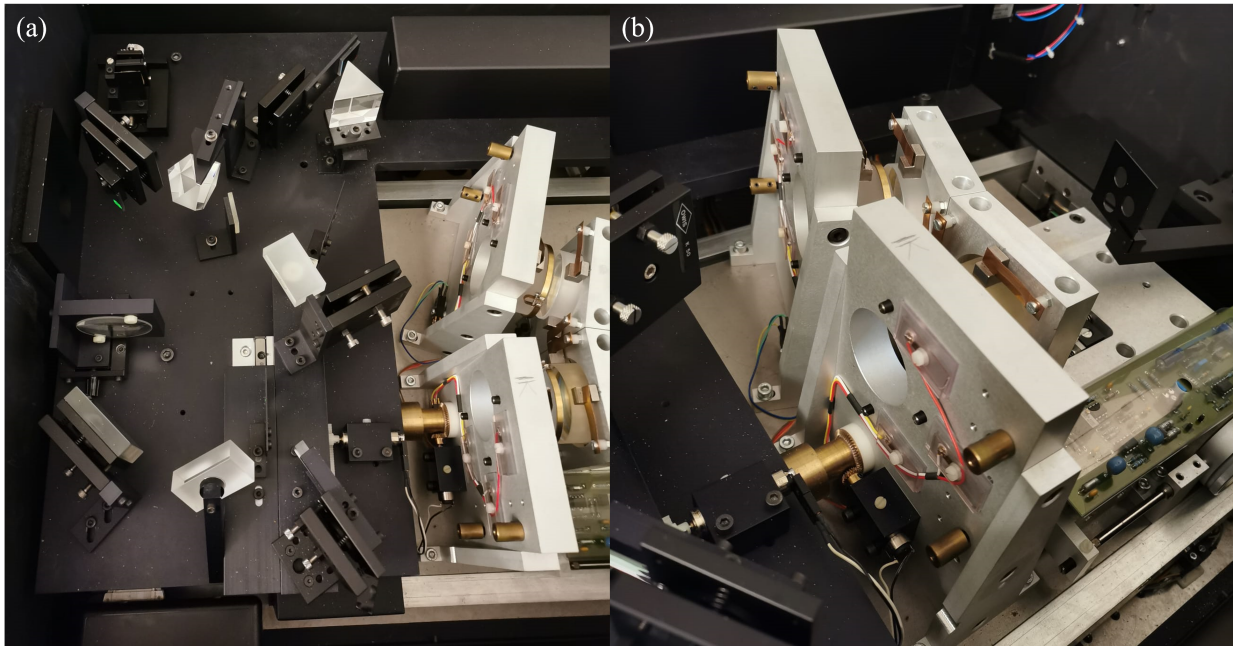


Figure 2.8: (a) Optical components for multipassing and (b) Fabry-Perot interferometers used in the laboratory experiments in the current thesis.

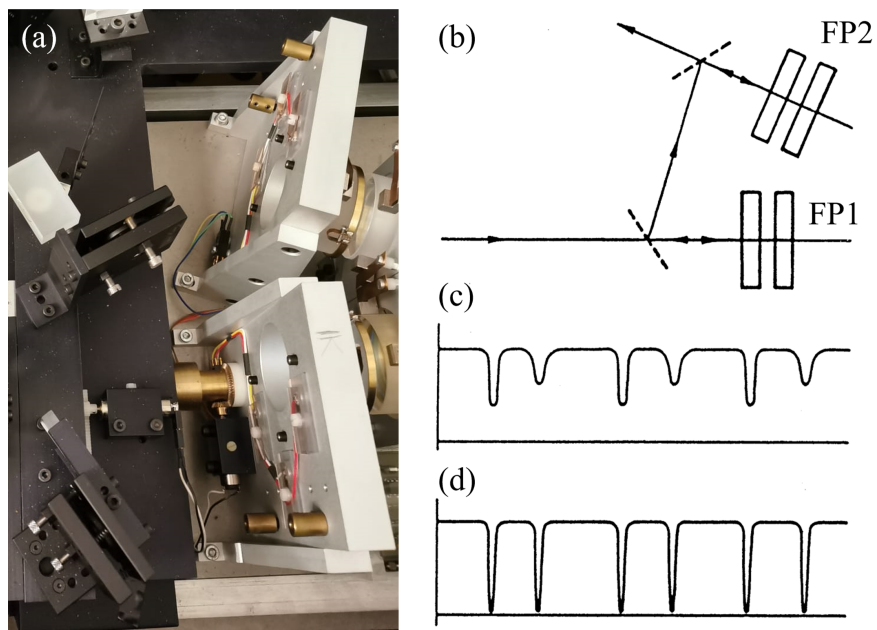


Figure 2.9: (a) Beam-splitters and Fabry-Perot FP1 and FP2 used in the laboratory experiments. (b) Scheme of alignment strategy. (c)-(d) Measured reflected intensity for two imperfectly and perfectly aligned interferometers, respectively. Images (b)-(c)-(d) are adapted from [39].

by minima whenever either FP1 or FP2 transmits. Two series of peaks are seen and are

associated with either FP1 or FP2 (Figure 2.9 (c)). Upon independently optimizing the alignment of FP1 and FP2, the minima approach zero (Figure 2.9 (d)).

The optimization of the interferometers alignment is achieved upon adjusting 5 degrees of freedom, namely X1, Y1, X2, Y2 and ΔZ (Figure 2.10).

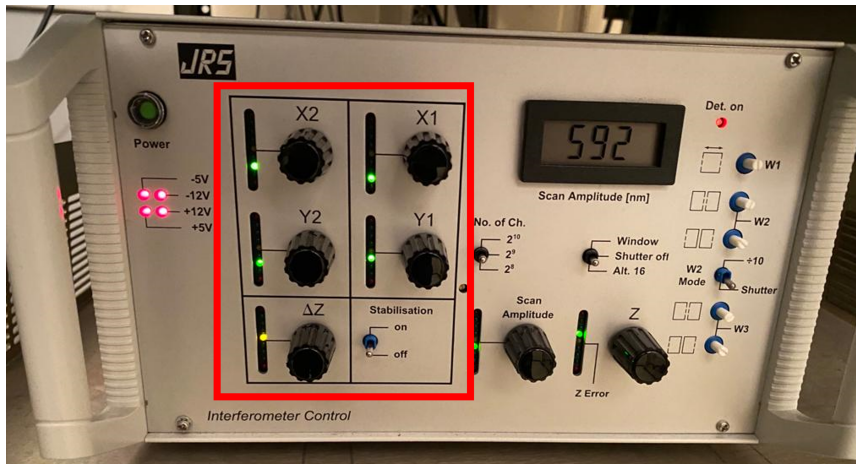


Figure 2.10: Interface of the interferometer control equipment. The 5 degrees of freedom X1, Y1, X2, Y2 and ΔZ are highlighted in red and used to maximize transmission of the interferometers.

While X1, Y1, X2, and Y2 are needed to improve the resolution of the minimum peak associated with FP1 and FP2, respectively, ΔZ allows changing the relative mirror spacing $L1 - L2$. The latter can further be optimized to ensure that a pair of peaks coincide. This final step allows to complete the pre-alignment of the tandem interferometer. It is finally possible to switch the optical system back to the multipass tandem measurement configuration. In this case, the transmission peak will be observed and can be optimized with only minor adjustments.

The optical system allows the interferometer to be used in a high contrast triple-pass tandem mode (3+3 configuration) [39]. This is a 3+3 configuration, as light is passed three time through each of the two Fabry-Perot interferometers. A schematic depiction of such a system is provided in Figure 2.11.

The light scattered from the sample enters the system through the adjustable pinhole P1. Only the cone of light defined by the aperture A1 is passed. Light is reflected by mirror M1 to the lens L1. Then, light is collimated and directed to FP1 via mirror M2. Here, a mask A2 is exploited. The beam passes through aperture 1 of A2 and is directed towards FP2 thanks to mirror M3. The 90° prism PR1 is hit by light and reflects the latter downwards. The beam goes back parallel to itself towards FP2. It travels through

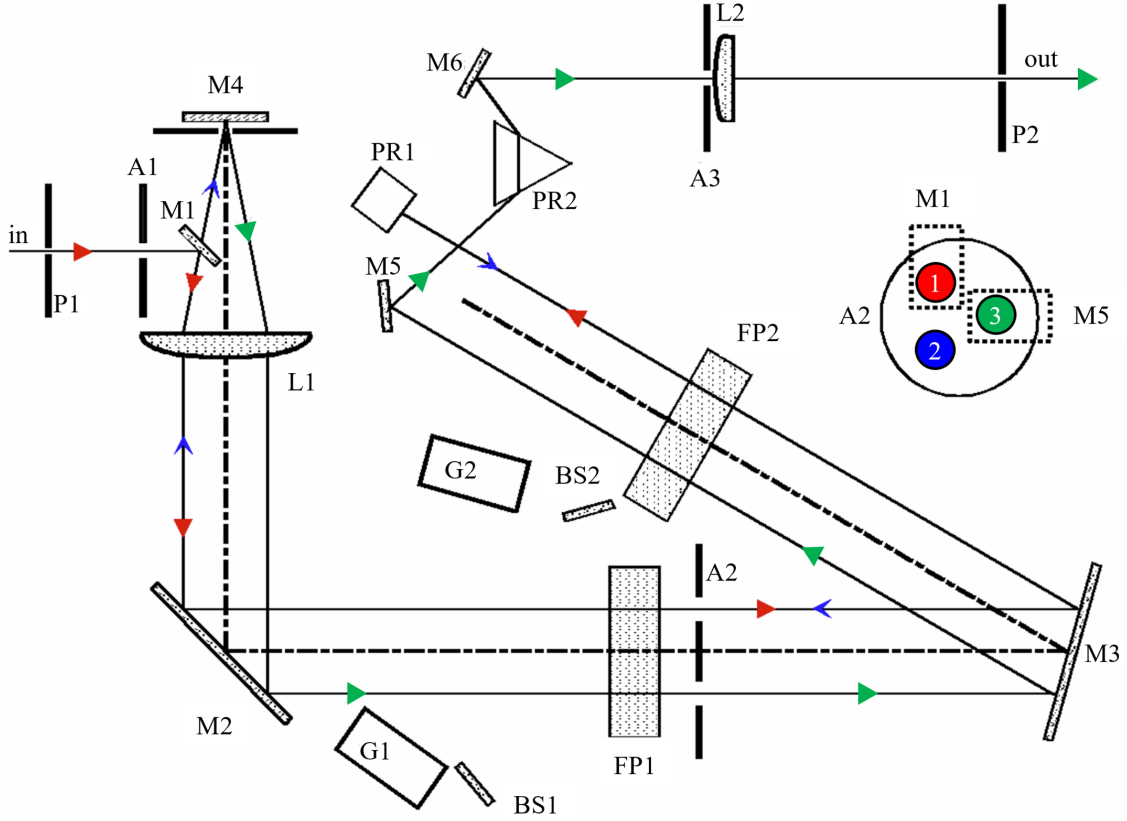


Figure 2.11: Scheme of the optics used in tandem multipass 3+3 configuration (image adapted from [39]). M1-M6 and L1-L2 are mirrors and lenses, respectively. A1-A3 are apertures. P1-P2 are pinholes, whereas PR1-PR2 are prisms. G1-G2 and BS1-BS2 are glassblock and beam-splitters, respectively, used in the alignment configuration (see below).

aperture 2 of A2 and back to FP1. After transmission through FP1, it hits lens L1 and is consequently focused onto mirror M4. The latter allows the light to go back through lens L1 where it is collimated and directed through FP1 once again. Combining lens L1 and mirror M4 lying at its focus allows filtering out undesired beams (e.g., beams reflected from the rear surfaces of the interferometer mirrors). Finally, light passes through the interferometers via aperture 3 of A2 and hits mirror M5. The beam travels to prism PR2. The combination of PR1, lens L2 and the output pinhole P2 gives rise to a bandpass filter with a width determined by the size of the pinhole. Mirror M6 allows sending light to the output pinhole.

When the system is switched from the tandem to the pre-alignment configuration, a translation stage moves the beam-splitters BS1 and BS2 into position (Figure 2.12). The glass block G1 shifts the light sideways leading it to hit FP1 in the centre. Light reflected

from FP1 and FP2 is shifted via the glass block G2 through the output path. Finally, light travels through the output pinhole and goes directly to the photomultiplier.

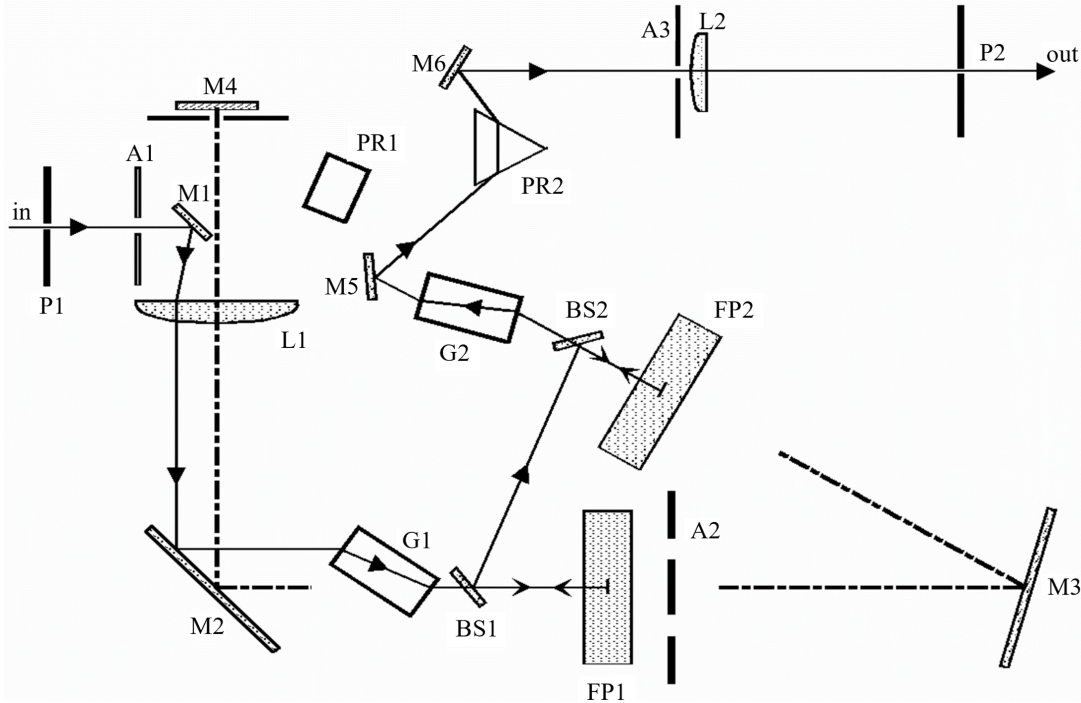


Figure 2.12: Scheme of the optical components used for alignment (image from [39]).

2.2. Samples Preparation

Samples are prepared via pulsed laser deposition (PLD). Such a technique allows deposition of thin films onto a substrate by manipulating deposition parameters (e.g., background pressure, fluence rate). The obtained samples are then characterized with Energy-Dispersive X-ray Spectroscopy (EDXS) and X-Ray Diffraction (XRD). In the following, a brief synthesis of the basic elements of PLD, EDXS, and XRD are reported.

2.2.1. Pulsed Laser Deposition

Pulsed laser deposition is a technique which exploits high-energy laser pulses to deposit thin-films. It vaporizes the surface of a solid target inside a vacuum chamber and then relies on the possibility to condense the produced vapor on a substrate. This procedure allows obtaining thin films with a thickness up to a few micrometers [40]. A scheme of pulsed laser deposition is depicted in Figure 2.13.

The key feature of PLD is that it relies on photon interaction between the incoming laser beam and the target. Following rapid explosion of the target surface region caused by

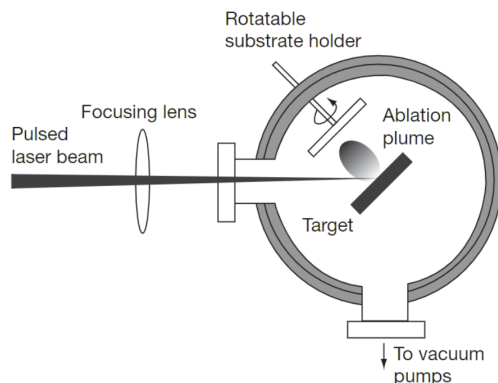


Figure 2.13: Sketch of pulsed laser deposition (image taken from [40]).

superheating, it is possible to create an ejected plume of material from any target. The plume of material has stoichiometry similar to that of the target, thus allowing to obtain the desired film. A key advantage in using PLD is the possibility to create thin films of a wide range of materials (e.g., metals, semiconductors, and insulators) by properly selecting laser operating conditions. Indeed, while the kinetic energies of ablated particles are high enough to promote surface diffusion, they do not induce bulk damage [40].

Samples structure has first been analyzed via Energy-Dispersive X-ray Spectroscopy (EDXS) and later on via X-Ray Diffraction (XRD).

2.2.2. Energy-Dispersive X-ray Spectroscopy Analysis

Energy-Dispersive X-ray Spectroscopy is a widely exploited technique for elemental analysis of a sample. It relies on the emission of characteristic X-rays from a specimen thanks to a high-energy beam of charged particles (e.g., electrons, protons). In this framework, a SEM electron beam is exploited. Such a beam is focused onto the sample and may excite an electron in an inner shell, ejecting it from the shell and creating an electron hole. An electron from an outer shell can fill in this hole upon emitting an X-ray. The number and energy of the X-rays emitted from a specimen yields information on the elemental composition of the specimen [41].

2.2.3. X-Ray Diffraction Analysis

XRD analysis is performed by a Panalytical X'Pert PRO X-ray diffractometer in $\theta/2\theta$ configuration [2]. A schematic representation of XRD is shown in Figure 2.14.

X-ray diffraction is a widespread technique to assess a sample's composition or crystalline structure. X-ray beams are sent through the sample at a given angle θ giving rise to

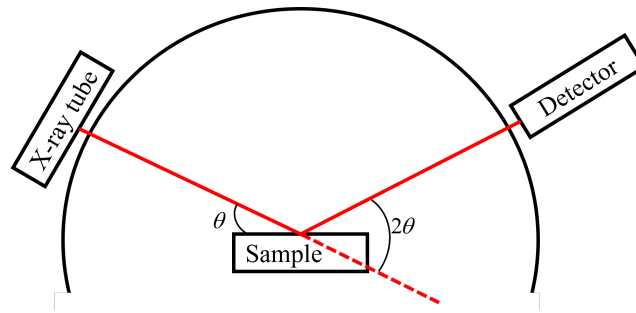


Figure 2.14: Schematic representation of X-ray Diffraction in $\theta/2\theta$ configuration.

diffraction. In particular, X-rays hitting the sample produce scattered waves. In a crystalline solid, the X-ray waves are scattered from lattice planes separated by a distance d between successive layers of atoms [42]. Scattered waves add constructively in specific directions determined by Bragg's law

$$n\lambda = 2d\sin(\theta) \quad (2.18)$$

where λ is the wavelength of the incident radiation (in this case Cu-K α) and n is an integer number.

The directions identified by Bragg's law appear as spots on the diffraction pattern and identify lattice planes. The latter are labeled in crystallography with three integers h , k , l , which are known as the Miller indices.

3 | Data Analysis

Titanium thin films (with thickness in between 200-500 nm) have been produced via pulsed laser deposition (PLD) at the Micro and Nano Structured Materials Laboratory (NanoLab) of the Energy Department of Politecnico di Milano. The samples are deposited on a Si wafer (with thickness of hundreds of μm) along the (1,0,0) (or equivalently (0,0,1)) crystallographic direction. The films seem to be showing a fcc crystal structure and are obtained upon varying (i) background pressure, (ii) fluence rate, and (iii) deposition time. Details of PLD deposition parameters associated with each sample are listed in Table 3.1.

Sample	Thickness (nm)	Fluence rate (J/cm ²)	Deposition time (s)	Background pressure (Pa)
Ti_02	238	8.79	1140	3.00×10^{-3}
Ti_06	450	4.42	6565	2.20×10^{-3}
Ti_15	400	7.50	2008	8.80×10^{-4}
Ti_16	191	7.52	1205	2.29×10^{-3}
Ti_24	209	3.80	2640	2.70×10^{-3}

Table 3.1: Thickness, fluence rate, deposition time and background pressure for samples produced via PLD. The denomination of titanium (Ti) samples is also reported. All samples are grown on a silicon substrate with thickness of the order of hundreds of microns.

Samples have first been analyzed via EDXS and XRD. In the following, key results obtained from such analysis are provided. Furthermore, Brillouin spectroscopy has been performed to assess the elastic constants of the film in Table 3.1. Experimental results are discussed and compared to findings available in the literature.

3.1. EDXS and XRD Analysis

3.1.1. EDXS Analysis

EDXS analysis reveals a non negligible percentage of oxygen in each sample. Key results of such analysis are listed in Table 3.2.

Sample	Oxygen percentage (%)
Ti_02	38.38
Ti_06	41.46
Ti_15	35.45
Ti_16	38.54
Ti_24	38.38

Table 3.2: Oxygen percentage found in samples through EDXS analysis. The denomination of titanium (Ti) samples is also reported.

The presence of interstitial impurity levels (e.g., H, O, N) and their effect on the fcc Ti crystal structure are discussed in previous studies [13]. Considering atomistic models to theoretically investigate the face-centered cubic TiO_x crystal structure, oxygen is suggested to be present with a percentage larger than 40%. Thus, scientists hint at the fact that the presence of oxygen (or hydrogen) in Ti fcc structures contributes to the stabilization of the fcc titanium phase [13].

The oxygen percentage retrieved from EDXS analysis is larger than 30% in all samples (see Table 3.2), a value compatible with theoretical analyses [13]. This element reinforces the idea that samples obtained via PLD are actually found in an fcc crystal structure.

3.1.2. XRD Analysis

Exemplary XRD spectra obtained for the analyzed samples are depicted in Figure 3.1. XRD spectra show the intensity of the signal for various angles of diffraction at their corresponding 2θ positions (i.e., the collection angle).

The crystal structure of titanium films and its dependence on film thickness has been explored in previous studies [28, 29]. The presence of the fcc phase of titanium has been observed for thin films (with a thickness up to circa 300 nm) [29]. It has been shown that titanium films gradually transform from fcc to hcp structure upon increasing the film thickness [28]. The fcc \rightarrow hcp phase transformation of polycrystalline titanium thin films of various thicknesses deposited on silicon substrate has been observed via XRD analysis [28]. The diffractogram obtained from the XRD analysis performed on such samples documents the appearance of several peaks of increasing intensity upon decreasing the film thickness. The peaks registered are associated with the fcc structure of titanium [28]. The crystal structure of thin films of titanium showing the fcc phase has been further studied in [29]. In this context, the obtained diffractogram is consistent with the

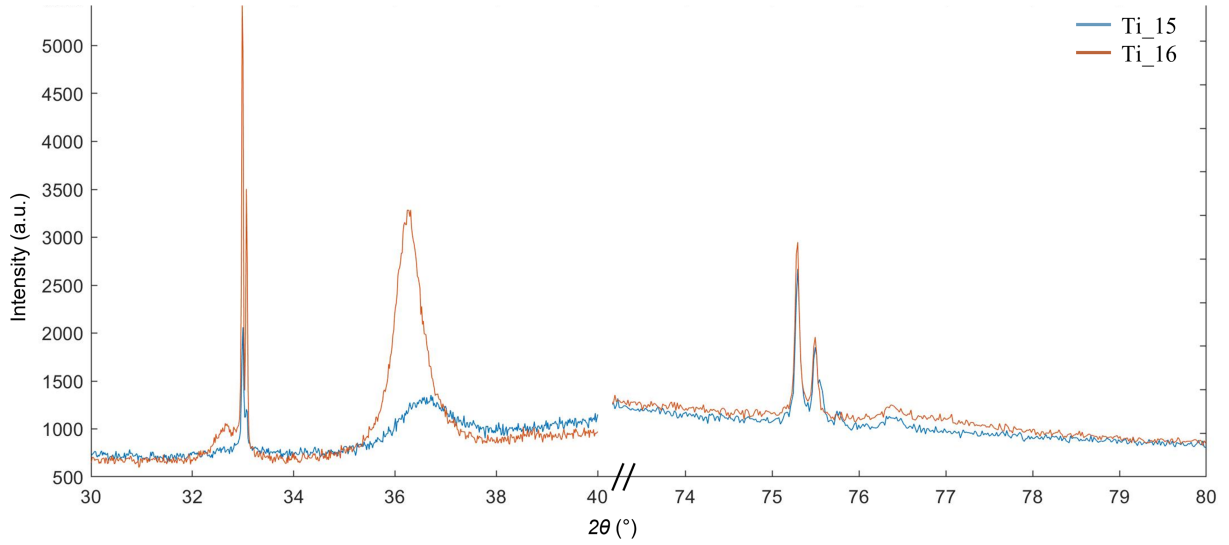


Figure 3.1: Example of XRD spectra obtained for Ti_15 and Ti_16 samples. Two peaks at circa 36° and 76° (characteristics of the fcc structure) can be seen. The sharp peak at 33° is associated with the Si substrate.

fcc-titanium structure documented in [28]. The XRD analysis presented in [29] shows diffraction peaks at positions $2\theta \sim 37^\circ, 79^\circ$. The two peaks are thus associated with the crystallographic direction identified by the Miller indexes (111) and (222), respectively.

From Figure 3.1 it is possible to observe two peaks at circa 36° and 76° . This estimate is in accordance with literature findings [28, 29] and reinforces the idea that the Ti films analyzed show a fcc crystal structure.

The peak positions are assessed through a fitting procedure with a Lorentzian function, yielding the values listed in Table 3.3. Model parameter estimates and the associated uncertainties are assessed through a Maximum Likelihood approach (see [43]).

From the position of the two peaks found via XRD analysis, it is possible to assess the value of the lattice parameter a of the crystal structure as

$$a = d\sqrt{h^2 + k^2 + l^2} \quad (3.1)$$

where d is the interplanar distance obtained via Bragg's law (Equation 2.18), and h, k, l are the Miller indexes associated with the considered lattice plane. It is possible to find a value of a for both directions (1,1,1) and (2,2,2). A final, representative value of a is then defined as the average between the two results.

The errors associated with d and a are assessed through a typical error propagation

Sample	2θ ($^{\circ}$)	hkl
Ti_02	36.361 ± 0.002	(1,1,1)
	76.88 ± 0.02	(2,2,2)
Ti_06	36.110 ± 0.003	(1,1,1)
	76.50 ± 0.01	(2,2,2)
Ti_15	36.70 ± 0.01	(1,1,1)
	76.38 ± 0.01	(2,2,2)
Ti_16	36.274 ± 0.002	(1,1,1)
	76.40 ± 0.02	(2,2,2)
Ti_24	36.361 ± 0.002	(1,1,1)
	76.88 ± 0.02	(2,2,2)

Table 3.3: 2θ positions obtained upon fitting XRD data with a Lorentzian function. The Miller indexes defining the crystallographic directions considered are highlighted. Since the XRD spectra of sample Ti_24 has not been measured, values of a sample of the very same thickness (Ti_02) are considered in this case.

formula. In general, given two independent variables x and y related, e.g., by a function $f = ax + by$, the error σ_f associated with f is given by

$$\sigma_f^2 = \left(\frac{\partial f}{\partial x}\right)^2 \sigma_x^2 + \left(\frac{\partial f}{\partial y}\right)^2 \sigma_y^2 \quad (3.2)$$

where σ_x and σ_y are the errors associated with x and y . Equation 3.2 holds also for nonlinear $f(x, y)$ functions.

Finally, it is possible to assess the value of the mass density associated with each sample as

$$\rho = \frac{m_{Ti} + m_O}{a^3} \quad (3.3)$$

where $m_{Ti}=47.867$ amu and $m_O=15.9994$ amu are the mass of titanium and oxygen, respectively. Samples are considered to be in a fcc crystal structure made by 4 titanium atoms and the oxygen percentage listed in Table 3.2.

The results obtained for a and ρ are listed in Table 3.4.

The results of the lattice parameters in Table 3.4 are compared to the values found in the literature and listed in Table 1 (see Figure 3.2).

Sample	Lattice parameter (Å)	Mass density (kg/m ³)
Ti_02	4.2900 ± 0.0004	4155 ± 1
Ti_06	4.3150 ± 0.0003	4107.4 ± 0.9
Ti_15	4.2800 ± 0.0008	4174 ± 2
Ti_16	4.3050 ± 0.0004	4098 ± 1
Ti_24	4.3100 ± 0.0004	4097 ± 1

Table 3.4: Lattice parameter and mass density of each sample obtained via XRD.

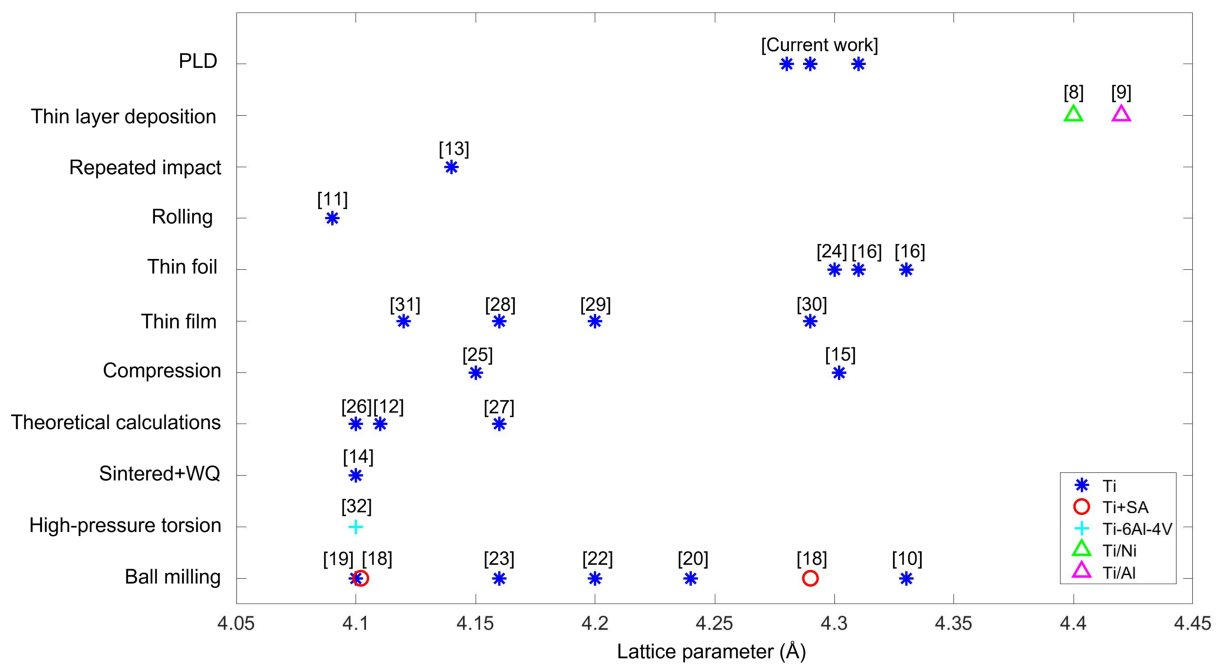


Figure 3.2: Comparison between literature values of lattice parameters (see Table 3.4) and those obtained through PLD produced samples. The techniques listed in Table 3.4 are here grouped for ease of interpretation. References listed in Table 3.4 are here used to label the lattice parameters values.

From Figure 3.2, it is possible to see that the parameters listed in Table 3.4 are in good accordance with the values in literature. This analysis supports the idea that the analyzed samples are found in a fcc structure.

3.2. Brillouin Spectroscopy Analysis

In the following, the methodology adopted to analyze data collected from Brillouin analysis is illustrated. Furthermore, the precision and accuracy of the results obtained are discussed. Finally, experimental results are thoroughly analyzed.

3.2.1. Methodology

A single Brillouin spectrum provides the circular frequencies ω of the observable spectral peaks [37]. The scattering geometry and the laser wavelength fully determine the wavevector $\mathbf{k}_{//}$ exchanged with SAWs (see Chapter 2). The experimental velocity of the surface acoustic waves (c_{SAW}) can be assessed as

$$c_{SAW} = \frac{\omega}{k_{//}} \quad (3.4)$$

where $k_{//}$ is the norm of the wavevector $\mathbf{k}_{//}$.

Multiple values of $\mathbf{k}_{//}$ are obtained upon changing the incidence angle. This procedure allows retrieving the dispersion relation $c_{SAW}(k_{//})$. The value of $k_{//}$ is assessed upon considering the incidence angle θ and the incident laser radiation (as described in Chapter 1). In the case of a film of thickness h , the propagation velocity depends on the norm of $\mathbf{k}_{//}$ through the (dimensionless) product $k_{//}h$ [37]. In this context, the dispersion relation is better identified by $c_{SAW}(k_{//}h)$.

The first step in the analysis of Brillouin spectra relies on a calibration procedure. Subsequently, it is possible to assess the value of the elastic constants of the material via computational algorithms based on a least square minimization procedure.

Calibration

The Fabry-Perot interferometer is operated in a tandem configuration (see Chapter 2) and supplies the raw Brillouin spectrum showing the photon count number as a function of the channel number [44]. The usual procedure adopted at the NanoLab to perform frequency calibration is based on the spectral ghosts. The latter originate from the imperfect suppression of transmission from adjacent orders in the tandem configuration. This occurs at the extrema of the FSR, when only one interferometer does not transmit the laser frequency. Instrumental ghosts typical of Fabry-Perot spectrometers rise at frequencies $\pm\text{FSR}$. Ghosts are useful for calibration purposes, once the distance among the mirrors is known [44]. The channel numbers n_p^+ and n_p^- are generally non-integer and are associated with the Stokes and anti-Stokes spectral peaks, respectively. Values of n_p^+ and n_p^- are identified by a best fit procedure (see below for a detailed description). The same procedure is applied to identify the channel numbers n_g^+ and n_g^- associated with the spectral ghosts [44]. The frequency shifts attributed to n_g^+ and n_g^- are given by $\pm\text{FSR}$ and the frequency shift f of a given spectral doublet is thus given by

$$f = \text{FSR} \frac{n_p^+ - n_p^-}{n_g^+ - n_g^-} \quad (3.5)$$

The calibration procedure is embedded in the software employed to retrieve experimental data.

Precision and Accuracy of the Experimental Results

Upon calibration of the spectra, Brillouin measurements allow assessing the acoustic velocities of surface waves obtained from each measured frequency shift Δf through

$$c_{SAW} = \frac{\lambda_0 \Delta f}{2 \sin \theta} \quad (3.6)$$

where λ_0 is the wavelength of the incident radiation and θ is the incident angle. Δf is related to the circular frequency ω as $\omega = 2\pi \Delta f$. $k_{//}$ is instead being evaluated as $k_{//} = 4\pi \sin \theta / \lambda_0$.

The precision and accuracy of these results are assessed in this section. The uncertainty associated with the laser wavelength λ_0 is negligible, the latter being a fixed value [37]. The frequency shift Δf , alongside its uncertainty $\sigma_{\Delta f}$, is assessed through a best fit procedure. The latter is performed through a software developed at the Nanolab of Politecnico di Milano. The software performs a least squares minimization taking into account the experimental backscattering geometry set. In backscattering configuration the lens collects light scattered together with all of the wavevectors within a cone around the scattered collection direction \mathbf{q}_s (see Section 3.2.1). In the case of SAWs, one is interested only in the wavevector component parallel to the sample surface (i.e., $k_{//}$). Values of \mathbf{q}_s and $k_{//}$ are related through Equation 1.37. The non linear nature of the latter leads to a broadening of the wavevectors cone around the scattered collection direction. The software developed at the Nanolab divides the collection cone in many segments and evaluates their contribution to the final frequency peak in terms of the parallel component of the wavevector. These contributions are then summed up. It is important to highlight that the light exactly backscattered is discarded through the use of a small mirror placed in front of the sample holder (see Chapter 2). Such a small mirror is necessary to focus the laser on the sample. Upon considering the finite collection aperture and the presence of the mirror, one finds an asymmetry of the peaks, which is only due to instrumental issues. The asymmetry of the frequency peaks provides a reference model for a best fit of the experimental peaks. The uncertainty on Δf mainly depends on the peak intensity.

Intense peaks are characterized by a good signal-to-noise ratio. Thus, the central value of the peak is identified with a very small uncertainty. The calibration procedure is key in determining the frequency scale of the measured spectra and is linked to a finite accuracy. The uncertainty associated with frequency calibration is usually negligible with respect to the uncertainty retrieved from the best fit procedure. Moreover, such an uncertainty can be completely neglected for the most intense and sharp peaks. The error associated with the calibration procedure can be assessed through the usual error propagation formula. Upon applying Equation 3.2 to Equation 3.5, one finds

$$\left(\frac{\sigma_f}{f}\right)^2 = \left(\frac{\sigma_{\text{FSR}}}{\text{FSR}}\right)^2 + \frac{\sigma_{n_p^+}^2 + \sigma_{n_p^-}^2}{(n_p^+ - n_p^-)^2} + \frac{\sigma_{n_g^+}^2 + \sigma_{n_g^-}^2}{(n_g^+ - n_g^-)^2} = \left(\frac{\sigma_{\text{FSR}}}{\text{FSR}}\right)^2 + \left(\frac{\sigma_p}{n_p}\right)^2 + \left(\frac{\sigma_g}{n_g}\right)^2 \quad (3.7)$$

where the last two terms are the relative uncertainties from the best fit procedures [44]. The first term in Equation 3.7 stems from the mirror spacing d , which is inversely proportional to the FSR. The relative uncertainty $\sigma_d/d = \sigma_{\text{FSR}}/\text{FSR}$ is usually below a micrometer over a few millimeters [44]. The term σ_p/n_p is associated with the peak doublet and mainly depends on the signal-to-noise ratio. While for strong peaks it is usually around 10^{-3} - 10^{-4} , it can rise to 10^{-2} for the weakest peaks [44]. The term σ_g/n_g is associated with the spectral ghosts and is always below 10^{-3} , though still above 10^{-4} due to the difficulty of adequately describe the peculiar shape of the double peaked ghosts [44].

The incidence angle θ is associated with an uncertainty σ_θ , which is related to the scattering geometry.

The uncertainty associated with the SAWs velocity c_{SAW} can be retrieved through the usual error propagation formula. Upon applying Equation 3.2 to Equation 3.6, one finds

$$\left(\frac{\sigma_{c_{\text{SAW}}}}{c_{\text{SAW}}}\right)^2 = \left(\frac{\sigma_{\Delta f}}{\Delta f}\right)^2 + \left(\frac{\sigma_{\sin\theta}}{\sin\theta}\right)^2 \quad (3.8)$$

Moreover, it is possible to show that

$$\frac{\sigma_{\sin\theta}}{\sin\theta} = \frac{1}{\sin\theta} \frac{d\sin\theta}{d\theta} \sigma_\theta = \frac{\sigma_\theta}{\tan\theta} \quad (3.9)$$

showing that the uncertainty σ_θ has more severe effects at small incidence angles [37]. In this thesis work, the incidence angle is changed manually. The error associated with such a procedure can be assessed as 0.5° . Indeed, the error related to the placement of the

sample holder at the correct angle cannot be higher than 1° (as a 1° angle would be easily detected) while being higher than the 0.2° error one would get upon using a mechanical rotator [44].

It is important to highlight the different natures of the uncertainties. We denote $\sigma_{\Delta f}$ as the random error associated with the identification of a peak frequency and σ_θ as the uncertainty caused by the random errors in setting the scattering geometry (in this case backscattering). Both errors are directly connected to each spectral peak. When considering different measurements, $\sigma_{\Delta f}$ and σ_θ are independent and uncorrelated. Furthermore, they tend to be averaged out by repeated measurements. Thus, they do not affect results (i.e., peak frequencies) in a mean sense. As such, while they characterize a lack of precision, they do not necessarily imply a lack of accuracy [37]. One must also consider that the sample holder is moved manually. Thus, σ_θ is characterized by a random error arising upon selecting the angle at which the sample holder is placed.

Finally, the peculiar shape of Brillouin peaks must be taken into account in the identification of peak frequencies. Indeed, the shape of the frequency peaks is due to the finite aperture of the light collecting lens. The lens collects light scattered with all wavevector directions falling within the solid angle delimited by the lens aperture, i.e., with all of the wavevectors within a cone around the scattered collection direction q_s . In backscattering geometry, this finite collection aperture produces an asymmetry of the peaks, which should be considered when determining the peak frequency [37]. This is taken into account through the best fit procedure exploited.

Least Square Minimization

The mechanical characterization of thin films relies on a least square minimization between the experimental and theoretical values of SAW velocities. Theoretical values of the velocities associated with the Rayleigh and Sezawa modes can be computed upon solving the Christoffel equation obtained from the set of equations in Equation 1.31. Thus, the films thickness and mass density are key to the evaluation of theoretical SAWs velocities. Sets of velocities $c_i^{comp}(C_j)$ can be theoretically computed as a function of one or more free parameters C_j (i.e., elastic moduli). The index i contains information on each branch of the dispersion relation of the sample and the wavevector $k_{//}$ at a given angle. Once experimental velocities c_i^{meas} are known, the sum of squared residuals is computed as

$$LS(C_j) = \sum_i \left(\frac{c_i^{comp}(C_j) - c_i^{meas}}{\sigma_i} \right)^2 \quad (3.10)$$

where σ_i is the standard deviation associated with each c_i^{meas} value and is determined upon fitting the experimental frequency peaks.

The key assumption made to exploit the aforementioned procedure is that the samples can be modeled as supported isotropic films, with titanium layers (i.e., films for which Equation 1.12 holds) and semi-infinite silicon substrate. Indeed, while Ti films are characterized by a thickness of few nm, the thickness of the silicon substrate is on the order of hundreds of μm . The least square procedure is in principle valid for any number of independent constants. The complexity of such a procedure increases with the number of constants to be assessed. In this thesis, the least square procedure is exploited in the simplest case of 2 independent elastic constants. Indeed, up to now there are no experimental evidences that the films are anisotropic. In this framework, the only independent elastic constants to be considered are C_{11} and C_{44} . Moreover, titanium films are modeled as perfectly adherent to the silicon substrate. It is thus possible to evaluate the theoretical velocities as a function of C_{11} and C_{44} to yield $c_i^{comp}(C_{11}, C_{44})$.

Equation 3.10 can be solved through a dedicated software. This procedure yields a graphical representation through multiple contour lines. These enable us to identify regions in the (C_{44}, C_{11}) parameter space associated with a given value of the least square error [35]. The aim of this analysis is to constrain the extent of the regions in the (C_{44}, C_{11}) space within which minimization of the difference between experimental and theoretical velocities can be easily performed. The most probable values of the elastic constants C_{11} and C_{44} are thus those which minimize Equation 3.10. The behavior of the LS estimator is best highlighted upon rescaling the contour lines with respect to the minimum value of Equation 3.10 in the (C_{44}, C_{11}) space. Thus, contour lines

$$\frac{LS(C_{11}, C_{44})}{LS_{min}} \quad (3.11)$$

are graphically depicted in such a way that their minimum value corresponds to 1.

The goal of the least square minimization analysis is to assess the most probable values of C_{11} and C_{44} . This is possible upon restricting the area identified by the contour lines in the (C_{44}, C_{11}) space by setting an appropriate confidence interval (i.e., a range of estimates of the unknown parameters). The latter depends on the number of experimental data. Furthermore, the confidence region (i.e., the generalization of the confidence interval in a multi-dimensional plane) is evaluated in terms of the variable parameters (in this case the elastic constants C_{11} and C_{44}) and the number of observable peaks [35]. Confidence regions associated with a random variable θ are defined through the Fisher-Snedecorr

probability distribution $F_{p,n-p}^\alpha$ as

$$\left\{ \theta = \frac{LS(\theta) - LS(\hat{\theta})}{LS(\hat{\theta})} \leq \frac{p}{n-p} F_{p,n-p}^\alpha \right\} \quad (3.12)$$

where α is the desired level of confidence [45]; p and n are the number of the target model parameters (in this case the two elastic constants) and of the experimental data, respectively; $LS(\theta)$ and $LS(\hat{\theta})$ correspond to the values of Equation 3.10 associated with the random variable θ and with the minimum value LS_{min} .

3.2.2. Results and Discussion

Samples listed in Table 3.1 are analyzed through Brillouin spectroscopy to assess values of the elastic constants C_{11} and C_{44} . The conditions under which the experiments are performed (i.e., the laser current, the scattering configuration, the ranges of angles analyzed, and the mirror distance) are detailed in the following. All spectra are acquired exploiting a backscattering configuration and analyzing angles ranging from 30° to 70° . The samples are placed along the (1,0,0) silicon crystallographic direction and are oriented in such a way that the probed $k_{//}$ wavevector is along the (1,0,0) direction. The pinhole aperture leading to the interferometer is set to $200 \mu\text{m}$ and the mirror distance is placed at 5 mm to scan a FSR of ± 30 GHz. It is important to highlight that the laser is not operated at its maximum current. Indeed, only 70% of the total laser current is exploited. This corresponds to a laser power of ~ 215 mW. The laser current is reduced to avoid damage to the sample. The beam splitter and optical components placed on the optical path followed by the laser radiation (see Figure 2.2) further diminish the amount of radiation hitting the sample. Eventually, the sample is hit by around 185-190 mW. Green light (with frequency $\sim 532\text{nm}$) is exploited. Scans are performed for 3-4 hours for each incidence angle.

In the following, Brillouin spectra obtained for each sample are shown in a frequency range from 0 to 30 GHz because of the symmetry properties of the spectra given by the Stokes and anti-Stokes peaks (see Chapter 2). They are shown both in their raw (i.e., in the way they have been collected experimentally) and filtered stage. Filtering is performed to reduce noise and is obtained considering a mild moving average. Furthermore, the above mentioned symmetry properties of the spectrum are exploited to evaluate the geometric mean between positive and negative frequencies. The experimental velocities estimated from each Brillouin spectrum are obtained through a best fit procedure. The latter is performed through an ad-hoc software developed at the Nanolab of Politecnico di Milano

which takes into account the asymmetry of the frequency peaks caused by the lens finite collection aperture and the presence of the mirror. In this context, the asymmetry of the frequency peaks provides a reference model to assist best fit of the experimental peaks.

Brillouin analysis for each sample is reported in the following. Upon following the least square procedure detailed in Section 3.2.1, it is possible to retrieve estimates of the values of the elastic constants associated with the samples. All of the analyses are performed at a 68% confidence level. The latter level is selected because not too many peaks can be detected for the samples and their intensity is not so high. In the following analysis, one finds that often contour lines are not closed. This constitutes a marked challenge to the identification of the values of C_{11} and C_{44} . To estimate the elastic constants, it is possible to impose physical limits to constrain the solution across the (C_{44}, C_{11}) plane. The upper and lower bounds in the (C_{44}, C_{11}) plane can be chosen upon considering thermodynamic stability conditions. Thermodynamic stability is reached when

$$C_{11} > \frac{4}{3}C_{44} > 0 \quad (3.13)$$

thus corresponding to a Poisson ratio ν which fulfills the following condition

$$-1 < \nu < \frac{1}{2} \quad (3.14)$$

Most materials are characterized by a positive Poisson's ratio (see Chapter 1). This is true also for titanium and its alloys. Equations 3.13 and 3.14 allow identifying rather large regions in the (C_{44}, C_{11}) plane. Such regions can be reduced upon introducing physical limits. The material stiffness (i.e., the extent to which a material opposes to deformation when a force is applied to it) can be distinguished between volume and shape stiffness. The latter is linked to the Poisson's ratio. For instance, a Poisson's ratio $\nu = 0.5$ (i.e., in a tensile test the lateral contraction allows keeping a constant volume) corresponds to a null shape stiffness. Moreover, a Poisson's ratio $\nu = 0$ (i.e., in a tensile test the lateral contraction is null, thus allowing for a maximum opposition to shape change) yields a maximum value of the shape stiffness. Diamond is known as the material with the highest hardness in nature. Such a material does not reach a Poisson's ratio of 0 and is instead characterized by $\nu=0.0691$ [46]. In this framework, one expects titanium not to be harder than diamond. The upper bound is set at $\nu = 0.33$, which corresponds to the maximum Poisson's ratio reported for titanium [1]. Indeed, previous studies (see e.g., [12]) predict that the fcc titanium has a higher stiffness than its hcp crystal structure. In the following, the upper bound limit is adapted considering the analyzed sample.

Ti_02 sample

The experimental Brillouin spectra and data obtained from the analysis of sample Ti_02 are depicted in Figure 3.3.

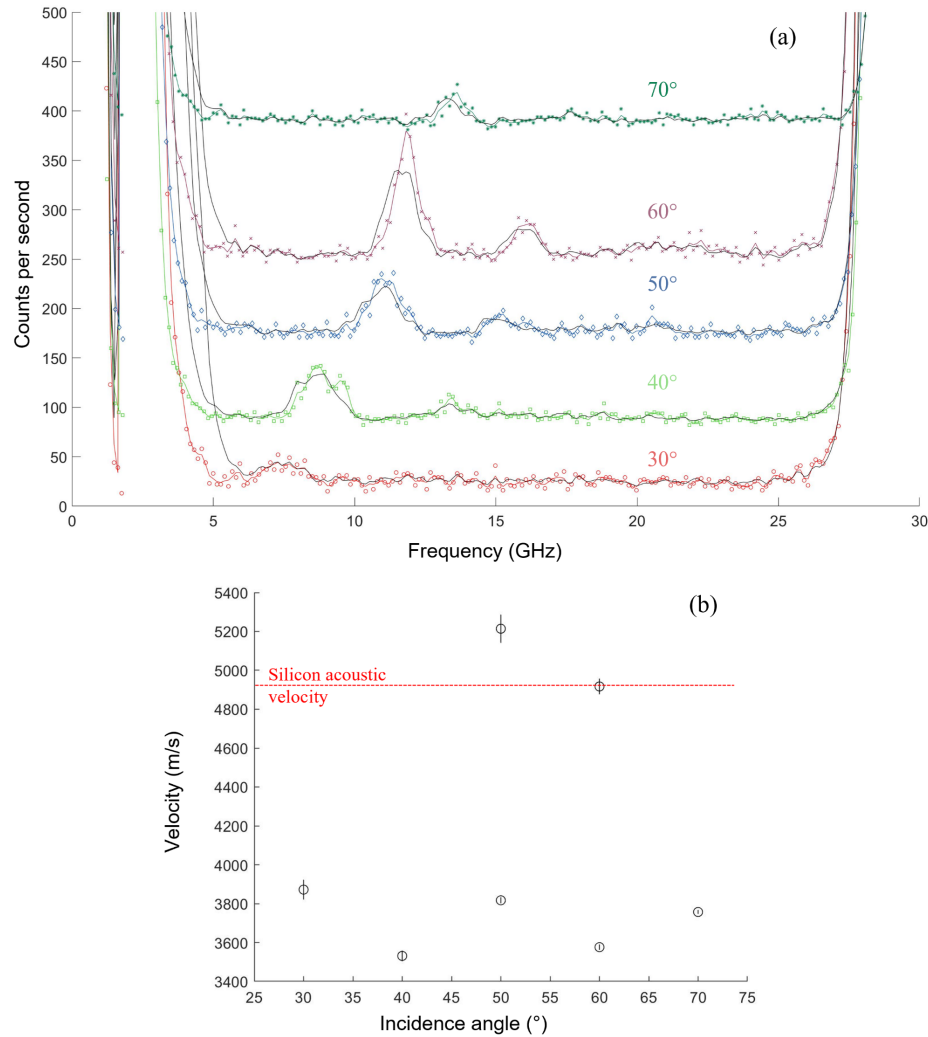


Figure 3.3: (a) Brillouin spectra experimentally retrieved from the analysis of the Ti_02 sample (incidence angles are written in the same color as the corresponding data set). Colored and black lines represent the raw (i.e., data as collected experimentally) and filtered data, respectively. Spectra obtained for different incidence angles are shifted to enhance readability. (b) Experimental velocities evaluated upon fitting data in (a) for each incidence angle. The acoustic velocity associated with the silicon substrate corresponds to the red dashed line in (b).

Brillouin spectra in Figure 3.3 (a) are shown both in their raw state (i.e., in the way they have been collected experimentally) and filtered stage. Raw and filtered data are highlighted in color and black, respectively.

From Figure 3.3 (a) it is possible to see the presence of up to two peaks, which identify two different branches of the characteristic dispersion relation of the sample. The peaks corresponding to the lowest velocities (i.e., those associated with the first branch) represent Rayleigh modes. The peaks at the highest velocities (i.e., those associated with the second branch of the dispersion relation) are Sezawa modes. Titanium is a slow film on a fast silicon substrate. This can be seen from Figure 3.3 (b). Indeed, the Rayleigh acoustic velocity (i.e., the velocity of the acoustic waves traveling on the considered medium) associated with the silicon substrate is higher than the experimental velocity associated with the points belonging to the first branch of the Ti_02 dispersion relation. The Rayleigh velocity of the acoustic waves associated with the silicon substrate is around 4900 m/s.

Upon following the least square procedure detailed in Section 3.2.1, it is possible to retrieve the values of the elastic constants associated to the Ti_02 sample. The contour lines obtained with such an analysis are depicted in Figure 3.4.

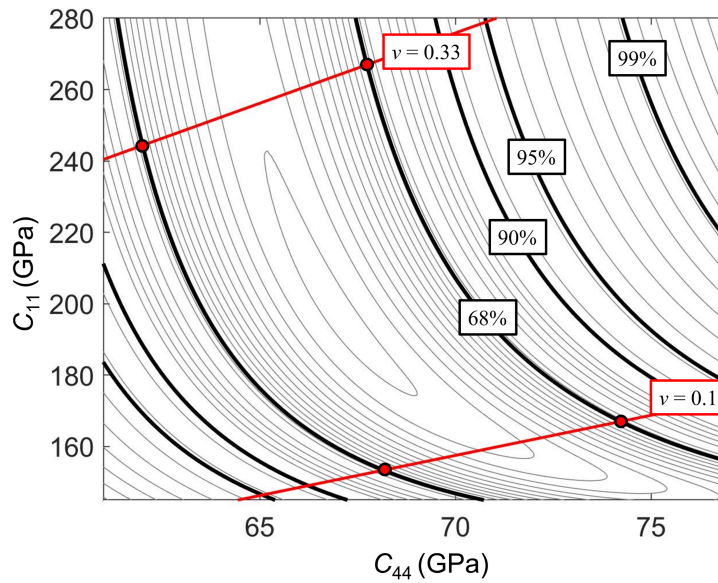


Figure 3.4: Contour lines corresponding to Equation 3.10 evaluated for sample Ti_02. The 68% confidence level considered is highlighted in black; 90%, 95%, and 99% confidence levels are also depicted in black for completeness; $\nu = 0.1$ and $\nu = 0.33$ bounds are highlighted in red. Red symbols represent the extrema of the truncated contour lines at the 68% confidence level considered for the analysis.

In Figure 3.4 it is possible to see the lines defining the lower and upper bounds determined by constant Poisson's ratio values, i.e., $\nu = 0.1$ and $\nu = 0.33$, respectively.

Upon setting the aforementioned constraints on the Poisson's ratio, one can find the rectangle that circumscribes the truncated contour lines. This procedure allows identifying

C_{11} and C_{44} as the rectangle barycenter. The error bars associated with C_{11} and C_{44} are identified as half of the rectangle sides. The results are listed in Table 3.5.

C_{11} (GPa)	C_{44} (GPa)
210 ± 57	68 ± 6

Table 3.5: Elastic constants C_{11} and C_{44} obtained from the analysis of the contour lines of sample Ti_02.

A first approach to assess the values of the elastic constant C_{12} , the bulk modulus B , and Young's modulus E is based on the use of Equations 1.12-1.13-1.17. The estimated values of C_{12} , E , and B are listed in Table 3.6, alongside their errors. The latter are evaluated through the usual error propagation formula (Equation 3.2). The Poisson's ratio resulting from theoretical evaluations (see Equation 1.15) is also listed, alongside its error resulting from Equation 3.2.

C_{12} (GPa)	ν	B (GPa)	E (GPa)
74 ± 58	0.26 ± 5.98	119 ± 57	172 ± 21

Table 3.6: Elastic constant C_{12} , Poisson's ratio ν , bulk modulus B , and Young's modulus E theoretically evaluated with Equations 1.12-1.13-1.17 for sample Ti_02. Errors are evaluated through the usual propagation error formula (Equation 3.2).

Theoretical evaluation of the values in Table 3.6 yields an overestimation of all of the listed elastic moduli (i.e., C_{12} , ν , B , and E). This can be seen especially in the estimate of ν listed in Table 3.6. The error associated with ν is notably large, since it has been calculated through the error propagation formula. A second approach to estimate the elastic moduli is thus given considering the extrema of the truncated contour lines. Indeed, it is noted that the area of the curve identified by the truncated contour lines is smaller with respect to that of the circumscribed rectangle. In particular, the value of C_{12} is assessed upon identifying the lines with constant value of C_{12} and passing through the outer extrema of the circumscribed rectangle. The very same procedure is exploited to obtain estimates of the Young's modulus E and of the bulk modulus B . Error bars are defined as half the difference between the maximum and minimum values of C_{12} , E , and B , respectively. The latter procedure is also used to identify the error bars associated with ν . The results are listed in Table 3.7. The curves with constant C_{12} , B , and E values considered are depicted in Figure 3.5.

C_{12} (GPa)	ν	B (GPa)	E (GPa)
74 ± 57	0.22 ± 0.12	120 ± 57	165 ± 15

Table 3.7: Elastic constant C_{12} , Poisson's ratio ν , bulk modulus B , and Young's modulus E evaluated considering the truncated contour lines alongside their error bars for sample Ti_02.

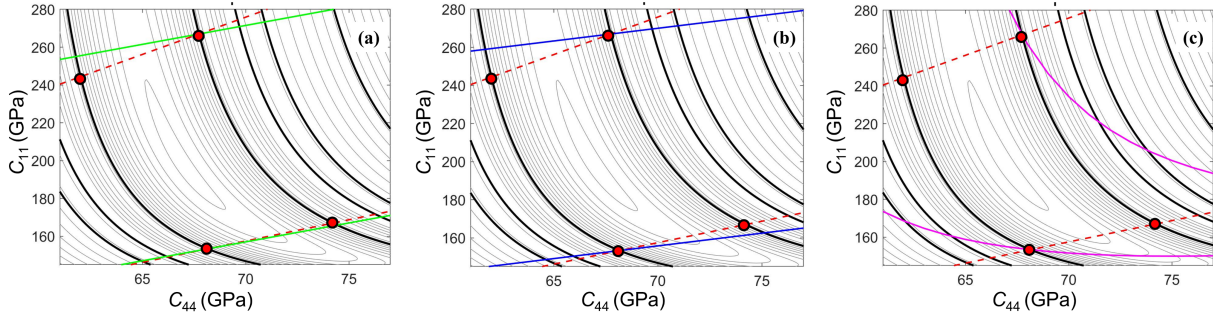


Figure 3.5: Contour lines evaluated for sample Ti_02; $\nu = 0.1$ and $\nu = 0.33$ bounds are highlighted in dashed red lines. Red dots represent the extrema of the truncated contour lines at the 68% confidence level considered for the analysis. Constant (a) C_{12} , (b) B , and (c) E curves passing through the outer extrema of the truncated contour lines are highlighted in green, blue, and magenta, respectively.

It can be noted that the values in Table 3.7 are characterized by lower uncertainties related to the considered elastic moduli. Relative variation of the value of B in Table 3.7 with respect to the estimate listed in Table 3.6 is of 0.8%. Upon comparison between estimates in Table 3.7 and Table 3.6, it can be seen that the most notable variations in the elastic moduli evaluation are documented for the values of ν and E . Indeed, the values of E and ν evaluated through the contour lines differ by 4% and 15% from those theoretically evaluated from C_{11} and C_{44} in Table 3.5. The estimates of the elastic moduli listed in Table 3.7 provide a higher quality result than those in Table 3.6 as focus is put on the contour lines and not on the circumscribed rectangle.

The values of C_{11} , C_{44} , and C_{12} obtained through the contour lines analysis can be used to compute the theoretical dispersion relations associated with the Ti_02 sample. This analysis is performed upon considering the Christoffel equation, similar to the approach adopted for the least square method exploited to identify the contour lines. The experimental data in Figure 3.3 (b) are superimposed to the theoretical dispersion relation obtained with the estimates of C_{11} , C_{44} , and C_{12} in Table 3.5. The results are shown in Figure 3.6 (a). Figure 3.6 (b) depicts theoretical dispersion relation evaluated with the

characteristic parameters (i.e., C_{11} , C_{44} , C_{12} , and mass density) of hcp titanium. Experimental data in Figure 3.3 (b) are superimposed to Figure 3.6 (b). Values of characteristic parameters (i.e., C_{11} , C_{44} , C_{12} , and mass density) of hcp titanium are listed in Table 3.8.

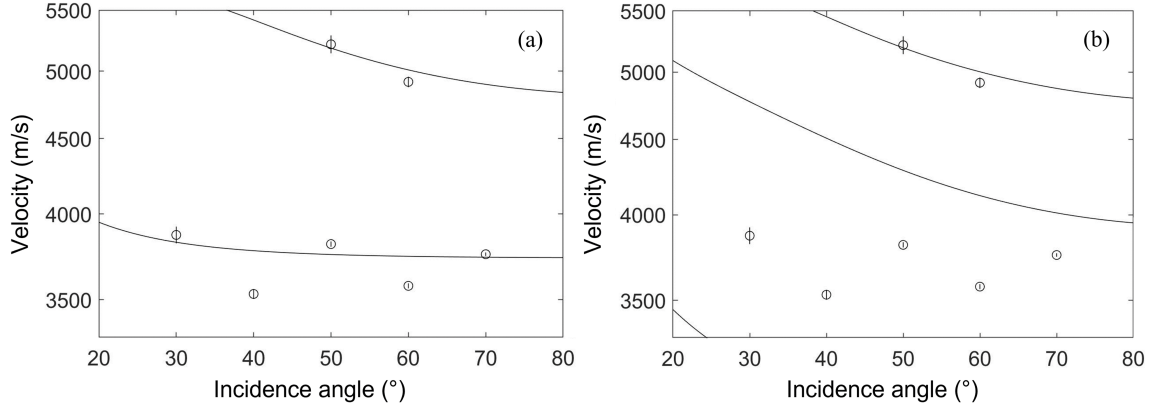


Figure 3.6: Experimental data in Figure 3.3 (b) superimposed to (a) theoretical dispersion relation obtained with the estimates of C_{11} , C_{44} and C_{12} in Table 3.5 and (b) the characteristic parameters (i.e., C_{11} , C_{44} , C_{12} , and mass density) of hcp titanium.

C_{11} (GPa)	C_{12} (GPa)	C_{44} (GPa)	ρ (kg/m ³)
168.7	80.7	44	4507

Table 3.8: Literature values for elastic constant C_{44} and mass density of hcp titanium [1, 47]. C_{11} and C_{12} are calculated from values of B and C_{44} available in the literature upon imposing the isotropy condition in Equation 1.12.

From Figure 3.6, it is possible to see that experimental data are better represented by the dispersion relations evaluated with the estimates of C_{11} , C_{44} , and C_{12} in Table 3.5. While the characteristic parameters of hcp titanium do not yield a proper interpretation of the experimental data associated with the first branch, they seem to provide a good interpretation of the data on the second branch of the dispersion relation. However, estimates in Table 3.5 are associated with improved agreement with experimental data, when considering both branches (see Figure 3.6 (a)).

Figure 3.6 clearly documents that sample Ti_02 is characterized by a behavior that differs from the one expected by an hcp titanium structure.

Ti_06 sample

The experimental Brillouin spectra and data obtained from the analysis of sample Ti_06 are depicted in Figure 3.7.

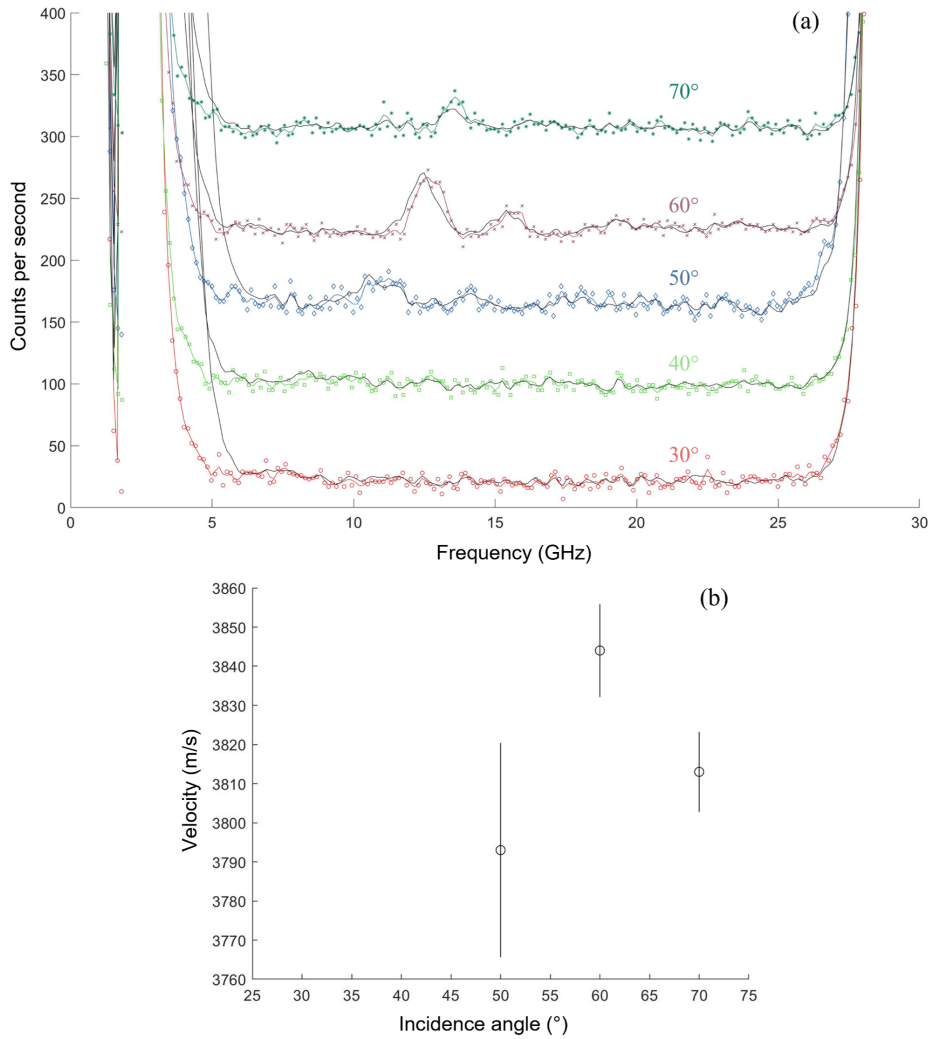


Figure 3.7: (a) Brillouin spectra experimentally retrieved from the analysis of the Ti_06 sample (incidence angles are written in the same color as the corresponding data set). Colored and black lines represent the raw (i.e., data as collected experimentally) and filtered data, respectively. Spectra obtained for different incidence angles are shifted to enhance readability. (b) Experimental velocities evaluated upon fitting data in (a) for each incidence angle.

Following the same procedure adopted for sample Ti_02, Brillouin spectra in Figure 3.7 (a) are shown in a frequency range from 0 to 30 GHz in their raw and filtered stage.

From Figure 3.7 (a) it is possible to see the presence of only one peak for all incidence

angles. Such peak corresponds to the first branch of the dispersion relation and represents Rayleigh modes. The spectra obtained at 30° and 40° are poor and do not allow the identification of any peak. A second peak can be seen at an incidence angle of 60° . However, the latter peak is not considered in the analysis. This is consistent with the observation that a single point does not allow retrieving information on the second branch of the dispersion relation. The experimental velocities in Figure 3.7 (b) are obtained through a best fit procedure, similar to the analyses illustrated above.

Upon following the least square procedure detailed in Section 3.2.1, it is possible to estimate the values of the elastic constants associated to the Ti_06 sample. The contour lines obtained with such an analysis are depicted in Figure 3.8.

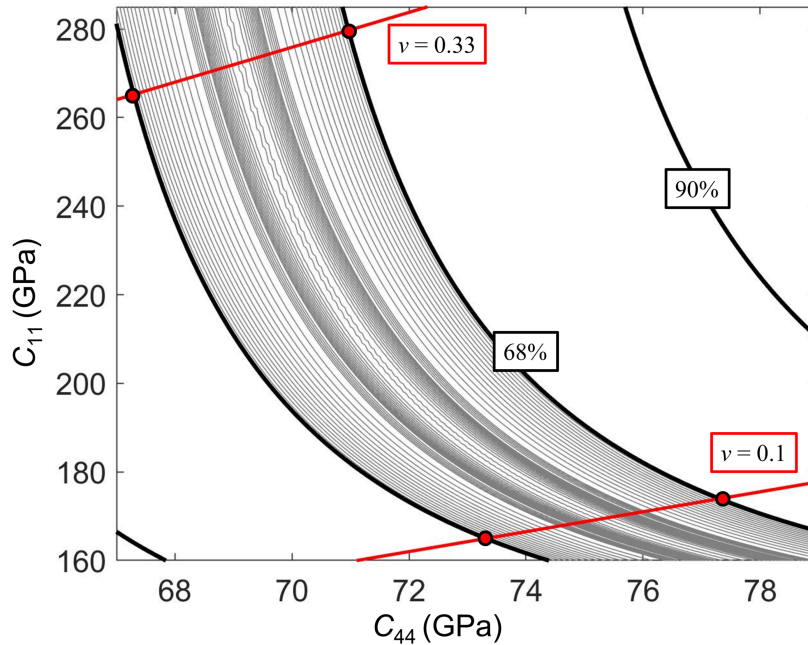


Figure 3.8: Contour lines evaluated for sample Ti_06. The 68% confidence level considered is highlighted in black. The 90% confidence level is also depicted in black for completeness. $\nu = 0.1$ and $\nu = 0.33$ bounds are highlighted in red. Red dots represent the extrema of the truncated contour lines at the 68% confidence level considered for the analysis.

From Figure 3.8, it is possible to see that the contour lines do not close, as in the case of the Ti_02 sample. Following a procedure similar to the one exploited to analyze sample Ti_02, it is possible to set upper and lower bounds in the (C_{44}, C_{11}) plane to determine the values of C_{11} and C_{44} . As for sample Ti_02, the lower bound is set to $\nu = 0.1$, whereas the the upper bound is set to $\nu = 0.33$.

Following the same procedure adopted for sample Ti_02, upon setting the aforementioned

constraints on the Poisson's ratio, one can find the rectangle that circumscribes the truncated contour lines. Values of C_{11} and C_{44} and their error bars obtained through this analysis are listed in Table 3.9.

C_{11} (GPa)	C_{44} (GPa)
222 ± 57	72 ± 5

Table 3.9: Values of elastic constants C_{11} and C_{44} obtained from the analysis of the contour lines of sample Ti_06.

The values of the elastic constant C_{12} , the bulk modulus B , and Young's modulus E are first assessed through the use of Equations 1.12-1.13-1.17. The results are listed in Table 3.10. As for sample Ti_02, a higher quality estimate of the elastic moduli is given considering the extrema of the truncated contour lines. The values of C_{12} , B , E , and ν are assessed upon identifying the curves with constant value of the elastic moduli passing through the outer extrema of the truncated contour lines. The results are listed in Table 3.10. Curves associated with constant values of C_{12} , B , and E are depicted in Figure 3.9.

C_{12}^{calc} (GPa)	ν^{calc}	B^{calc} (GPa)	E^{calc} (GPa)	C_{12}^{map} (GPa)	ν^{map}	B^{map} (GPa)	E^{map} (GPa)
78 ± 58	0.26 ± 4.92	126 ± 58	182 ± 19	78 ± 60	0.22 ± 0.12	126 ± 59	175 ± 14

Table 3.10: Elastic constant C_{12} , Poisson's ratio ν , bulk modulus B , and Young's modulus E theoretically evaluated with Equations 1.12-1.13-1.17 (labeled with the superscript "*calc*") and evaluated considering the truncated contour lines alongside their error bars (labeled with the superscript "*map*") for sample Ti_06.

From Table 3.10, it can be seen that the relative variations between the elastic moduli evaluated through the use of the contour lines and the theoretical calculation are of 15% and 4% for ν and E estimates, respectively. Values of C_{12}^{calc} and B^{calc} do not differ from C_{12}^{map} and B^{map} . The C_{12}^{map} , B^{map} , E^{map} , and ν^{map} estimates of the elastic moduli listed in Table 3.10 are considered to provide a higher quality result than C_{12}^{calc} , B^{calc} , E^{calc} , and ν^{calc} as focus is put on the contour lines and not on the circumscribed rectangle.

Similar to sample Ti_02, the values of C_{11} , C_{44} and C_{12}^{map} obtained through the contour lines analysis can be used to compute the theoretical dispersion relation associated with the Ti_06 sample. The experimental data in Figure 3.7 (b) are superimposed to the theoretical dispersion relation obtained with the estimates of C_{11} , C_{44} , and C_{12}^{map} in Table

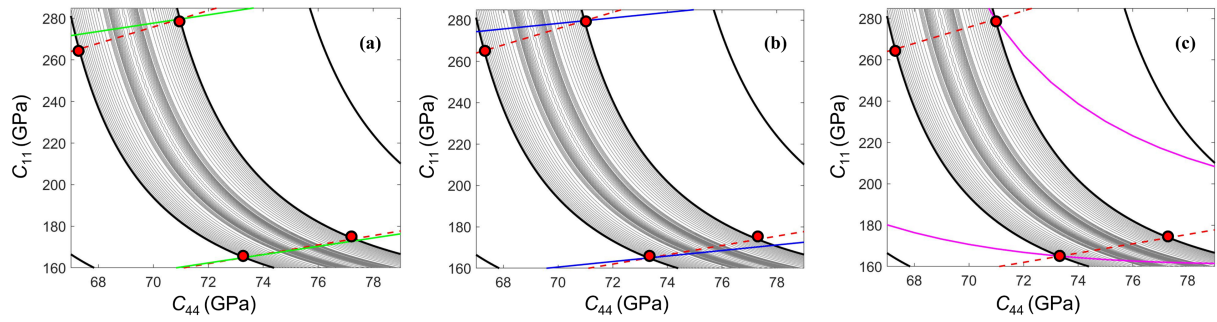


Figure 3.9: Contour lines evaluated for sample Ti_06; $\nu = 0.1$ and $\nu = 0.33$ bounds are highlighted in dashed red lines. Red dots represent the extrema of the truncated contour lines at the 68% confidence level considered for the analysis. Constant (a) C_{12} , (b) B , and (c) E curves through the outer extrema of the truncated contour lines are highlighted in green, blue, and, magenta, respectively.

3.9-3.10. The results are shown in Figure 3.10 (a). Figure 3.10 (b) depicts theoretical dispersion relation evaluated with the characteristic parameters (i.e., C_{11} , C_{44} , C_{12} , and mass density) of hcp titanium. Experimental data in Figure 3.7 (b) are superimposed to Figure 3.10 (b) as well.

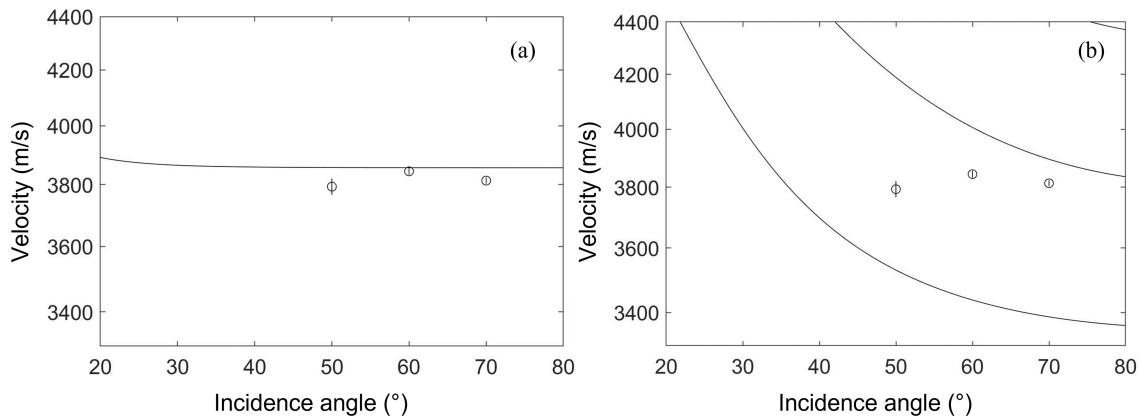


Figure 3.10: Experimental data in Figure 3.7 (b) superimposed to (a) theoretical dispersion relations obtained with the estimates of C_{11} , C_{44} , and C_{12}^{map} in Table 3.9-3.10 and (b) the characteristic parameters (i.e., C_{11} , C_{44} , C_{12} , and mass density) of hcp titanium.

Figure 3.10 reveals that experimental data are better represented by the dispersion relation evaluated with the estimates of C_{11} , C_{44} , and C_{12}^{map} in Table 3.10. The characteristic parameters of hcp titanium do not model correctly the experimental data.

From Figure 3.10, it is clear that sample Ti_06 shows a behaviour different from that expected by an hcp titanium structure.

Ti_15 sample

The experimental Brillouin spectra and data obtained from the analysis of sample Ti_15 are depicted in Figure 3.11.

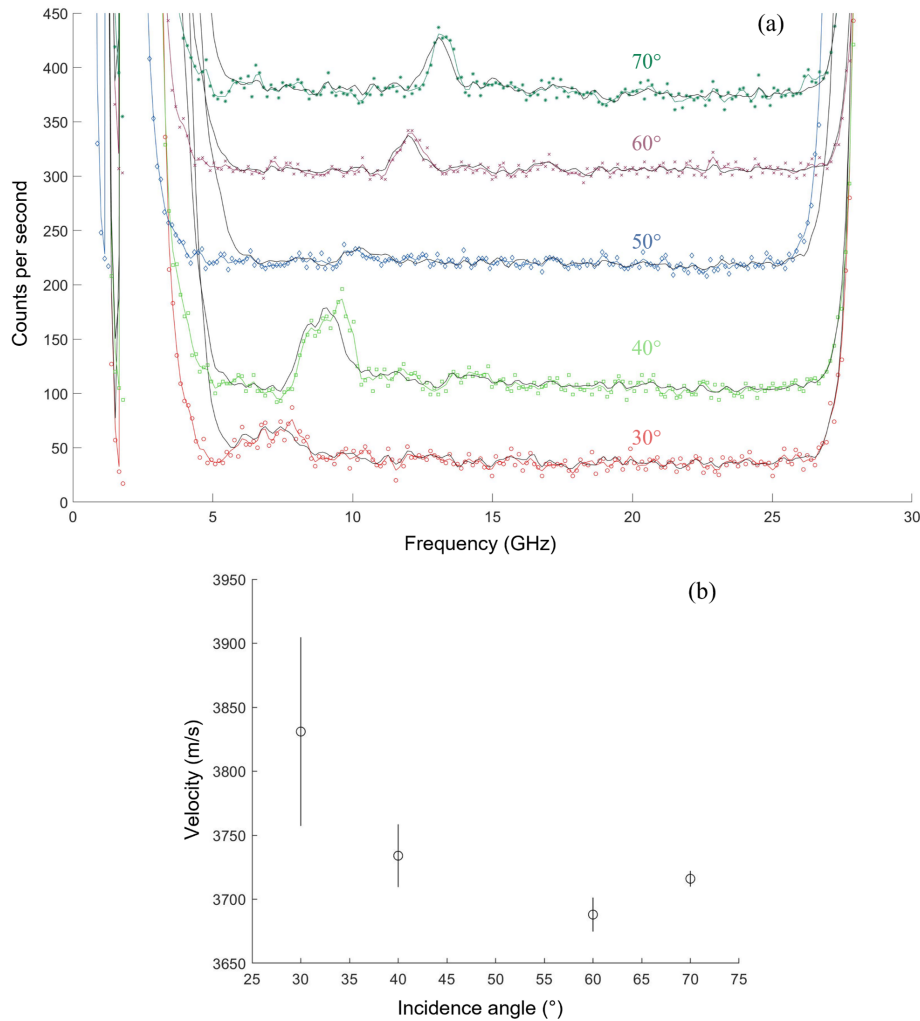


Figure 3.11: (a) Brillouin spectra experimentally retrieved from the analysis of the Ti_15 sample (incidence angles are written in the same color as the corresponding data set). Colored and black lines represent the raw (i.e., data as collected experimentally) and filtered data, respectively. Spectra obtained for different incidence angles are shifted to enhance readability. (b) Experimental velocities evaluated upon fitting data in (a) for each incidence angle.

From Figure 3.11 (a), for all incidence angles it is possible to see the presence of only one peak, which corresponds to the first branch of the dispersion relation and represents Rayleigh modes. Moreover, no peaks are detected at 50°. The experimental velocities in Figure 3.11 (b) are obtained through a best fit procedure.

The least square procedure detailed in Section 3.2.1 allows retrieving the contour lines associated with sample Ti_15 (see Figure 3.12).

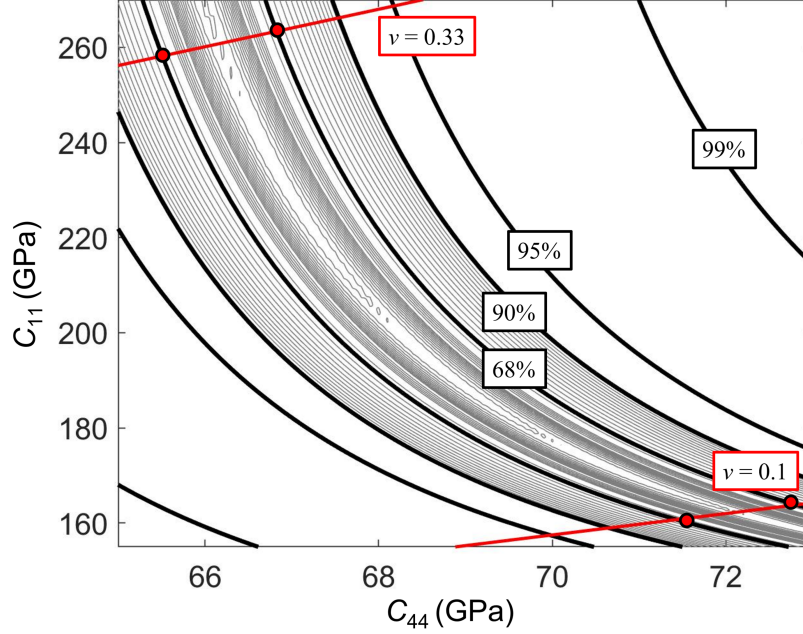


Figure 3.12: Contour lines evaluated for sample Ti_15. The 68% confidence level considered is highlighted in black. The 90%, 95%, and 99% confidence levels are also depicted in black for completeness; $\nu = 0.1$ and $\nu = 0.33$ bounds are highlighted in red. Red dots represent the extrema of the truncated contour lines at the 68% confidence level considered for the analysis.

From Figure 3.12, it is possible to see that the contour lines do not close, as in the case of the previous samples. As previously done, the lower and upper bounds in the (C_{44}, C_{11}) plane are set to $\nu = 0.1$ and $\nu = 0.33$, respectively.

The procedure adopted for the previous samples is exploited to analyze the Ti_15 sample. The values of C_{11} and C_{44} retrieved from the analysis of Figure 3.12 are listed in Table 3.11. The estimates of C_{12}^{calc} , E^{calc} , B^{calc} , ν^{calc} , C_{12}^{map} , E^{map} , B^{map} , and ν^{map} are listed in Table 3.12 alongside their error bars. Curves associated with constant values of C_{12} , B , and E are depicted in Figure 3.13.

From Table 3.12, it can be seen that the relative variations between the elastic moduli evaluated through the use of the contour lines and the theoretical calculation are of 15% and 4% for ν and E estimates, respectively. C_{12}^{calc} and B^{calc} values do not differ from C_{12}^{map} and B^{map} . As previously done, the C_{12}^{map} , B^{map} , E^{map} and ν^{map} estimates of the elastic moduli listed in Table 3.12 are considered to provide a higher quality result C_{12}^{calc} , B^{calc} , E^{calc} , and ν^{calc} .

C_{11} (GPa)	C_{44} (GPa)
212 ± 51	69 ± 4

Table 3.11: Elastic constants C_{11} and C_{44} obtained from the analysis of the contour lines of sample Ti_15.

C_{12}^{calc} (GPa)	ν^{calc}	B^{calc} (GPa)	E^{calc} (GPa)	C_{12}^{map} (GPa)	ν^{map}	B^{map} (GPa)	E^{map} (GPa)
74 ± 52	0.26 ± 3.59	120 ± 52	174 ± 15	74 ± 56	0.22 ± 0.12	120 ± 54	167 ± 10

Table 3.12: Elastic constant C_{12} , Poisson's ratio ν , bulk modulus B , and Young's modulus E theoretically evaluated with Equations 1.121-1.15-1.17-1.13 (labeled with the superscript "calc") and evaluated considering the truncated contour lines alongside their error bars (labeled with the superscript "map") for sample Ti_15.

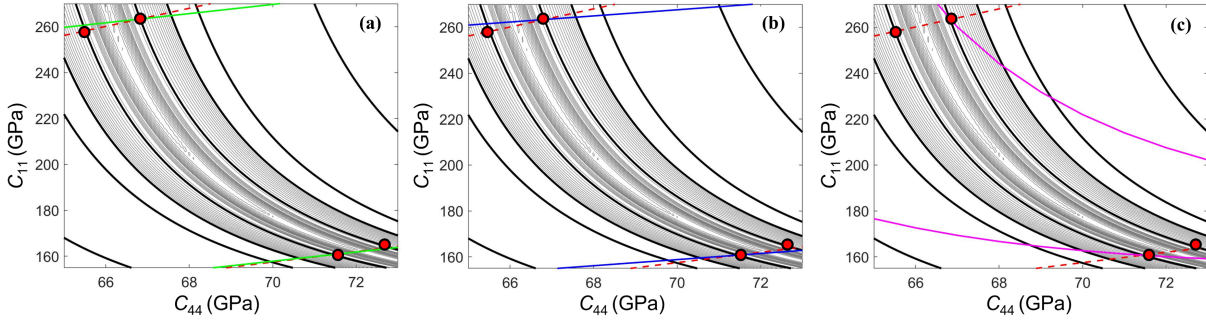


Figure 3.13: Contour lines evaluated for sample Ti_15. $\nu = 0.1$ and $\nu = 0.33$ bounds are highlighted in dashed red lines. Red dots represent the extrema of the truncated contour lines at the 68% confidence level considered for the analysis. Constant (a) C_{12} , (b) B , and (c) E curves passing through the outer extrema of the truncated contour lines are highlighted in green, blue, and, magenta, respectively.

The values of C_{11} , C_{44} , and C_{12}^{map} obtained through the contour lines analysis can be used to compute the theoretical dispersion relation associated with the Ti_15 sample. The results are shown in Figure 3.14.

From Figure 3.14, it is possible to see that experimental data are better represented by the dispersion relation evaluated with the estimates of C_{11} , C_{44} and C_{12}^{map} in Table 3.11 and 3.10. The characteristic parameters of hcp titanium are not conducive to a proper representation of the experimental data.

From Figure 3.14, it is clear that sample Ti_15 shows a behaviour different from that expected by an hcp titanium structure.

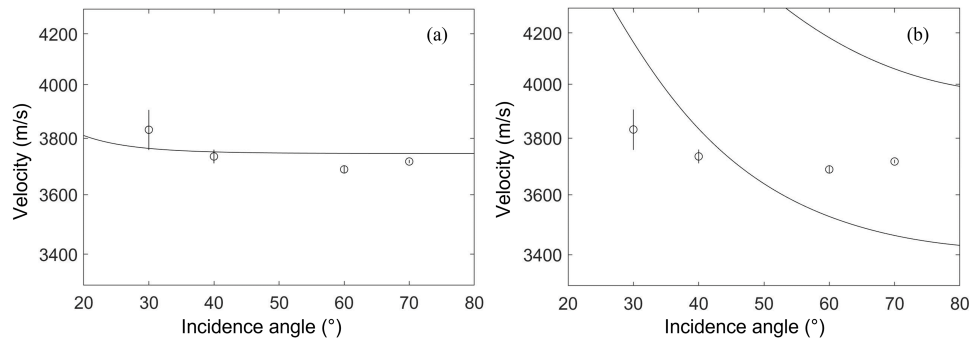


Figure 3.14: Experimental data in Figure 3.11 (b) superimposed to (a) theoretical dispersion relations obtained with the estimates of C_{11} , C_{44} , and C_{12}^{map} in Table 3.11 and 3.12 and (b) the characteristic parameters (i.e., C_{11} , C_{44} , C_{12} , and mass density) of hcp titanium.

A close inspection of Figure 3.12 reveals that the inner contour lines (i.e., those closer to the minimum LS_{min}) show multiple minima (i.e., multiple closed contour lines) for high values of C_{11} . Thus, the map in Figure 3.12 is extended to include higher values of C_{11} . The result is depicted in Figure 3.15.

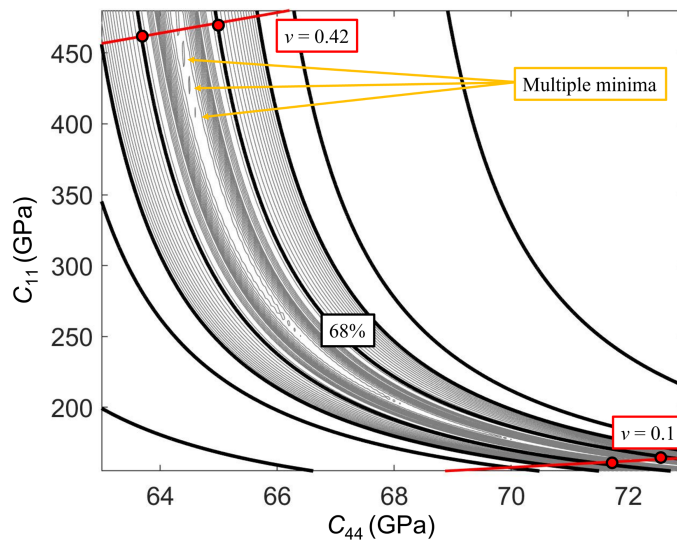


Figure 3.15: Contour lines evaluated for sample Ti_15 obtained upon enlarging the field of view of Figure 3.12. The 68% confidence level considered is highlighted in black; $\nu = 0.1$ and $\nu = 0.42$ bounds are highlighted in red. Red dots represent the extrema of the truncated contour lines at the 68% confidence level considered for the analysis.

Figure 3.15 reveals that the contour lines do not close even in this case. Thus, a higher upper limit (i.e., $\nu = 0.42$) is considered. Indeed, the latter value is the characteristic Poisson's ratio associated with gold, which is known for its softness. In this analysis, it is

assumed that the samples cannot exceed the value of the Poisson's ratio for gold, because titanium is known for its high strength.

The values of C_{11} and C_{44} obtained from the analysis of Figure 3.15 are listed in Table 3.13. The estimates of C_{12}^{calc} , E^{calc} , B^{calc} , ν^{calc} , C_{12}^{map} , E^{map} , B^{map} , and ν^{map} are listed in Table 3.14 alongside their error bars. Constant C_{12} , B , and E curves considered are depicted in Figure 3.16.

C_{11} (GPa)	C_{44} (GPa)
316 ± 155	68 ± 5

Table 3.13: Elastic constants C_{11} and C_{44} obtained from the analysis of the contour lines of sample Ti_15 in Figure 3.15.

C_{12}^{calc} (GPa)	ν^{calc}	B^{calc} (GPa)	E^{calc} (GPa)	C_{12}^{map} (GPa)	ν^{map}	B^{map} (GPa)	E^{map} (GPa)
179 ± 155	0.36 ± 3.54	225 ± 155	186 ± 14	179 ± 162	0.26 ± 0.16	225 ± 159	171 ± 14

Table 3.14: Elastic constant C_{12} , Poisson's ratio ν , bulk modulus B , and Young's modulus E theoretically evaluated with Equations 1.121-1.15-1.17-1.13 (labeled with the superscript "calc") and evaluated considering the truncated contour lines alongside their error bars (labeled with the superscript "map") in Figure 3.15.

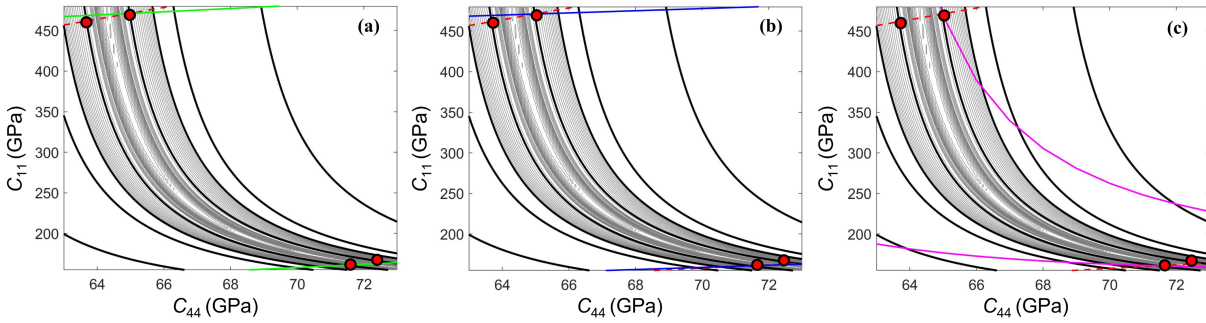


Figure 3.16: Contour lines evaluated for sample Ti_15; $\nu = 0.1$ and $\nu = 0.42$ bounds are highlighted in dashed red lines. Red dots represent the extrema of the truncated contour lines at 68% confidence level considered for the analysis. Constant (a) C_{12} , (b) B , and (c) E curves passing through the outer extrema of the truncated contour lines are highlighted in green, blue, and magenta, respectively.

From Table 3.14, it can be seen that the relative variations between the elastic moduli evaluated through the use of the contour lines and the theoretical calculation are of 28%

and 8% for ν and E estimates, respectively. C_{12}^{calc} and B^{calc} values do not differ from C_{12}^{map} and B^{map} . Similar to what has been observed before, the C_{12}^{map} , B^{map} , E^{map} and ν^{map} estimates of the elastic moduli listed in Table 3.14 are considered to provide a higher quality result than C_{12}^{calc} , B^{calc} , E^{calc} and ν^{calc} .

The values of C_{11} , C_{44} , and C_{12}^{map} obtained in Table 3.13 and 3.14 are used to compute the theoretical dispersion relation associated with the Ti_15 sample. The results are shown in Figure 3.17.

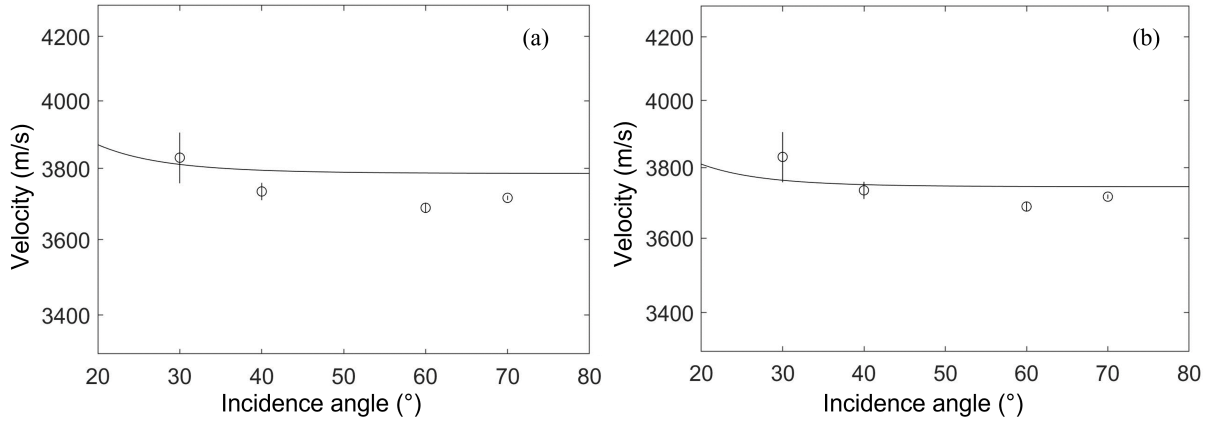


Figure 3.17: Experimental data in Figure 3.11 (b) superimposed to (a) theoretical dispersion relation obtained with the estimates of C_{11} , C_{44} , and C_{12}^{map} in Table 3.13 and 3.14 and (b) theoretical dispersion relation obtained with the estimates of C_{11} , C_{44} , and C_{12}^{map} in Table 3.11 and 3.12.

From Figure 3.17, it is possible to see that experimental data are better represented by the dispersion relation evaluated with the estimates of C_{11} , C_{44} and C_{12}^{map} in Table 3.11 and 3.12. The latter values are those considered as the best estimates of the elastic moduli characterizing sample Ti_15.

Ti_16 sample

The experimental Brillouin spectra and data obtained from the analysis of sample Ti_16 are depicted in Figure 3.18.

Figure 3.18 (a) documents the presence of only one peak for all incidence angles. Such a peak corresponds to the first branch of the dispersion relation and represents Rayleigh modes. Moreover, peaks on the second branch are detected at incidence angles of 60° and 70°. These peaks correspond to Sezawa modes. The experimental velocities in Figure 3.18 (b) are obtained through a best fit procedure.

The least square procedure detailed in Section 3.2.1 yields the contour lines associated

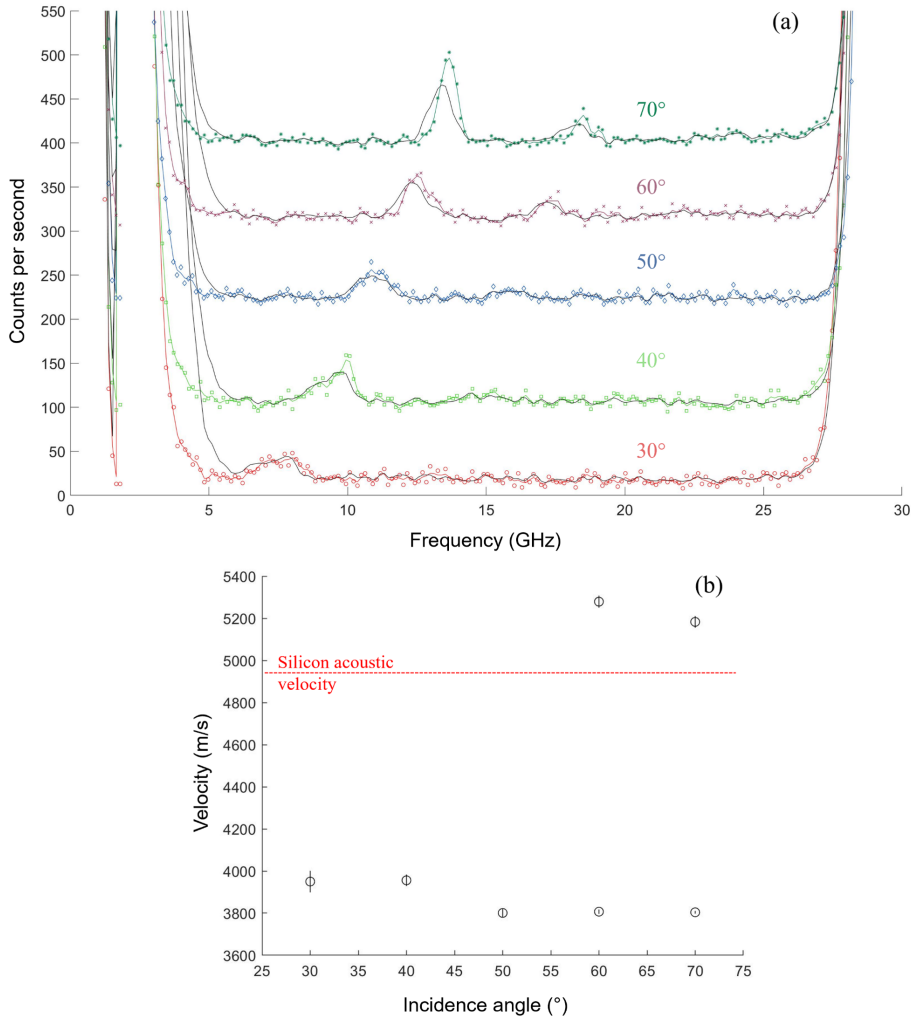


Figure 3.18: (a) Brillouin spectra experimentally retrieved from the analysis of the Ti_16 sample (incidence angles are written in the same color as the corresponding data set). Colored and black lines represent the raw (i.e., data as collected experimentally) and filtered data, respectively. Spectra obtained for different incidence angles are shifted to enhance readability. (b) Experimental velocities evaluated upon fitting data in (a) for each incidence angle.

with sample Ti_16 (see Figure 3.19).

Contour lines in Figure 3.19 are closed. For the analysis of this sample, the $\nu = 0.1$ and $\nu = 0.33$ bounds are not considered. Indeed, from Figure 3.19 (a) it is possible to see that the contour lines corresponding to the 68% confidence level close at higher C_{11} values than those identified by the $\nu = 0.1$ constant line. Moreover, an upper bound of $\nu = 0.42$ (corresponding to the Poisson's ratio of gold [48]) is selected to analyze Figure 3.19 (b). Indeed, from Figure 3.19 (a) it can be noted that the $\nu = 0.33$ constant line cuts off a

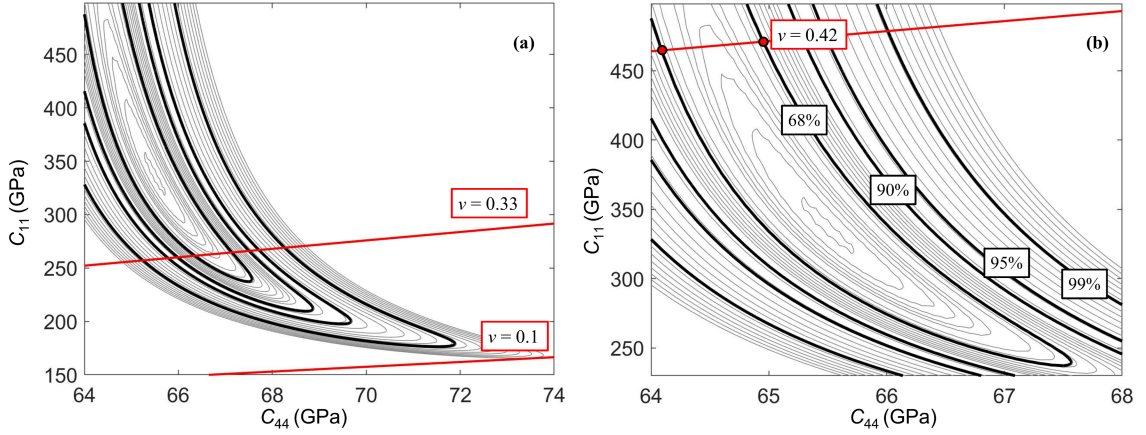


Figure 3.19: Contour lines evaluated for sample Ti_16. The 68% confidence level considered is highlighted in black. The 90%, 95%, and 99% confidence levels are also depicted in black for completeness; $\nu = 0.1$ and $\nu = 0.33$ bounds are highlighted in red in (a); the $\nu = 0.42$ bound is highlighted in red in (b). Red dots represent the extrema of the truncated contour lines at the 68% confidence level considered for the analysis.

large part of the (C_{44}, C_{11}) plane.

The procedure adopted for the previous samples is exploited to analyze the Ti_16 sample. The values of C_{11} and C_{44} retrieved from the analysis of Figure 3.19 (b) are listed in Table 3.15.

C_{11} (GPa)	C_{44} (GPa)
354 ± 117	66 ± 2

Table 3.15: Elastic constants C_{11} and C_{44} obtained from the analysis of the contour lines of sample Ti_16.

The estimates of C_{12}^{calc} , E^{calc} , B^{calc} , ν^{calc} , C_{12}^{map} , E^{map} , B^{map} , and ν^{map} are listed in Table 3.16 alongside their error bars. Curves characterized by constant values of C_{12} , ν , B , and E are depicted in Figure 3.20.

From Table 3.16, it can be seen that the relative variations between the elastic moduli evaluated through the use of the contour lines and the theoretical calculation are of 1% and 8% for E and ν estimates, respectively. Values of C_{12}^{calc} , and B^{calc} values do not differ from C_{12}^{map} and B^{map} . As previously done, the C_{12}^{map} , B^{map} , E^{map} and ν^{map} estimates of the elastic moduli listed in Table 3.16 are considered to provide a higher quality result than C_{12}^{calc} , B^{calc} , E^{calc} and ν^{calc} .

C_{12}^{calc} (GPa)	ν^{calc}	B^{calc} (GPa)	E^{calc} (GPa)	C_{12}^{map} (GPa)	ν^{map}	B^{map} (GPa)	E^{map} (GPa)
222 ± 117	0.39 ± 1.25	266 ± 117	182 ± 6	222 ± 119	0.36 ± 0.06	266 ± 118	180 ± 4

Table 3.16: Elastic constant C_{12} , Poisson's ratio ν , bulk modulus B , and Young's modulus E theoretically evaluated with Equations 1.121-1.15-1.17-1.13 (labeled with the superscript "calc") and evaluated considering the truncated contour lines alongside their error bars (labeled with the superscript "map") for sample Ti_16.

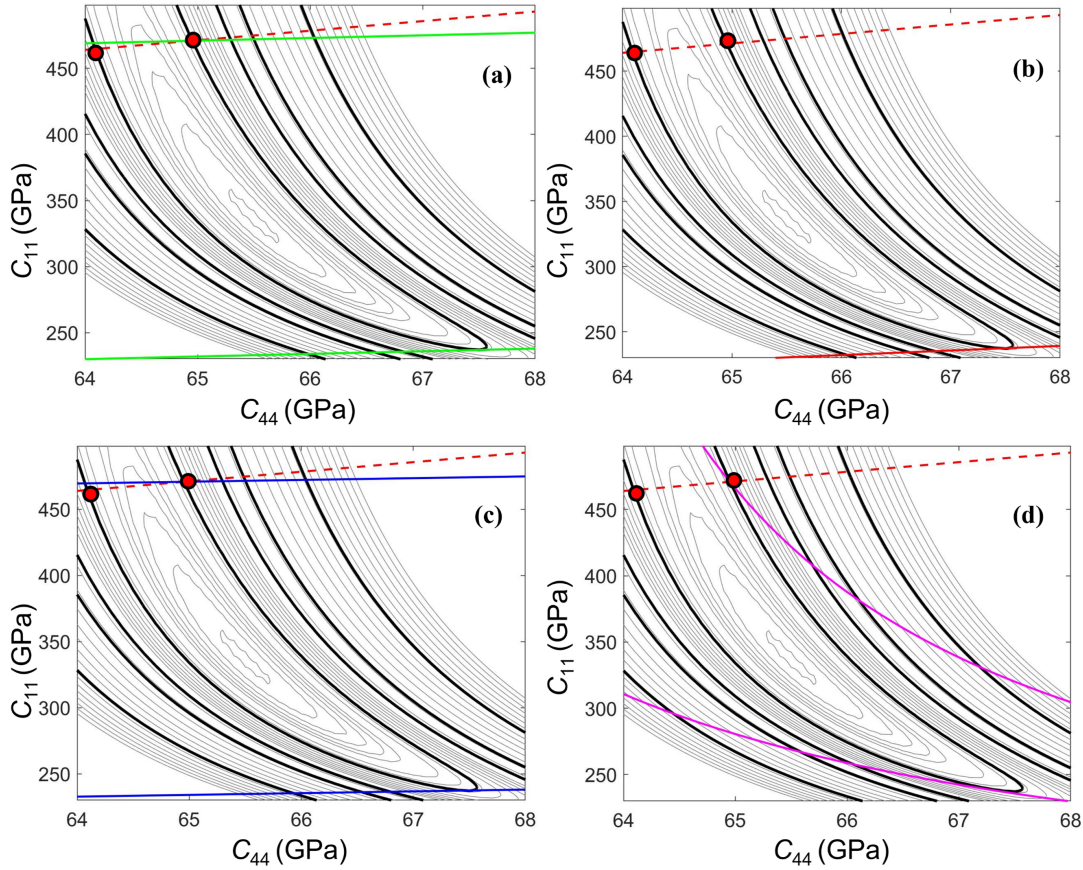


Figure 3.20: Contour lines evaluated for sample Ti_16; the $\nu = 0.42$ bound is highlighted in dashed red lines. Red dots represent the extrema of the truncated contour lines at the 68% confidence level considered for the analysis. Constant (a) C_{12} , (b) ν , (b) B , and (d) E curves passing through the outer extrema of the truncated contour lines are highlighted in green, red, blue, and magenta, respectively.

The values of C_{11} , C_{44} , and C_{12}^{map} obtained through the contour lines analysis can be used to compute the theoretical dispersion relation associated with the Ti_16 sample. The results are shown in Figure 3.21.

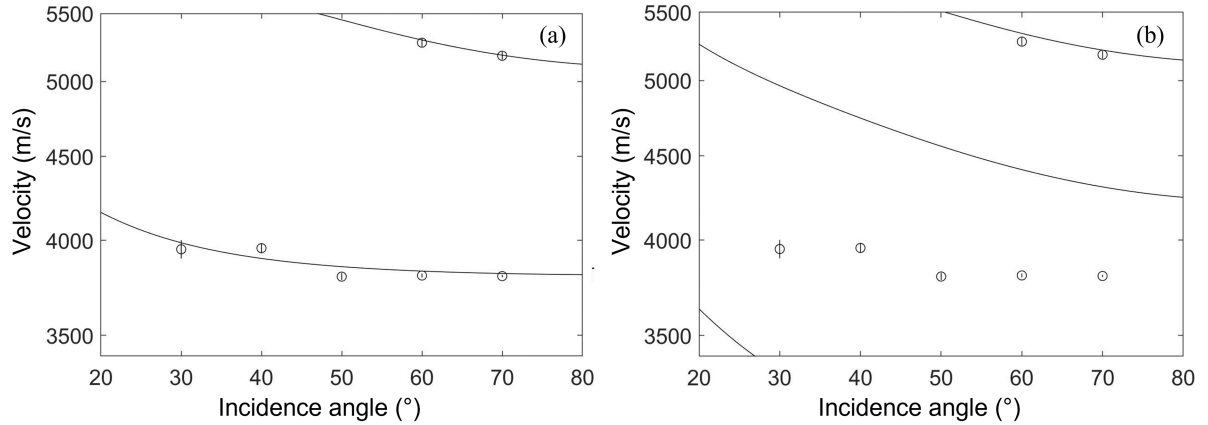


Figure 3.21: Experimental data in Figure 3.18 (b) superimposed to (a) theoretical dispersion relation obtained with the estimates of C_{11} , C_{44} , and C_{12}^{map} in Table 3.15 and 3.16 and (b) the characteristic parameters (i.e., C_{11} , C_{44} , C_{12} , and mass density) of hcp titanium.

From Figure 3.21, it is possible to see that experimental data are better represented by the dispersion relation evaluated with the estimates of C_{11} , C_{44} , and C_{12}^{map} in Table 3.15 and 3.16. From Figure 3.21, it is clear that sample Ti_16 shows a behaviour different from that expected by an hcp titanium structure.

Ti_24 sample

The experimental Brillouin spectra and data obtained from the analysis of sample Ti_24 are depicted in Figure 3.22.

Figure 3.22 (a) documents the presence of only one peak for all incidence angles. Such peak corresponds to the first branch of the dispersion relation and represents Rayleigh modes. The experimental velocities in Figure 3.22 (b) are obtained through a best fit procedure.

Figure 3.22 (b) reveals a trend of the velocities which differs from the one detected for other samples. Indeed, a slow film on a fast substrate (e.g., titanium films on silicon substrate) is characterized by an increase of velocities towards smaller angles (e.g., Figure 3.3, 3.18). However, Figure 3.22 (b) shows velocities decreasing at smaller angles. The latter behavior is typical of a fast film on a slow substrate [34]. This somehow unexpected behavior associated with sample Ti_24 suggests that one of the hypothesis exploited to perform Brillouin analysis (i.e., homogeneous, perfectly adherent film) does not hold. Brillouin analysis is performed to verify whether sample Ti_24 satisfies the latter hypothesis.

The contour lines obtained for sample Ti_24 are depicted in Figure 3.23.

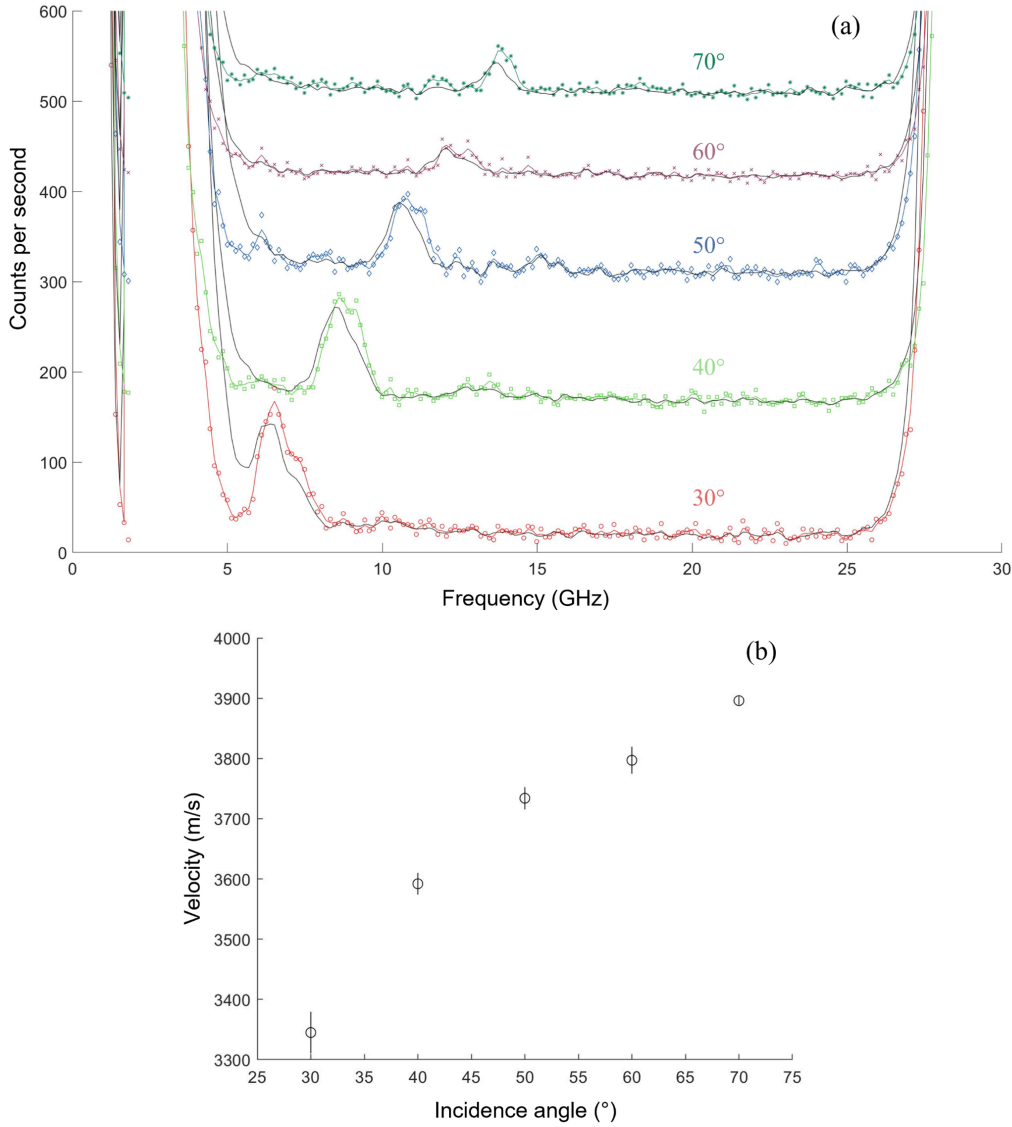


Figure 3.22: (a) Brillouin spectra experimentally retrieved from the analysis of the Ti_24 sample (incidence angles are written in the same color as the corresponding data set). Colored and black lines represent the raw (i.e., data as collected experimentally) and filtered data. Spectra obtained for different incidence angles are shifted to enhance readability. (b) Experimental velocities evaluated upon fitting data in (a) for each incidence angle.

Values of C_{11} , C_{44} , and their corresponding error bars obtained through this analysis are listed in Table 3.17.

The procedure adopted for the previous samples is exploited to analyze the Ti_24 sample. The estimates of C_{12}^{calc} , E^{calc} , B^{calc} , ν^{calc} , C_{12}^{map} , E^{map} , B^{map} , and ν^{map} are listed in Table 3.18 alongside their error bars. Constant C_{12} , ν , B , and E curves considered are depicted in Figure 3.24.

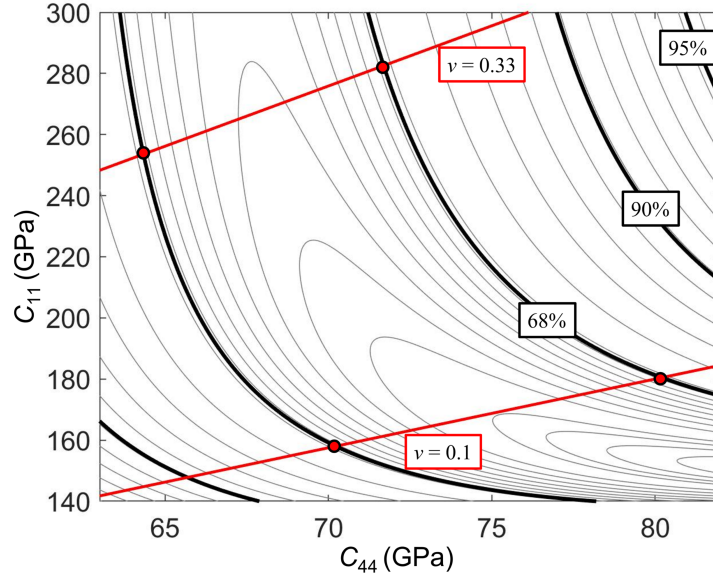


Figure 3.23: Contour lines evaluated for sample Ti_24. The 68% confidence level considered is highlighted in black. The 90% and 95% confidence levels are also depicted in black for completeness; the $\nu = 0.1$ and $\nu = 0.33$ bounds are highlighted in red. Red dots represent the extrema of the truncated contour lines at the 68% confidence level considered for the analysis.

C_{11} (GPa)	C_{44} (GPa)
220 ± 62	72 ± 8

Table 3.17: Elastic constants C_{11} and C_{44} obtained from the analysis of the contour lines of sample Ti_24.

C_{12}^{calc} (GPa)	ν^{calc}	B^{calc} (GPa)	E^{calc} (GPa)	C_{12}^{map} (GPa)	ν^{map}	B^{map} (GPa)	E^{map} (GPa)
76 ± 64	0.26 ± 7.84	124 ± 63	182 ± 26	78 ± 61	0.22 ± 0.12	126 ± 61	173 ± 18

Table 3.18: Elastic constant C_{12} , Poisson's ratio ν , bulk modulus B , and Young's modulus E theoretically evaluated with Equations 1.121-1.15-1.17-1.13 (labeled with the superscript "calc") and evaluated considering the truncated contour lines alongside their error bars (labeled with the superscript "map") for sample Ti_24.

From Table 3.18, it can be seen that the relative variations between the elastic moduli evaluated through the use of the contour lines and the theoretical calculation are of 15% and 5% for ν and E estimates, respectively. C_{12}^{calc} and B^{calc} values differ of 3% and 2% from

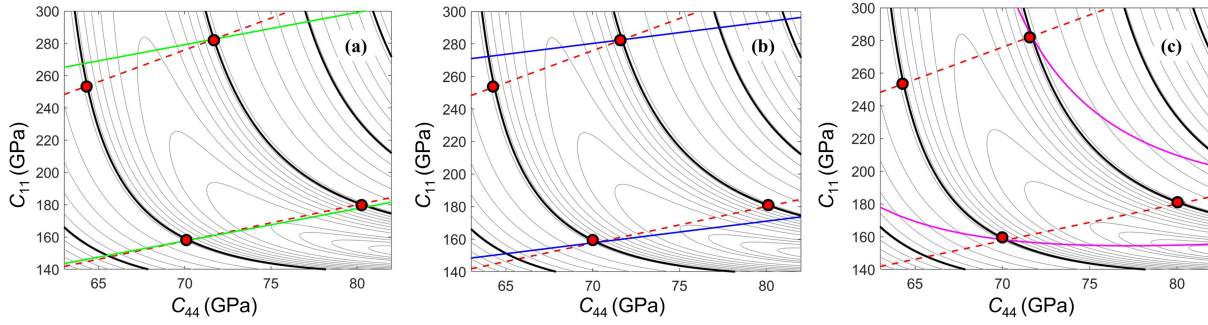


Figure 3.24: Contour lines evaluated for sample Ti_24; the $\nu = 0.1$ and $\nu = 0.33$ bounds are highlighted in dashed red lines. Red dots represent the extrema of the truncated contour lines at the 68% confidence level considered for the analysis. Constant (a) C_{12} , (b) B , and (c) E curves passing through the outer extrema of the truncated contour lines are highlighted in green, blue, and magenta, respectively.

C_{12}^{map} and B^{map} , respectively. The C_{12}^{map} , B^{map} , E^{map} and ν^{map} estimates of the elastic moduli listed in Table 3.18 are considered to provide a higher quality result than C_{12}^{calc} , B^{calc} , E^{calc} and ν^{calc} as focus is put on the contour lines and not on the circumscribed rectangle.

Similar to what has been presented for sample Ti_24, the values of C_{11} , C_{44} , and C_{12}^{map} obtained through the contour lines analysis can be used to compute the theoretical dispersion relation associated with the Ti_24 sample. The corresponding results are also shown in Figure 3.25.

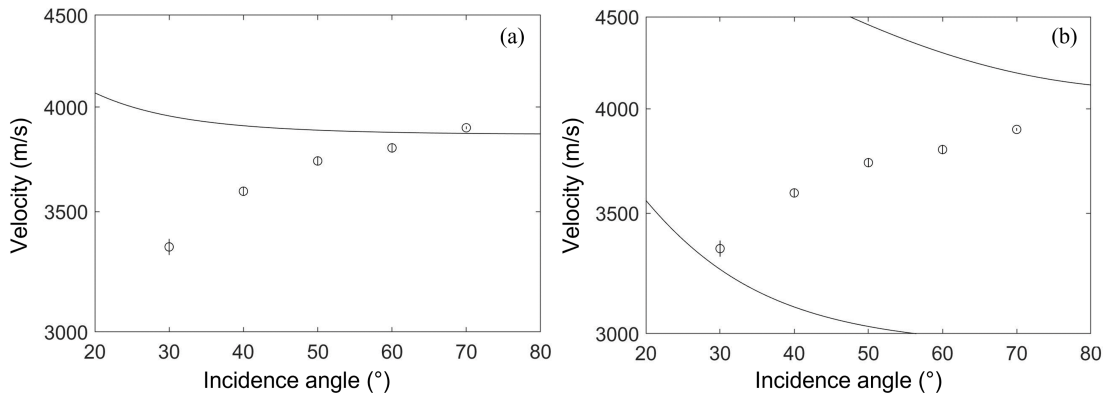


Figure 3.25: Experimental data in Figure 3.22 (b) superimposed to (a) theoretical dispersion relation obtained with the estimates of C_{11} , C_{44} , and C_{12}^{map} in Table 3.17 and 3.18 and (b) the characteristic parameters (i.e., C_{11} , C_{44} , C_{12} , and mass density) of hcp titanium.

From Figure 3.25, it is possible to see that experimental data are not correctly represented by the dispersion relation evaluated with the estimates of C_{11} , C_{44} , and C_{12}^{map} in Table

3.17 and 3.18. The evaluation of the theoretical dispersion relation supports the idea that sample Ti_24 does not fulfill the hypothesis at the basis of Brillouin analysis. However, the dispersion relation evaluated with the estimates of C_{11} , C_{44} , and C_{12}^{map} in Table 3.18 is still capable of providing an interpretation of the experimental data which is of higher quality than what can be obtained through the characteristic parameters of hcp titanium. Upon inspecting more closely Figure 3.23, it is possible to note that the contour lines seem to be extending towards higher C_{44} values. Extended contour lines for sample Ti_24 are depicted in Figure 3.26.

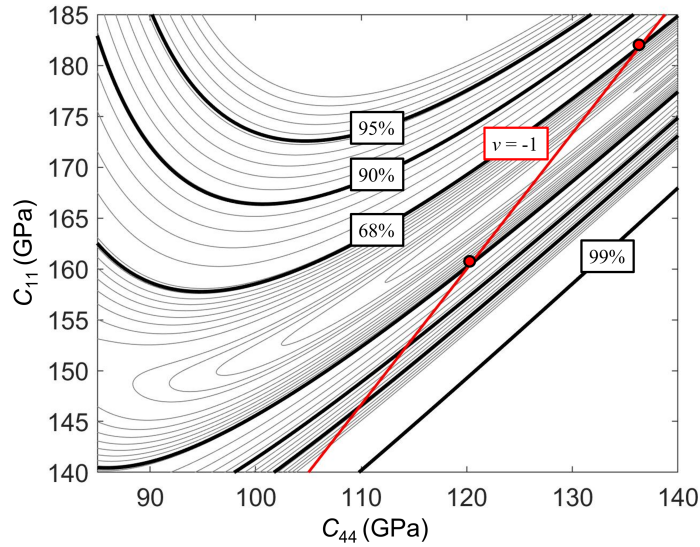


Figure 3.26: Contour lines for sample Ti_24 associated with an enlarged range of C_{44} values. The 68%, 90%, 95%, and 99% confidence levels are shown as well as the red dots showing the truncated contour lines at the 68% confidence level. The $\nu = -1$ constant line is highlighted in red.

The constant line at $\nu = -1$ is highlighted in Figure 3.26. The contour lines in Figure 3.26 seem to extend towards even higher C_{44} values. However, values of the Poisson's ratio range in between -1 and 0.5 (see Equation 1.15). If we consider the $\nu = -1$ and $\nu = 0.33$ as lower and upper boundary for sample Ti_24, respectively, the value of ν retrieved from the analysis of the two dimensional map discussed above would yield a negative Poisson's ratio. However, this is not compatible with titanium and titanium alloys samples, which are characterized by a Poisson's ratio ranging between 0.24-0.33 [48].

Comparison with α -Ti

The estimates of the elastic moduli C_{44} , ν , B , and E obtained in the previous sections have been compared with characteristic values associated with hcp- (α -) Ti. The results

are depicted in Figure 3.27. Values of C_{12} , ν , B , and E for hcp titanium are listed in Table 3.19.

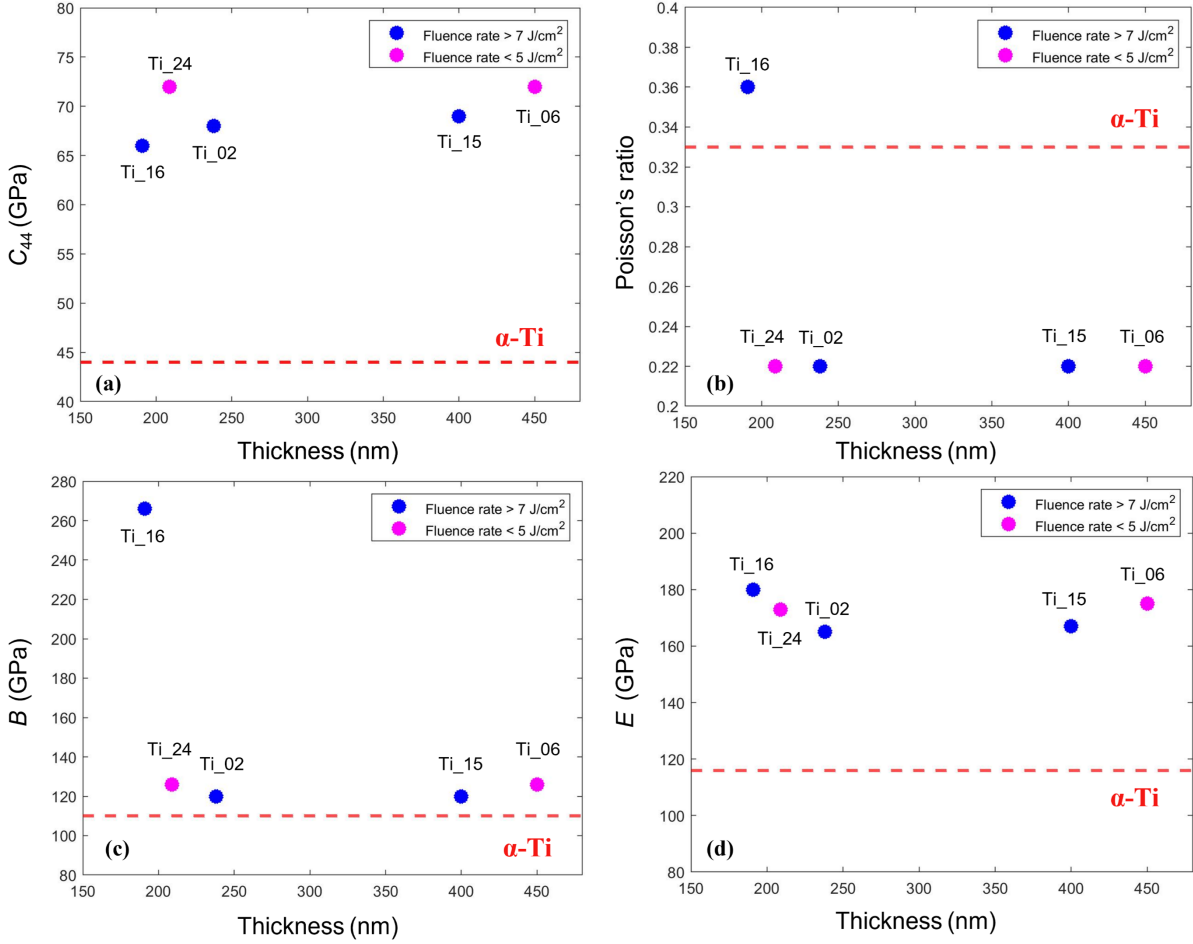


Figure 3.27: Comparison of elastic moduli C_{12} , ν , B , and E retrieved for the Ti_02, Ti_06, Ti_15, Ti_16, and Ti_24 samples and the characteristic values expected for α -Ti.

C_{44} (GPa)	ν	B (GPa)	E (GPa)
44	0.33	110	116

Table 3.19: Elastic moduli C_{44} , ν , B , and E associated with titanium in its α crystal phase [1, 47]

From Figure 3.27, it is possible to see that the elastic moduli assessed through the current Brillouin analysis differ from those expected in the case of an hcp crystal structure. In particular, it is important to highlight that the highest differences are registered for sample

Ti_16, which is the thinnest sample under analysis. Indeed, while the bulk modulus for the Ti_02, Ti_06, Ti_15, and Ti_24 samples increases of about 9%-15% with respect to the expected α -Ti value, the estimate of B for the Ti_16 sample is 142% higher than the expected one. The shear modulus C_{44} increases of around 50%-64% for the samples and reaches the minimum value for the Ti_16 one. The Young's modulus increases of 42%-51% for the Ti_02, Ti_06, Ti_15, and Ti_24 samples and is 55% higher than the expected one for the Ti_16 sample. Finally, while the Poisson's ratio decreases of 33% for the thickest samples, it increases of 9% for the thinnest one.

Upon comparing the elastic moduli estimates obtained through the current analysis with those expected for the α phase of titanium, one finds rather interesting results. Figure 3.27 suggests that the crystal structure of the analyzed samples may differ from that expected in nature. This hypothesis is also consistent with the values of the lattice parameters previously assessed for each sample (see Figure 3.2). One must keep in mind that the following analysis has been carried out upon imposing physical limits. The latter element might impact on the final values of the elastic moduli retrieved.

One could wonder how much the final results depend on the choice of the upper and lower bound. The analysis does not allow the assessment of the Poisson's ratio for most samples. Indeed, lower and upper boundaries have been taken into account for the Ti_02, Ti_06, Ti_15, and Ti_24 samples. The values of ν determined through the analysis of the extrema of the truncated contour lines are simply given by the average between the upper and lower bound chosen. Contour lines associated with the Ti_16 samples are closed across the analyzed region (see Figure 3.19), thus allowing a more precise estimate of ν .

With reference to the estimate of C_{44} , increasing the lower bound $\nu = 0.1$ would only slightly decrease the maximum value of the shear modulus. Upon increasing/decreasing the upper bound $\nu = 0.33$, one could slightly diminish/increase the lowest value of C_{44} .

An increase/decrease of the upper and lower bound of ν would result in an increase/decrease of the C_{11} minimum/maximum estimate. The variation of C_{11} can be observed easily than the one corresponding to C_{44} , as the range within which C_{11} changes is larger than that of C_{44} . The value of B would change accordingly to C_{11} .

Considering the value of E , one notes that increasing the lower bound of ν would increase the minimum estimate of E . An increase/decrease of the upper bound would result in an increase/decrease of the maximum value of E .

The aforementioned observations allow assessing that the C_{44} estimate is the most precise

one. Furthermore, the value of C_{44} is the least sensitive to the upper and lower bound of ν choice. Thus, C_{44} is the most robust results stemming from the whole procedure.

The exotic phase of titanium yields a C_{44} value that ranges in between 65-75 GPa, with respect to an expected value of 44 GPa for the α -Ti. Moreover, while the Young's modulus of the hcp titanium is around 120 GPa, it goes up to 160-180 GPa for the fcc crystal structure. An ongoing analysis is being carried out at the NanoLab on hcp titanium samples. This study yields a value of the shear modulus of 45 GPa, which is indeed close to the expected α -Ti estimate. Brillouin spectroscopy is thus able to correctly capture a sharp difference between the hcp and fcc titanium crystal structure. Uncertainties increase considering the volume stiffness (i.e., B and C_{11}).

Conclusions

Brillouin analysis is performed to assess the mechanical properties of titanium thin films produced at the Micro and Nano Structured Materials Laboratory (NanoLab) of the Energy Department of the Politecnico di Milano. The samples are first analyzed through EDXS and XRD. The EDXS analysis shows that all samples are characterized by an oxygen percentage of around 35-42%. The XRD analysis yields characteristic peaks which do not correspond to those found in the expected hcp-titanium structure. The 2θ positions assessed through XRD analysis suggest that the samples organized in a face-centered cubic crystal structure during deposition.

The key research hypothesis exploited to analyze such samples through Brillouin spectroscopy are the following:

- samples are found in a face-centered cubic crystal structure;
- samples are modeled as isotropic thin films perfectly adherent to a semi-infinite silicon substrate.

The aforementioned hypothesis allow to fully characterize the mechanical properties of samples through the elastic constants C_{11} and C_{44} .

Brillouin analysis suggests that the samples elastic moduli (i.e., C_{44} , ν , B , and E) differ from those expected in the case of an hcp crystal structure. Thickness seems to be the parameter which most influences the samples elastic moduli. Indeed, the thinnest sample is characterized by the highest detected bulk modulus and Poisson's ratio.

It is important to highlight that the proposed analysis allows to arbitrarily select the most reasonable physical limits to interpret data. Upper and lower bounds are selected in data analysis to best resemble titanium characteristics. Setting these limits somehow hampers our ability to identify the Poisson's ratio in most cases. Nevertheless, experimental data are well interpreted through the theoretical dispersion relations considered. Finally, results associated with sample Ti_24 are not considered reliable as the behavior of experimental data suggest that one of the aforementioned key hypothesis is violated.

Brillouin spectroscopy is an established optical non-destructive technique which allows

assessing the elastic properties of thin films. However, this is not the most common way to evaluate films elastic constants. Indeed, nanoindentation has become a widely exploited technique to assess mechanical properties from very small samples [49]. The latter technique yields sample elastic properties upon exploiting an external load. However, the main drawback of nanoindentation is that only a maximum depth of penetration of 10% of the film thickness can be analysed in a test, to avoid unintended probing of the properties of the substrate [50]. The samples analyzed in this thesis work are characterized by thicknesses ranging between circa 190 and 450 nm. In this framework, nanoindentation would not grasp too much information about the elastic properties of the samples. Indeed, the penetration depth exploited through nanoindentation would reach 19-45 nm, which is a rather small depth to be explored. Finally, the nanoindentation key output is the reduced modulus, which allows relating E to ν . The value of the Young's modulus is then assessed upon selecting a suitable Poisson's ratio. Thus, even exploiting nanoindentation, one would not be able to retrieve the exact value of ν .

The analysis proposed in this thesis yields interesting and fascinating results. The titanium thin films produced at the NanoLab are characterized by a lattice parameter which does not coincide with that expected for titanium α -phase. Values of the lattice parameters retrieved from the XRD analysis are compatible with previous findings showing that titanium can assemble in a face-centered cubic crystal structure. The peculiar behavior of the samples is assessed through their mechanical characterization. Upon assuming an fcc crystal structure, elastic constants C_{11} , C_{12} , and C_{44} are retrieved, together with the bulk modulus B , the Young's modulus E , and the Poisson's ratio ν . Key results are then compared with the characteristic α -Ti elastic moduli C_{44} , B , E , and ν . While C_{44} , B , and E are found to be higher than those associated with an hcp crystal structure, ν is found to be lower. These results suggest that the analyzed samples are harder than the commonly found α -Ti.

The key outputs of this thesis work are summarized in the following:

- samples lattice parameters are consistent with available literature observations and suggest that titanium organized in a fcc structure during deposition;
- elastic moduli C_{44} , B , E , and ν differ from those expected in a hcp titanium crystal structure and suggest that the analyzed samples are harder than the commonly found α -Ti;
- thickness seems to be the most impacting parameter on the sample elastic properties.

Further analysis of the samples is required to provide a more complete picture of their

mechanical behavior. For instance, analysis through transmission electron microscopy would provide additional insight on the actual structure of the samples. The latter technique would also yield enhance knowledge about the relevance of the oxygen presence in the formation of this new crystal form. Moreover, samples obtained at lower fluence rate could be investigated. Indeed, while samples Ti_06 and Ti_24 have been produced at lower fluence rates than the other samples, Brillouin analysis does not yield results of sufficient quality. This is mainly related to the availability of only a small data set for sample Ti_06. Indeed, only three peaks are identified (at incidence angles of 50°, 60°, and, 70°). Additionally, the analysis of sample Ti_24 shows contrasting behaviors. Indeed, while experimental data are consistent with a slow film on a fast substrate, their pattern is associated with a fast film on a slow substrate. Further analysis of the Ti_24 sample could be beneficial in order to assess whether problems have been encountered during its deposition. The analysis of sample Ti_24 may suggest that such a sample is not homogeneous, perfectly adherent to the substrate or correctly deposited.

While the fcc titanium crystal structure is present in the literature, to the best of our knowledge the elastic properties are found only as theoretical estimates. The latter suggest that such an exotic phase is characterized by higher elastic moduli, the fcc structure being stiffer but not necessarily harder than the hcp titanium. This thesis documents (to the best of our knowledge) the first measurement of the elastic moduli of this exotic titanium structure. The analysis carried out in this work yields values of elastic moduli higher than those expected for the α -Ti, thus being compatible with theoretical expectations.

Bibliography

- [1] C. Leyens and M. Peters, *Titanium and Titanium Alloys: Fundamentals and Applications*. Wiley, New York, 2003.
- [2] D. Dellasega *et al.*, “Role of energetic ions in the growth of fcc and ω crystalline phases in ti films deposited by hipims,” *Applied Surface Science*, 2021.
- [3] F.E. Wawner Jr. and K.R. Lawless, “Epitaxial growth of titanium thin films,” *J. Vac. Sci. Technol. A*, vol. 6, pp. 588–590, 1969.
- [4] A.A. Saleh *et al.*, “Observation of ultrathin metastable fcc ti films on al (110) surfaces,” *Phys. Rev. B*, vol. 49, p. 4908, 1994.
- [5] A.R. Jankowski *et al.*, “Synthesis and characterization of nanophase face-centered-cubic titanium,” *Nanostructured Mater.*, vol. 7, pp. 89–94, 1996.
- [6] S.K. Kim *et al.*, “Growth of face-centered-cubic titanium on aluminium,” *J. Phys. : Condens. Matter*, vol. 8, pp. 25–36, 1996.
- [7] Y. Sugawara *et al.*, “Interface structure of face-centered-cubic-Ti thin film grown on 6H-SiC substrate,” *J. Mater. Res.*, vol. 15, pp. 2121–2124, 2000.
- [8] D. Josell *et al.*, “Fcc titanium in Ti/Ni multilayers,” *Mat. Lett.*, vol. 22, pp. 275–279, 1995.
- [9] D. Van Heerden *et al.*, “The formation of FCC titanium in titanium-aluminium multilayers,” *Acta Mater.*, vol. 44 (1), pp. 297–306, 1996.
- [10] I. Manna *et al.*, “Formation of face-centered-cubic titanium by mechanical attrition,” *J. Appl. Phys.*, vol. 93, pp. 1520–1524, 2003.
- [11] H.C. Wu *et al.*, “Rolling-induced face centered cubic titanium in hexagonal close packed titanium at room temperature,” *Sci. Rep.*, vol. 6, p. 24370, 2016.
- [12] A. Aguayo *et al.*, “Elastic stability and electronic structure of fcc Ti, Zr, and Hf: A first-principles study,” *Phys. Rev. B*, vol. 65, 2002.

- [13] D. M. Tshwane *et al.*, “Surface analysis of the stress-induced, impurity driven face centered cubic titanium phase and the ranging lattice parameter sizes,” *Materials Today Communications*, vol. 24, p. 101168, 2020.
- [14] A.S. Bolokang *et al.*, “Microstructure and phase transformation on milled and unmilled ti induced by water quenching,” *Materials Letters*, vol. 132, pp. 157–161, 2014.
- [15] D.H. Hong *et al.*, “Stress-induced hexagonal close-packed to face-centered cubic phase transformation in commercial-purity titanium under cryogenic phase-strain compression,” *Scripta Mater.*, vol. 69, pp. 405–408, 2013.
- [16] C. Chen *et al.*, “The microstructure and formation mechanism of face-centered cubic ti in commercial pure ti foils during tensile deformation at room temperature,” *Mater. Charact.*, vol. 136, pp. 257–263, 2018.
- [17] Y. Chang *et al.*, “Could face-centered cubic titanium in cold-rolled commercially-pure titanium only be a ti-hydride?,” *Scripta Mater.*, vol. 178, pp. 39–43, 2020.
- [18] A.S. Bolokang *et al.*, “Formation of the metastable FCC phase by ball milling and annealing of titanium-stearic acid powder,” *Adv. Powder Technol.*, vol. 26, pp. 632–639, 2015.
- [19] P. E. Vullum *et al.*, “Observations of nanoscopic, face centered cubic Ti and TiH_x,” *Appl. Phys. A*, vol. 94, pp. 787–793, 2009.
- [20] M. J. Phasha *et al.*, “Solid-state transformation in nanocrystalline Ti induced by ball milling,” *Mater. Lett.*, vol. 64, pp. 1215–1218, 2010.
- [21] A.S. Bolokang *et al.*, “Formation of titanium nitride produced from nano-crystalline titanium powder under nitrogen atmosphere,” *Int. J. Refract. Met. Hard Mater.*, vol. 28, pp. 610–615, 2010.
- [22] P. Chatterjee *et al.*, “An X-ray diffraction of nanocrystalline titanium prepared by high-energy vibrational ball milling,” *Appl. Surf. Sci.*, vol. 182, pp. 372–376, 2001.
- [23] I. Manna *et al.*, “Positron lifetime studies of the hcp to fcc transformation induced by mechanical attrition of elemental titanium,” *Phys. Lett. A*, vol. 328, pp. 246–254, 2004.
- [24] L. Niu *et al.*, “Mechanical behavior and deformation mechanism of commercial pure titanium foils,” *Mater. Sci. Eng. A*, vol. 707, pp. 435–442, 2017.
- [25] X. Zheng *et al.*, “Deformation induced FCC lamellae and their interaction in commercial pure Ti,” *Scripta Mater.*, vol. 162, pp. 326–330, 2019.

- [26] V. L. Sliwko *et al.*, “The fcc-bcc structural transition: I. A band theoretical study for Li, K, Rb, Ca, Sr, and the transition metals Ti and V,” *J. Phys. Condens. Matter*, vol. 8, p. 799, 1996.
- [27] H. Zhang *et al.*, “Strain direction dependency of deformation mechanisms in an HCP-Ti crystalline by molecular dynamics simulations,” *Comp. Mater. Sci.*, vol. 172, p. 109328, 2020.
- [28] J. Chakraborty *et al.*, “Thickness-dependent fcc-hcp phase transformation in polycrystalline titanium thin films,” *Acta Mater.*, vol. 59, pp. 2615–2623, 2011.
- [29] M. Fazio *et al.*, “Study of the structure of titanium thin films deposited with a vacuum arc as a function of the thickness,” *Thin Solid Films*, vol. 593, pp. 110–115, 2015.
- [30] Z. Zhao *et al.*, “The observation of the orthorombic α'' and fcc titanium in deformed commercially pure titanium compressed at elevated temperature,” *J. Alloys. Compd.*, vol. 815, pp. 1522981–10, 2020.
- [31] Q. Yu *et al.*, “In situ TEM observation of FCC Ti formation at elevated temperatures,” *Scripta Mater.*, vol. 140, pp. 9–12, 2017.
- [32] H. Shahmir *et al.*, “An evaluation of the hexagonal close-packed to face-centered cubic phase transformation in a Ti-6Al-4V alloy during high-pressure torsion,” *Mater. Sci. Eng. A*, vol. 704, pp. 212–217, 2017.
- [33] M. G. Beghi, *Ultrasonic and Spectroscopic Techniques for the Measurement of the Elastic Properties of Nanoscale Materials*. IntechOpen.
- [34] T. Kundu, *Mechanics of Elastic Waves and Ultrasonic Nondestructive Evaluation, in Ultrasonic and Electromagnetic NDE for Structure and Material Characterization - Engineering and Biomedical Applications*. CRC Press, Taylor Francis group, Boca Raton, London, New York, 2004.
- [35] E. Besozzi, “Caratterizzazione di film di tungsteno mediante spettroscopia brillouin,” *Tesi di Laurea*, A.A. 2011-2012.
- [36] T. Lay and T. C. Wallace, *Modern Global Seismology*. 1995.
- [37] M. G. Beghi, *Measurement of the Elastic Properties of Solids by Brillouin Spectroscopy, in Ultrasonic and Electromagnetic NDE for Structure and Material Characterization - Engineering and Biomedical Applications*. CRC Press, Taylor Francis group, Boca Raton, London, New York, 2004.
- [38] Operator’s manual., *The coherent INNOVA 300 series ion laser*.

- [39] J. R. Sandercock, *TFP-1 Interferometer Operator Manual*. JRS Scientific Instruments, Zwillikon, CH, 2001.
- [40] Z. Liu, *Management and Control of Corrosion*, in *Shreir's Corrosion*. Elsevier Science, 2010.
- [41] C. O. Colpan *et al.*, *Energy Conversion*, in *Comprehensive Energy Systems*. Elsevier Science, 2018.
- [42] https://en.wikipedia.org/wiki/Bragg%27s_law,
- [43] J. Carrera *et al.*, "Estimation of aquifer parameters under transient and steady state conditions: 1. maximum likelihood method incorporating prior information," *Water Resources Research*, vol. 22, pp. 199–210, 1986.
- [44] M. Beghi *et al.*, "Precision and accuracy in film stiffness measurement by brillouin spectroscopy," *Rev. Sci. Instrum.*, vol. 82, 2011.
- [45] G.A.F. Seber *et al.*, *Nonlinear regression*. Wiley Interscience, 2003.
- [46] M. Mohr *et al.*, "Young's modulus, fracture strength, and poisson's ratio of nanocrystalline diamond films," *Journal of Applied Physics*, vol. 116, 2014.
- [47] <https://en.wikipedia.org/wiki/Titanium>,
- [48] https://en.wikipedia.org/wiki/Poisson%27s_ratio,
- [49] A. B. Mann, *Surfaces and Interfaces for Biomaterials*, vol. 225-247. Woodhead Publishing Series in Biomaterials, 2005.
- [50] A. C. Fischer-Cripps, *Nanoindentation of Thin Films*, vol. 132–143. Springer New York, NY, 2004.

List of Figures

1	Titanium's (a) hcp α phase and (b) bcc β phase. Their most densely packed planes and directions are highlighted ([1]).	1
1.1	Transformation of a reference body (R) into its deformed state (D) in a (x_1, x_2, x_3) Cartesian coordinate system. Figure adapted from [35].	8
1.2	External forces F_i ($i = 1, 2, 3, 4$) applied to a body in equilibrium. Two exemplary planes passing through the point P and cutting the body into two halves are highlighted (from [34]).	9
1.3	Stress components $\sigma_{i,j}$ ($i, j = 1, 2, 3$) in a (x_1, x_2, x_3) coordinate system (from [34]).	10
1.4	Stress-strain relations for elastic and inelastic materials (from [34]).	10
1.5	Sketch of the geometry of a film of thickness h supported by a semi-infinite substrate.	18
1.6	Backscattering by a SAW of wavevector $\mathbf{k}_{//}$, direct backscattering by a bulk acoustic wave (i.e., acoustic waves occurring in the bulk of material) of wavevector $\mathbf{k}_b^{(d)}$, and indirect backscattering by a bulk wave of wavevector $\mathbf{k}_b^{(i)}$. \mathbf{q}_i , and \mathbf{q}_s are the incident and scattered wavevectors; $\mathbf{q}_{i,s}$, $\mathbf{q}'_{i,s}$ are the optical wavevectors in the external medium (vacuum) and in layer 1. Image adapted from [34].	21
1.7	Example of Brillouin spectrum. The elastic peak and the Stokes/anti-Stokes events can be seen.	22
1.8	Brillouin backscattering geometry to study opaque films. Here, \mathbf{q}_i and θ are the incident wavevector and angle. \mathbf{q}_s , and $\mathbf{k}_{//}$ are the scattered and SAW's wavevector, respectively. Image adapted from [37]	23

2.1	Typical experimental set-up for Brillouin spectroscopy in backscattering geometry. M1-M2 and L1-L4 are mirrors and lenses, respectively. Sp is the specimen. L2, P and L3 allow spatial filtering by the two lenses and a pinhole P. FP is the Fabry-Perot interferometer (for simplicity, a single interferometer is depicted, instead of the tandem multipass one). D is the light detector (typically a phototube). Light is focused and collected, in backscattering geometry, by lens L1. Image adapted from [37].	26
2.2	Optical path followed by the laser radiation. Attenuators are used to modify the intensity of light. The dashed and continuous lines represent the secondary and primary radiation beams, respectively.	27
2.3	Fabry-Perot interferometer transmittance with respect to a given D mirror distance. Image adapted from [39].	29
2.4	(a)-(b) Transmission in two Fabry-Perot interferometers FP1 and FP2 with different FSRs. (c) Transmission in tandem configuration (adapted from [39]).	33
2.5	Exemplary ghosts due to instrumentation which can be seen in a typical Brillouin spectrum.	34
2.6	Exemplary scanning tandem configuration with two Fabry-Perot interferometers, FP1 and FP2, characterized by mirror distance $L1$ and $L2$, respectively. Image adapted from [39].	35
2.7	(a) Picture and (b) sketch of Fabry-Perot interferometers FP1 and FP2 supported by active isolation system MOD-2, characterized by two dynamical isolation mounts (MOD-2 elements). Image (b) adapted from [39]. . .	36
2.8	(a) Optical components for multipassing and (b) Fabry-Perot interferometers used in the laboratory experiments in the current thesis.	37
2.9	(a) Beam-splitters and Fabry-Perot FP1 and FP2 used in the laboratory experiments. (b) Scheme of alignment strategy. (c)-(d) Measured reflected intensity for two imperfectly and perfectly aligned interferometers, respectively. Images (b)-(c)-(d) are adapted from [39].	37
2.10	Interface of the interferometer control equipment. The 5 degrees of freedom X1, Y1, X2, Y2 and ΔZ are highlighted in red and used to maximize transmission of the interferometers.	38
2.11	Scheme of the optics used in tandem multipass 3+3 configuration (image adapted from [39]). M1-M6 and L1-L2 are mirrors and lenses, respectively. A1-A3 are apertures. P1-P2 are pinholes, whereas PR1-PR2 are prisms. G1-G2 and BS1-BS2 are glassblock and beam-splitters, respectively, used in the alignment configuration (see below).	39

List of Figures	91
2.12 Scheme of the optical components used for alignment (image from [39]).	40
2.13 Sketch of pulsed laser deposition (image taken from [40]).	41
2.14 Schematic representation of X-ray Diffraction in $\theta/2\theta$ configuration.	42
3.1 Example of XRD spectra obtained for Ti_15 and Ti_16 samples. Two peaks at circa 36° and 76° (characteristics of the fcc structure) can be seen. The sharp peak at 33° is associated with the Si substrate.	45
3.2 Comparison between literature values of lattice parameters (see Table 3.4) and those obtained through PLD produced samples. The techniques listed in Table 3.4 are here grouped for ease of interpretation. References listed in Table 3.4 are here used to label the lattice parameters values.	47
3.3 (a) Brillouin spectra experimentally retrieved from the analysis of the Ti_02 sample (incidence angles are written in the same color as the corresponding data set). Colored and black lines represent the raw (i.e., data as collected experimentally) and filtered data, respectively. Spectra obtained for different incidence angles are shifted to enhance readability. (b) Experimental velocities evaluated upon fitting data in (a) for each incidence angle. The acoustic velocity associated with the silicon substrate corresponds to the red dashed line in (b).	55
3.4 Contour lines corresponding to Equation 3.10 evaluated for sample Ti_02. The 68% confidence level considered is highlighted in black; 90%, 95%, and 99% confidence levels are also depicted in black for completeness; $\nu = 0.1$ and $\nu = 0.33$ bounds are highlighted in red. Red symbols represent the extrema of the truncated contour lines at the 68% confidence level considered for the analysis.	56
3.5 Contour lines evaluated for sample Ti_02; $\nu = 0.1$ and $\nu = 0.33$ bounds are highlighted in dashed red lines. Red dots represent the extrema of the truncated contour lines at the 68% confidence level considered for the analysis. Constant (a) C_{12} , (b) B , and (c) E curves passing through the outer extrema of the truncated contour lines are highlighted in green, blue, and magenta, respectively.	58
3.6 Experimental data in Figure 3.3 (b) superimposed to (a) theoretical dispersion relation obtained with the estimates of C_{11} , C_{44} and C_{12} in Table 3.5 and (b) the characteristic parameters (i.e., C_{11} , C_{44} , C_{12} , and mass density) of hcp titanium.	59

- 3.7 (a) Brillouin spectra experimentally retrieved from the analysis of the Ti_06 sample (incidence angles are written in the same color as the corresponding data set). Colored and black lines represent the raw (i.e., data as collected experimentally) and filtered data, respectively. Spectra obtained for different incidence angles are shifted to enhance readability. (b) Experimental velocities evaluated upon fitting data in (a) for each incidence angle. 60
- 3.8 Contour lines evaluated for sample Ti_06. The 68% confidence level considered is highlighted in black. The 90% confidence level is also depicted in black for completeness. $\nu = 0.1$ and $\nu = 0.33$ bounds are highlighted in red. Red dots represent the extrema of the truncated contour lines at the 68% confidence level considered for the analysis. 61
- 3.9 Contour lines evaluated for sample Ti_06; $\nu = 0.1$ and $\nu = 0.33$ bounds are highlighted in dashed red lines. Red dots represent the extrema of the truncated contour lines at the 68% confidence level considered for the analysis. Constant (a) C_{12} , (b) B , and (c) E curves through the outer extrema of the truncated contour lines are highlighted in green, blue, and, magenta, respectively. 63
- 3.10 Experimental data in Figure 3.7 (b) superimposed to (a) theoretical dispersion relations obtained with the estimates of C_{11} , C_{44} , and C_{12}^{map} in Table 3.9-3.10 and (b) the characteristic parameters (i.e., C_{11} , C_{44} , C_{12} , and mass density) of hcp titanium. 63
- 3.11 (a) Brillouin spectra experimentally retrieved from the analysis of the Ti_15 sample (incidence angles are written in the same color as the corresponding data set). Colored and black lines represent the raw (i.e., data as collected experimentally) and filtered data, respectively. Spectra obtained for different incidence angles are shifted to enhance readability. (b) Experimental velocities evaluated upon fitting data in (a) for each incidence angle. 64
- 3.12 Contour lines evaluated for sample Ti_15. The 68% confidence level considered is highlighted in black. The 90%, 95%, and 99% confidence levels are also depicted in black for completeness; $\nu = 0.1$ and $\nu = 0.33$ bounds are highlighted in red. Red dots represent the extrema of the truncated contour lines at the 68% confidence level considered for the analysis. 65

3.13 Contour lines evaluated for sample Ti_15. $\nu = 0.1$ and $\nu = 0.33$ bounds are highlighted in dashed red lines. Red dots represent the extrema of the truncated contour lines at the 68% confidence level considered for the analysis. Constant (a) C_{12} , (b) B , and (c) E curves passing through the outer extrema of the truncated contour lines are highlighted in green, blue, and, magenta, respectively. 66

3.14 Experimental data in Figure 3.11 (b) superimposed to (a) theoretical dispersion relations obtained with the estimates of C_{11} , C_{44} , and C_{12}^{map} in Table 3.11 and 3.12 and (b) the characteristic parameters (i.e., C_{11} , C_{44} , C_{12} , and mass density) of hcp titanium. 67

3.15 Contour lines evaluated for sample Ti_15 obtained upon enlarging the field of view of Figure 3.12. The 68% confidence level considered is highlighted in black; $\nu = 0.1$ and $\nu = 0.42$ bounds are highlighted in red. Red dots represent the extrema of the truncated contour lines at the 68% confidence level considered for the analysis. 67

3.16 Contour lines evaluated for sample Ti_15; $\nu = 0.1$ and $\nu = 0.42$ bounds are highlighted in dashed red lines. Red dots represent the extrema of the truncated contour lines at 68% confidence level considered for the analysis. Constant (a) C_{12} , (b) B , and (c) E curves passing through the outer extrema of the truncated contour lines are highlighted in green, blue, and magenta, respectively. 68

3.17 Experimental data in Figure 3.11 (b) superimposed to (a) theoretical dispersion relation obtained with the estimates of C_{11} , C_{44} , and C_{12}^{map} in Table 3.13 and 3.14 and (b) theoretical dispersion relation obtained with the estimates of C_{11} , C_{44} , and C_{12}^{map} in Table 3.11 and 3.12. 69

3.18 (a) Brillouin spectra experimentally retrieved from the analysis of the Ti_16 sample (incidence angles are written in the same color as the corresponding data set). Colored and black lines represent the raw (i.e., data as collected experimentally) and filtered data, respectively. Spectra obtained for different incidence angles are shifted to enhance readability. (b) Experimental velocities evaluated upon fitting data in (a) for each incidence angle. 70

- 3.19 Contour lines evaluated for sample Ti_16. The 68% confidence level considered is highlighted in black. The 90%, 95%, and 99% confidence levels are also depicted in black for completeness; $\nu = 0.1$ and $\nu = 0.33$ bounds are highlighted in red in (a); the $\nu = 0.42$ bound is highlighted in red in (b). Red dots represent the extrema of the truncated contour lines at the 68% confidence level considered for the analysis. 71
- 3.20 Contour lines evaluated for sample Ti_16; the $\nu = 0.42$ bound is highlighted in dashed red lines. Red dots represent the extrema of the truncated contour lines at the 68% confidence level considered for the analysis. Constant (a) C_{12} , (b) ν , (b) B , and (d) E curves passing through the outer extrema of the truncated contour lines are highlighted in green, red, blue, and magenta, respectively. 72
- 3.21 Experimental data in Figure 3.18 (b) superimposed to (a) theoretical dispersion relation obtained with the estimates of C_{11} , C_{44} , and C_{12}^{map} in Table 3.15 and 3.16 and (b) the characteristic parameters (i.e., C_{11} , C_{44} , C_{12} , and mass density) of hcp titanium. 73
- 3.22 (a) Brillouin spectra experimentally retrieved from the analysis of the Ti_24 sample (incidence angles are written in the same color as the corresponding data set). Colored and black lines represent the raw (i.e., data as collected experimentally) and filtered data. Spectra obtained for different incidence angles are shifted to enhance readability. (b) Experimental velocities evaluated upon fitting data in (a) for each incidence angle. 74
- 3.23 Contour lines evaluated for sample Ti_24. The 68% confidence level considered is highlighted in black. The 90% and 95% confidence levels are also depicted in black for completeness; the $\nu = 0.1$ and $\nu = 0.33$ bounds are highlighted in red. Red dots represent the extrema of the truncated contour lines at the 68% confidence level considered for the analysis. 75
- 3.24 Contour lines evaluated for sample Ti_24; the $\nu = 0.1$ and $\nu = 0.33$ bounds are highlighted in dashed red lines. Red dots represent the extrema of the truncated contour lines at the 68% confidence level considered for the analysis. Constant (a) C_{12} , (b) B , and (c) E curves passing through the outer extrema of the truncated contour lines are highlighted in green, blue, and magenta, respectively. 76
- 3.25 Experimental data in Figure 3.22 (b) superimposed to (a) theoretical dispersion relation obtained with the estimates of C_{11} , C_{44} , and C_{12}^{map} in Table 3.17 and 3.18 and (b) the characteristic parameters (i.e., C_{11} , C_{44} , C_{12} , and mass density) of hcp titanium. 76

3.26 Contour lines for sample Ti_24 associated with an enlarged range of C_{44} values. The 68%, 90%, 95%, and 99% confidence levels are shown as well as the red dots showing the truncated contour lines at the 68% confidence level. The $\nu = -1$ constant line is highlighted in red. 77

3.27 Comparison of elastic moduli C_{12} , ν , B , and E retrieved for the Ti_02, Ti_06, Ti_15, Ti_16, and Ti_24 samples and the characteristic values expected for α -Ti. 78

List of Tables

1	Values of the lattice parameter of fcc titanium (adapted from [13]). The values depend on both the process of formation of titanium and the material exploited.	4
3.1	Thickness, fluence rate, deposition time and background pressure for samples produced via PLD. The denomination of titanium (Ti) samples is also reported. All samples are grown on a silicon substrate with thickness of the order of hundreds of microns.	43
3.2	Oxygen percentage found in samples through EDXS analysis. The denomination of titanium (Ti) samples is also reported.	44
3.3	2θ positions obtained upon fitting XRD data with a Lorentzian function. The Miller indexes defining the crystallographic directions considered are highlighted. Since the XRD spectra of sample Ti_24 has not been measured, values of a sample of the very same thickness (Ti_02) are considered in this case.	46
3.4	Lattice parameter and mass density of each sample obtained via XRD. . .	47
3.5	Elastic constants C_{11} and C_{44} obtained from the analysis of the contour lines of sample Ti_02.	57
3.6	Elastic constant C_{12} , Poisson's ratio ν , bulk modulus B , and Young's modulus E theoretically evaluated with Equations 1.121-1.15-1.17-1.13 for sample Ti_02. Errors are evaluated through the usual propagation error formula (Equation 3.2).	57
3.7	Elastic constant C_{12} , Poisson's ratio ν , bulk modulus B , and Young's modulus E evaluated considering the truncated contour lines alongside their error bars for sample Ti_02.	58
3.8	Literature values for elastic constant C_{44} and mass density of hcp titanium [1, 47]. C_{11} and C_{12} are calculated from values of B and C_{44} available in the literature upon imposing the isotropy condition in Equation 1.12. . . .	59
3.9	Values of elastic constants C_{11} and C_{44} obtained from the analysis of the contour lines of sample Ti_06.	62

3.10	Elastic constant C_{12} , Poisson's ratio ν , bulk modulus B , and Young's modulus E theoretically evaluated with Equations 1.121.15-1.17-1.13 (labeled with the superscript " <i>calc</i> ") and evaluated considering the truncated contour lines alongside their error bars (labeled with the superscript " <i>map</i> ") for sample Ti_06.	62
3.11	Elastic constants C_{11} and C_{44} obtained from the analysis of the contour lines of sample Ti_15.	66
3.12	Elastic constant C_{12} , Poisson's ratio ν , bulk modulus B , and Young's modulus E theoretically evaluated with Equations 1.121.15-1.17-1.13 (labeled with the superscript " <i>calc</i> ") and evaluated considering the truncated contour lines alongside their error bars (labeled with the superscript " <i>map</i> ") for sample Ti_15.	66
3.13	Elastic constants C_{11} and C_{44} obtained from the analysis of the contour lines of sample Ti_15 in Figure 3.15.	68
3.14	Elastic constant C_{12} , Poisson's ratio ν , bulk modulus B , and Young's modulus E theoretically evaluated with Equations 1.121.15-1.17-1.13 (labeled with the superscript " <i>calc</i> ") and evaluated considering the truncated contour lines alongside their error bars (labeled with the superscript " <i>map</i> ") in Figure 3.15.	68
3.15	Elastic constants C_{11} and C_{44} obtained from the analysis of the contour lines of sample Ti_16.	71
3.16	Elastic constant C_{12} , Poisson's ratio ν , bulk modulus B , and Young's modulus E theoretically evaluated with Equations 1.121.15-1.17-1.13 (labeled with the superscript " <i>calc</i> ") and evaluated considering the truncated contour lines alongside their error bars (labeled with the superscript " <i>map</i> ") for sample Ti_16.	72
3.17	Elastic constants C_{11} and C_{44} obtained from the analysis of the contour lines of sample Ti_24.	75
3.18	Elastic constant C_{12} , Poisson's ratio ν , bulk modulus B , and Young's modulus E theoretically evaluated with Equations 1.121.15-1.17-1.13 (labeled with the superscript " <i>calc</i> ") and evaluated considering the truncated contour lines alongside their error bars (labeled with the superscript " <i>map</i> ") for sample Ti_24.	75
3.19	Elastic moduli C_{44} , ν , B , and E associated with titanium in its α crystal phase [1, 47]	78

List of Main Symbols

Variable	Description	SI unit
\mathbf{X}, \mathbf{x}	position vector	m
\mathbf{u}	displacement	m
ε_{ij}	strain tensor	
ω_{ij}	rotation tensor	
$\mathbf{T}^{(n)}$	traction	
σ_{ij}	stress components	Pa
$C_{i,j,k,l}$	elastic constants	Pa
E	Young's modulus	Pa
G, C_{44}	shear modulus	Pa
ν	Poisson's ratio	Pa
B	bulk modulus	Pa
ρ	mass density	kg/m ³
\mathbf{k}, \mathbf{q}	wavevector	m ⁻¹
Ω, ω	angular frequency	Hz
c	velocity	m/s
l_i	direction cosine	
δ_{ij}	Kronecher delta	
$\Gamma_{j,k}$	Christoffel tensor	Pa
λ	wavelength	m
$\lambda_{//}$	wavelength parallel to the surface	m
$k_{//}$	wavevector parallel to the surface	m ⁻¹
h	film thickness	m
k_B	Boltzmann's constant	J/K
T	thermodynamic temperature	K
a	atomic distance	Å
f	frequency	Hz
θ	angle	°
T	transmittance	
$D, L1, L2$	mirror distance	m

F	finesse	
R	mirror reflectivity	
C	contrast	
FSR	free spectral range	Hz
h, k, l	Miller indexes	
m_{Ti}, m_O	Titanium and Oxygen mass	kg
LS	least square estimator	
σ	standard deviation	

